Heat Engineering

Journal of Research

of the

National Bureau of Standards

JULY 1933

VOLUME 11 NUMBER 1

U. S. DEPARTMENT OF COMMERCE
Sinclair Weeks, Secretary
NATIONAL BUREAU OF STANDARDS
A. V. Astin, Director

JULY • 1958
VOLUME • 61
NUMBER • 1

JOURNAL OF RESEARCH

of the

NATIONAL BUREAU OF STANDARDS

PERIODICALS OF THE NATIONAL BUREAU OF STANDARDS

The National Bureau of Standards is engaged in fundamental and applied research in physics, chemistry, mathematics, and engineering. Projects are conducted in fifteen fields: electricity, optics and metrology, heat and power, atomic and radiation physics, chemistry, mechanics, organic and fibrous materials, metallurgy, mineral products, building technology, applied mathematics, electronics, ordnance development, radio propagation, and missile development. The Bureau has custody of the national standards of measurement and conducts research leading to the improvement of scientific and engineering standards and of techniques and methods of measurement. Testing methods and instruments are developed; physical constants and properties of materials are determined; and technical processes are investigated.

JOURNAL OF RESEARCH

Internationally known as a leading scientific periodical, the Journal presents research papers by authorities in the specialized fields of physics, mathematics, chemistry, and engineering. Complete details of the work are presented, including laboratory data, experimental procedures, and theoretical and mathematical analyses. Annual subscription: domestic, $5.50; foreign, $6.75.

TECHNICAL NEWS BULLETIN

Summaries of current research at the National Bureau of Standards are published each month in the Technical News Bulletin. The articles are brief, with emphasis on the results of research, chosen on the basis of their scientific or technologic importance. Lists of all Bureau publications during the preceding month are given, including Research Papers, Handbooks, Applied Mathematics Series, Building Materials and Structures Reports, and Circulars. Each issue contains 12 or more two-column pages; illustrated. Annual subscription: domestic, $1.00; foreign, $1.25.

BASIC RADIO PROPAGATION PREDICTIONS

The Predictions provide the information necessary for calculating the best frequencies for communication between any two points in the world at any time during the given month. The data are important to all users of long-range radio communications and navigation, including broadcasting, airline, steamship, and wireless services, as well as to investigators of radio propagation and ionosphere. Each issue, covering a period of one month, is released three months in advance and contains 16 large pages, including pertinent charts, drawings, and tables. Annual subscription: domestic, $1.00; foreign, $1.25.

Order all publications from the Superintendent of Documents
U. S. Government Printing Office, Washington 25, D. C.

The printing of this publication has been approved by the Director of the Bureau of the Budget, May 12, 1953.

Journal of Research of the National Bureau of Standards Vol. 51, No. 1, July 1953 Research Paper 2426

Fabrication of Radio-Frequency Micropotentiometer Resistance Elements

Lewis F. Behrent

Disk resistors between 1 and 10^3 milliohms needed for the radio-frequency micropotentiometer were not available. Therefore, considerable research was necessary on a wide variety of processes for forming thin-film elements. Those methods whereby resistors stable to within plus or minus 1 percent were consistently produced are described in detail, and the various limitations, fabrication problems, and solutions to these problems are discussed.

1. Introduction

With the rapid growth of the electronics field, particularly in the past decade, there has been an increasing need for accurate voltage standards in the microvolt range for radio-receiver sensitivity measurements, field-intensity determinations, the calibration of r-f signal generators, and other applications. At the present time an accuracy of ± 1 percent has become highly desirable. A device developed to meet this need, called the r-f micropotentiometer,[1,2] provides an accurate, portable, and rugged low-impedance source of r-f voltages from 1 to 10^5 μv for use both in the laboratory and in the field. To achieve a low-output impedance of 1 to 10^3 milliohms, it was necessary to develop low-resistance disk elements. Research was conducted on a great many different processes for making thin-film resistive elements, to determine which consistently produced elements having the requisite stability of ± 1 percent over long periods of time and a satisfactorily flat frequency characteristic to at least 300 Mc.

The following processes were tried: (a) clamping of resistive disks, (b) low-temperature painting and baking, (c) high-temperature firing, (d) evaporation and plating, and (e) chemical reduction. Only three processes will be described here, that is, high-temperature firing, evaporation and plating, and clamping. Low-temperature paints proved unsatisfactory, whereas the value of the chemical-reduction process has not been fully determined.

2. General Description

Basically, a micropotentiometer consists of a disk resistor element whose r-f impedance is resistive, the same as for direct current, and some means to indicate the potential across that element. For example, figure 1, a, shows such a resistor terminating an essentially lossless coaxial line. The input voltage to the line, (1 to 10 v), may be measured accurately by means of a calibrated r-f voltmeter. The current at the resistive element is

$$I_R = \frac{E_S}{Z_L \cos \beta l + jZ_0 \sin \beta l}, \quad (1)$$

where at a given frequency

I_R = current at the resistive element, amperes
E_S = r-f voltage input to the line, volts
Z_L = impedance of the resistive element, ohms
Z_0 = characteristic impedance of the line, ohms
$\beta = 2\pi/\lambda$
l = electrical length of the line, centimeters
λ = wavelength of the r-f signal in the line, centimeters.

Therefore,

$$E_R = I_R Z_L = \frac{E_S Z_L}{Z_L \cos \beta l + jZ_0 \sin \beta l}, \quad (2)$$

where E_R is volts at the resistive element. At those frequencies where l is an odd multiple of $\lambda/4$, eq (2) reduces simply to

$$E_R = \frac{E_S Z_L}{Z_0}. \quad (3)$$

Figures 1, b, and 1, c, illustrate a thermoelement and a bolometer, respectively, used to measure the current flowing in the resistor, R. For these latter applications the current monitor is considered as having no frequency error even at the highest radio frequency used.

By using resistances of from 1 milliohm to 1 ohm in combination with current levels between 1 and 100 ma, levels from 1 to 10^5 μv can be made available. The voltage range may be extended to lower or higher values. However, the use of higher resistances may make it necessary to correct for the impedance of some external circuits connected across the resistance element.

The resistance of an annular ring is principally a function of its physical dimensions and the electrical conductivity of the resistive material used.[3] Expressed mathematically,

$$R = \frac{1}{2\pi\sigma d} \ln \gamma, \quad (4)$$

[1] Radio-frequency micropotentiometers, NBS Tech. News Bul. *35*, 33-34 (March 1951).
[2] M. C. Selby, Accurate r-f microvoltages, Communications and Electronics, AIEE, No. 6, 158-164 (May 1953).
[3] W. Jackson and L. G. H. Huxley, The solution of transmission-line problems by use of the circle diagram of impedance, Trans. IEE **91**, No. III (London, 1944).

259947—53——1

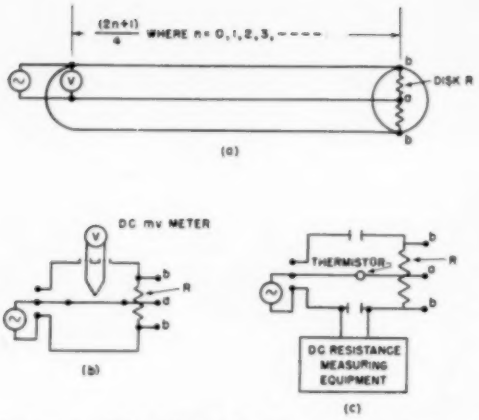

FIGURE 1. *Schematics of three types of radio-frequency micropotentiometers.*

R, disk resistive element; RF output is obtained across the coaxial connector ab. a, coaxial line; b, thermoelement; and c, thermistor.

where

R = resistance of the annular ring, ohms
$\sigma = 1/\rho$ = mho/cm
$\gamma = r_2/r_1$
d = thickness of the resistive film, centimeters
r_1 = inner radius of the annular ring, centimeters, or inches
r_2 = outer radius of the annular ring, centimeters, or inches
ρ = resistivity of the metal, ohms/cm

A basic sectional line drawing of a typical resistive element and the coaxial electrodes with which it is in contact, figure 2, identifies the dimensions r_2, r_1, and d in eq (4). When the resistive film was formed by firing conductive paints containing the noble metals, the resistance values obtained were somewhat greater than calculations would indicate because of the physical properties of the film so formed.

At zero frequency the current flowing in a conductor is uniformly distributed over its entire cross section. However, as the frequency is increased, there is a greater concentration of the current close to the surface, thereby increasing the resistance above its d-c value. This phenomenon[4], known as "skin effect", must be largely eliminated in the resistive element of the micropotentiometer, where the convenience of operating with d-c calibration values is desirable.

The depth of r-f current penetration, δ, in a thick, solid metal is given by

$$\delta = \left(\frac{1}{\sigma_m \pi f \mu_m}\right)^{\frac{1}{2}}, \qquad (5)$$

where

δ = depth of penetration in meters
σ_m = conductivity of the metal
f = frequency of the applied current in c/s
$\mu_m = 4\pi \times 10^{-7}$ h/m for nonferrous metals.

[4] F. E. Terman, Radio engineering handbook, p. 34. (McGraw-Hill Book Co., Inc., New York, N. Y., 1943).

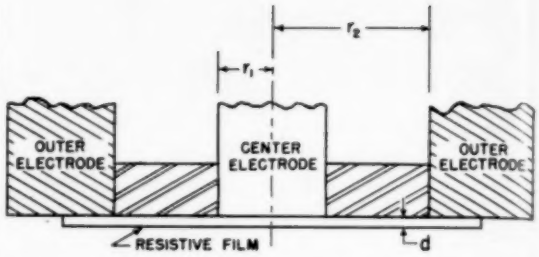

FIGURE 2. *Cross-sectional line drawing of resistive element, showing the electrodes and the resistive film.*

Considering the thin-film annulus as a section of coaxial line with a solid conductor as the propagation medium, the transfer impedance, as derived from transmission-line theory, is, for all practical purposes, given by

$$Z_m = R_m\left[1 - j\,\frac{d^2}{3\delta^2} - \frac{7}{90}\,\frac{d^4}{\delta^4} - \ldots\right], \qquad (6)$$

where

Z_m = transfer impedance, ohms
R_m = d-c resistance of the annulus, ohms
d = film thickness, centimeters.

If at any given frequency $d \leq 0.5\delta$, the r-f current penetration is very nearly complete and the r-f impedance differs from the d-c resistance by less than 1 percent.

3. Fabrication Problems and Tests

There are several problems common to all methods described in this report for fabricating low resistances from thin films. Because these difficulties impose limitations upon the usefulness of the completed element, and may even render it useless, each of these problems will be examined. However, the specific solutions will be presented later in the discussion of fabrication techniques.

3.1. Radio-Frequency Characteristics and Stability

The r-f impedance of a resistor element will be frequency-sensitive if (a) the coaxial electrodes fail to contact the film along uniform concentric rings, that is, if the contact areas are irregular and spotty so that the width of the annulus between them is not uniform, (b) the thickness of the film in the annulus is uneven, or (c) the electrodes overlap some part of the resistor while remaining insulated from it. Any combination of these conditions may be found in a single resistive element. Where condition (a) is found, generally condition (c) also exists. The first produces an unsymmetrical distribution of current in the annulus resulting in a series inductive reactance, whereas the latter, because of the capacitance between the film and the electrodes, foreshortens the r-f current path thereby reducing the r-f resistance. Therefore, these effects tend to compensate each other. Unsymmetrical distribution of the current

in the ring is also caused by uneven film thickness. Resistor instability is caused by poor electrical contact between the film and the electrodes, or results from the flaking off or migration of film particles in the annulus. After sufficient skill is developed in applying the techniques described, the percentage of unstable elements should be very small. Laboratory tests during the past 2 years on resistive elements made from clamped carbon disks, fired-on conductive paints, and evaporated-and-plated films have established that such elements remain stable to ± 1 percent or better.

3.2. Power Dissipation and Mechanical Ruggedness

Because the micropotentiometer is primarily intended for use at levels between 1 and 10^5 μv, it is usually unnecessary to apply more than 100 ma to any resistive element. Experimentally, it was found that all types are capable of carrying at least five times this current without deleterious effects. Therefore, there is no power-dissipation problem.

Resistive elements made by the evaporation and plating technique were more fragile and susceptible to mechanical injury than those made by the other processes. Mechanical shock or abrasion can break the film loose from its supporting base (substrate), to which it is bonded only by the keying action of the film particles. The stresses applied to the center in normal use of all types of elements may cause deterioration of electrical contact to the film, and an unstable element, unless the coaxial electrodes and the separating dielectric are firmly joined.

3.3. Temperature Effect

When the r-f micropotentiometer is used solely in the laboratory where the ambient temperature never varies by more than a few degrees, the error in resistance due to temperature variations will seldom exceed 1 percent. However, a micropotentiometer used in the field may be subjected to a wide range of ambient-temperature conditions. In this case, for resistive materials having a high-temperature coefficient of resistance, errors of 5 to 6 percent are possible. To determine how serious this problem might become, 1-ohm disk resistors made from carbon sheet, 25 ohms per square, evaporated, and plated silver film resistors and disks made from Hanovia fired-on conductive paints (platinum No. 1, platinum No. 14, and silver No. 38) were tested over a temperature range from 5° to 50° C. The mean-temperature coefficient of resistance, α_t, in this temperature range for each of the above materials is presented in table 1.

TABLE 1.

Resistive material	Mean-temperature coefficient of resistance, α_t*
Hanovia silver paint No. 38	3×10^{-1}
Evaporated and plated silver	3×10^{-1}
Hanovia platinum-gold paint No. 1	5.5×10^{-2}
Hanovia platinum No. 14	7×10^{-2}
Carbon sheet, 25 ohms per square	8×10^{-2}

*α_t is the percentage in resistance per deg C.

3.4. Factors Limiting the Resistance Range

For a given resistive material, a resistance range of about 10 to 1 may be obtained merely by using different film thicknesses. Solid films of metal less than 25 mμ thick cannot be relied upon because of a tendency to break up.[5] The metal film may form into droplets because of the surface tension, or particles may migrate until the surface consists of unconnected agglomerates of the metal. Film thickness may be increased as long as the above current penetration requirements are met.

3.5. Initial Tests and Life Tests

It has been found, experimentally, that structural imperfections affecting the stability and frequency characteristics of resistive elements do not ordinarily alter the d-c resistance sufficiently to be detected by simple d-c measurements. A simple and accurate initial test that may be used is to incorporate the element in a micropotentiometer and compare the voltage drop across its output with an accurately known r-f voltage or with the output from other tested micropotentiometers. In figure 3,a the known reference voltage is provided by another micropotentiometer, M_1. Both it and the unknown, M_2, are connected in parallel branches to the same r-f source. Thus frequency drift either in the receiver or the generator has negligible effect. The transfer instrument is any r-f detector, usually a receiver, having a sensitivity of 1 μv, or better. The r-f cur-

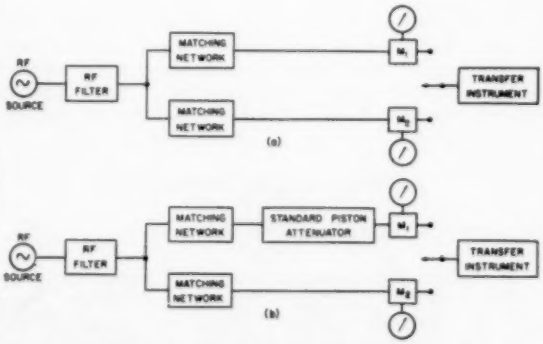

FIGURE 3. *Block diagrams of methods for comparing an unknown micropotentiometer versus a tested one.*

a, Direct comparison; b, comparison of widely different units using a standard attenuator.

[5] Robert G. Picard and O. S. Duffendack, Studies on the structure of thin metallic films by means of the electron microscope. J. Appl. Phys. *14*, 291–305 (1943).

rent into each micropotentiometer is adjusted until the voltage output is the same for both, as determined by the transfer instrument. Then each thermoelement is calibrated with direct current to determine the r-f currents that flowed in the resistive elements, and the output voltages are calculated from Ohm's Law. In matching the output voltages the current levels may reach extremes that are difficult to measure accurately if the resistances of the micropotentiometers are widely different. For example, ambient temperature variations materially reduce the accuracy with which a current of 20 percent or less of the full rated value flowing in a given thermoelement can be measured. A standard waveguide-below-cutoff attenuator is placed in series with the higher resistance micropotentiometer, M_1, as shown in figure 3,b, to keep the r-f-current levels within reasonable limits. The r-f input to each branch is adjusted to give full rated current in the thermoelement of each micropotentiometer, the attenuator in the M_1 branch having been set at some convenient low attenuation level. The r-f output of M_1 is then reduced to match that of M_2 by adjusting the standard attenuator. This is possible because the heater resistance of the thermoelement in the M_1 branch changes by a negligible amount with change in the heater current.

The final voltage output of M_1 is

$$V_{M_1} = V_0 \times \Delta A, \tag{7}$$

where

V_0 = voltage drop across the output of M_1 for full rated current,

ΔA = change in attenuation, as a voltage ratio < 1, required to reduce V_0 to match V_{M_2}.

Differences in the output voltages calculated for each of the micropotentiometers are caused by structural defects.

This same test, repeated at intervals of from 2 to 4 weeks for a period of 6 months, constitutes a test for the quality of fabrication techniques when a process has first been put into operation. From actual tests it was found that a better indication of quality can be obtained at high radio frequencies.

4. Fabrication Processes

4.1. Clamped Elements

A carbon disk clamped to coaxial electrodes provided a very stable type of resistor element. Figure 4 is a partially exploded view of such an assembly. The disk depicted in figure 5 was cut from a commercial carbon sheet consisting of a very thin carbon film deposited on a backing of Bakelite. Because this card material was available in a number of resistance values, it was important to select one that would provide an annular resistive element of reasonable physical dimensions. Fabrication of resistances smaller than 1 ohm was attempted by

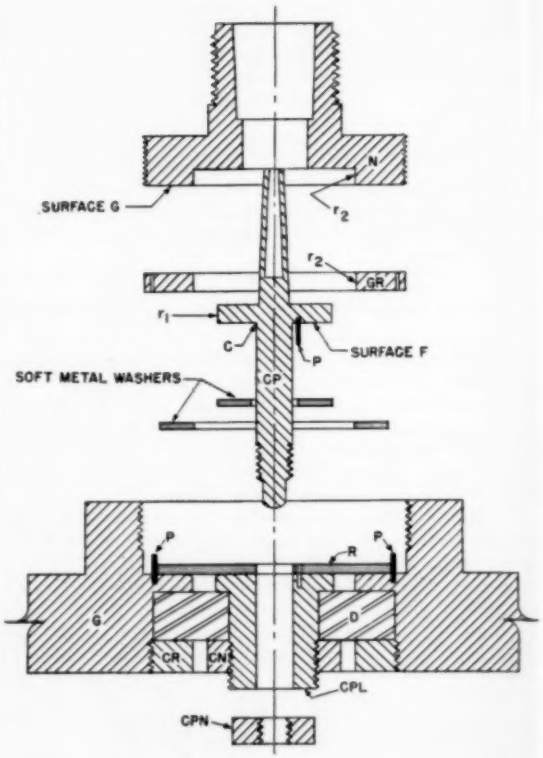

FIGURE 4. *Blown-up view of a clamped-type resistive element.*

CPN, Brass nut; CPL, brass center electrode; GR, brass electrode; CR, brass clamp ring; CN, brass clamp ring; D, dielectric; G, brass ground shell; P, metal pins; CP, brass center electrode; N, brass outer ground shell; R, carbon coaxial resistor.

reducing the width of the annulus, but it was extremely difficult to obtain satisfactory results when the width was made less than 1 mm. As the resistance decreases logarithmically with the decrease in diameter ration, γ, this method was not the correct approach. The reduction in γ necessary to produce an appreciable decrease in resistance resulted in such close spacing of the electrodes that the shunting capacitance between them became rather high. Inasmuch as the resistance per square was known, it was more convenient to determine γ for a particular resistance, R, from eq (8), the equivalent of eq (4), except for rearranged constants.

$$\gamma = \log^{-1}\left(\frac{R}{0.367S}\right), \tag{8}$$

where S is the specific resistance of the carbon sheet in ohms per square. An inner radius, r_1, of $\frac{1}{8}$ in. was used to provide enough area for the center mounting hole, and an adequate contact area for the center electrode. The maximum radius of the disk was made $\frac{1}{8}$ in. larger than r_2 to provide sufficient contact area for the outer coaxial electrode used.

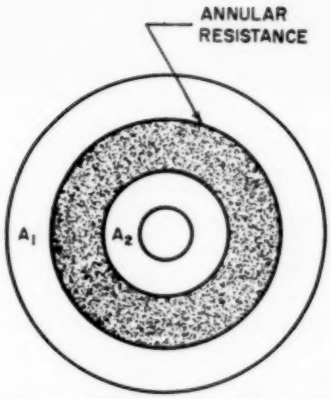

FIGURE 5. *Sketch of a carbon disk for the clamped-type element, showing the annular resistive area and the painted contact rings.*

A_1, Painted ring (outside); A_2, painted ring (inside).

There are, undoubtedly, many ways of cutting disks from the carbon-coated card material. The method used provided quite satisfactory results, whether cutting one or a large number of disks at a time. The sheet material was placed face down on a smooth, flat surface, and squares about ⅛ in. larger than the desired outside diameter of the finished disk were individually cut on power shears. The squares were stacked, clamped between flat metal plates, drilled, and turned to size on a lathe. Air-drying silver paints (Linnick Chemical Co. air-drying silver lacquer or DuPont silver conducting paint No. 4817) were used for concentric areas to be in contact with the electrodes. Either was applied with a camel's-hair brush after masking the annular ring area. High precision in this operation was found unnecessary. The drying process was accelerated by the application of heat from an infrared lamp for a short time.

Returning now to figure 4, parts G, D, CR, CN, and CPL are shown assembled to form the core of the unit. The contact resistance was to be less and remain less than 1 milliohm. It was found important that the surfaces of G and CPL against which the disk was clamped be coplanar, and parallel with the surface F, the faces of GR, and the surface G of part N, and that all were normal to the axis of the assembly. Stable and positive contact between the electrodes and the disk was obtained with tin- or lead-foil washers 2 to 5 mils thick. These washers were cut to fit exactly over the silver contact areas and were placed between the disk and the electrodes GR and CP. In clamping the disk into place, care was taken to prevent turning of the parts. This was accomplished by pinning CP to CPL, and GR to G. The pins used for this purpose fitted loosely so as not to prevent these parts from resting flat against the disk. The shank of CP fitted freely into CPL and surface F was undercut slightly at C for the same reason. In the figure, the edges of the electrodes appear quite rounded. All that was required, actually, was to break the edges enough to remove sharp irregularities that could damage the resistive film and prevent the electrodes from seating properly.

Clamped assemblies were found unsatisfactory for low-value resistance units. Nichrome foil, which had suitable resistivity, was too hard. It failed to form to the electrodes resulting in spotty contact at only a few points. Such a unit, because of lack of electrical symmetry, exhibited reactance at relatively low frequencies. The noble metals that were required as thin foils (2.5 μ thick for resistance of 1 to 10 milliohms) proved to be too soft. Under the pressure of contact, they flowed sufficiently to cause a deterioration of contact to the point where the contact resistance became comparable with the foil resistance.

4.2. Fired Paints

Where stable elements of less than 1 ohm were needed, the construction illustrated in figure 6 produced good results. A dielectric, D, of glass or ceramic, completely covered, except on one end, by a very thin coating of fired-on conductive paint was soldered to the inner and outer electrodes G and P. That portion of the film covering the end of D constituted the resistive annular ring. Inasmuch as the electrodes were soldered directly to the metal film comprising the resistive element, a properly soldered unit was free from the contact resistance difficulties encountered with the clamped assembly. Many conducting paints and pastes of platinum, gold, silver, and combinations of these were tried. Those listed in table 2 were selected because resistive films made from these possessed the requisite stability adhered well to their substrates, and had less tendency to alloy with the solder in the assembling proc-

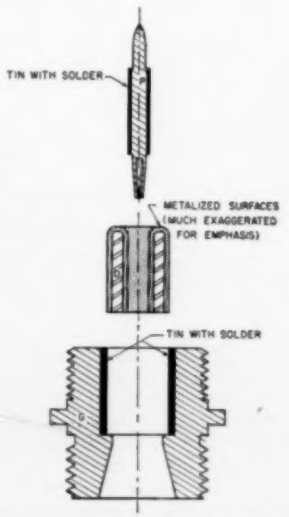

FIGURE 6. *Cross-sectional view of an element using a glass or ceramic sleeve metallized by the fired-paint technique.*

TABLE 2. *Approximate data for using fired paints as resistive elements*

Type of paint	Dilution with turpentine	Substrate	Firing temperature	Resistance obtained	Resistivity (From mfg. data)	Approximate diameter ratios
	Percent		°*F*		*Ohms/cm²*	
Hanovia No. 1 (platinum bright, containing gold and platinum alloyed).	None	Ceramic or pyrex glass.	1,200	0.3 to 0.7 ohms	13 (film 0.1 μ thick).	1.5:1 to 2.3:1.
Hanovia No. 12 (platinum in suspension).	15	Ceramic	1,200 (leave door of oven open until 800° F is reached).	18 milliohms	1	2.3:1.
Hanovia No. 14 (platinum alloy paste).	Up to 50	Pyrex or ceramic	1,200	30 to 43 milliohms	0.75 to 0.85 when thinned 15 percent.	1.5:1 to 2.3:1.
Hanovia 14	Unthinned	do	1,200	10 to 18 milliohms	do	1.5:1 to 2.3:1.
Hanovia No. 38 (silver paste)	10	Gold and glass or ceramic.	1,000 to 1,300	1 milliohm	0.04 (0.1-mil thick film).	2:1.

ess. The information contained in this table was intended to serve merely as a rough guide in the design and construction of elements. In practice, the resistivity of any of these paints varied as much as 100 percent from the values shown because it depended upon such factors as the degree of dilution, the manner of application, the manner of firing, and the condition of the surface of the substrate. Therefore, only an approximation of γ for a particular value of disk resistance could be determined from eq (4).

The first step in assembling a fired element was to select the proper substrate for the particular conductive paint to be used. This was important because many paints are intended for firing to a particular base material. Should this paint be fired on a base for which it was not intended, poor bonding to that base could result, and the finished element would be mechanically fragile. Because the paints fired at a temperature of approximately 1,400° F, only a Pyrex glass or a ceramic material capable of withstanding this temperature without undue stressing or distortion could be used.

Dielectric bushings with end faces perpendicular to their axes were cut from glass or ceramic tubing, using a thin glass-cutting wheel. One end face was polished to provide the smoothest possible surface and its edges were slightly rounded. In the case of glass, this was easily done by fire-polishing the end with the flame of a torch; with ceramic, this was much more difficult and the finished surface was rather porous. Consequently, commercially available glazed ceramic insulators of the style illustrated in figure 7, a, were used. With this configuration for D, the outer electrode, G, needed modification, as shown in figures 7, b, and 8.

Before applying conductive paint to the insulator, the surfaces were thoroughly cleaned with acetone to remove all foreign matter. Once cleaned, the insulator was handled only with tweezers. A single thin coating of conducting paint, properly thinned, was applied with a small brush to all surfaces except the end having the unrounded edges, and care was taken to see that it bridged the rounded edges to form a continuous film. For applying the paint uniformly, the insulator was held vertically in a motor-driven jig, figure 9, and the paint applied as it was slowly rotated. Difficulty was encountered in coating the inside surface of the center hole when the diameter was less than $\frac{3}{16}$ in.

All the paints listed in table 2, with one exception, were fired in the same manner. After the paint had air-dried until it was no longer sticky, the insulator was placed in an electric muffle furnace at room temperature. The furnace was then slowly heated until the firing temperature was reached. When firing Hanovia No. 12, the furnace door was left open until a temperature of about 800° F was obtained to allow a copious supply of air for oxidizing the solvents in the paint. At this point the door was closed and the heating cycle continued until the oven reached the maximum temperature of firing, 1,400° F. When using the other paints listed, it was unnecessary to leave the door open at any stage. Once the furnace arrived at the maximum temperature, it was kept at this heat for about 10 minutes and then allowed to cool slowly to prevent internal stressing of the dielectric during cooling. The platinum-coated insulators were then burnished, washed with acetone, silver contact rings painted on, and refired as before.

Prior to soldering the metallized insulator into its electrodes, the film was burnished with fine steel wool, washed with acetone, and a mask applied to the annular portion to prevent the solder from flowing over it. Sauereisen Cement No. 78 was used. This air-drying compound was thinned with water to the desired consistency and applied by brush to cover the end face and the rounded edges. If these edges had been left unmasked, the solder would have flowed over them to form wedge-shaped extensions to the electrodes, with the result that the r-f resistance at high frequencies would have been more than its d-c value. After the masking had dried, the exposed areas of the film were burnished and washed again and Divco flux No. 300 immediately applied. Any delay in applying this flux may result in contamination of the surface.

The next step was to prepare the electrodes for the assembling operation. They were placed into a duralumin jig, as shown in figures 10, a and b, and 11, to position them so that the insulator could be dropped into place and soldered in. In addition to its function of holding the pieces, the jig conveyed heat by conduction to both members simultaneously. The pieces were heated only enough to cause the Divco 233 solder to melt and flow smoothly. Then the surfaces indicated in figures 6 and 7, b, were liberally tinned with this solder and the metallized insulator dropped into place between the electrodes

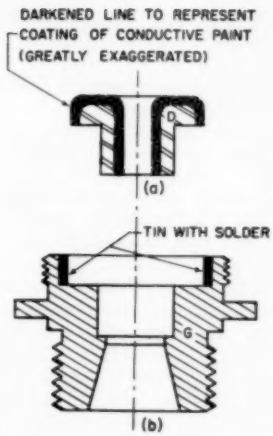

FIGURE 7. *Cross section of commercial ceramic insulator and outer electrode.*

a, metalized surfaces; b, modified construction of outer electrode to fit the ceramic insulator emphasizing areas to be tinned.

FIGURE 9. *A motor-driven jig for painting ceramic buttons.*

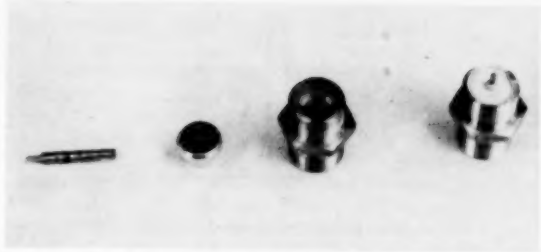

FIGURE 8. *Completed resistive element and its component parts, including the brass outer electrode, the metallized ceramic insulator, and the metal center pin.*

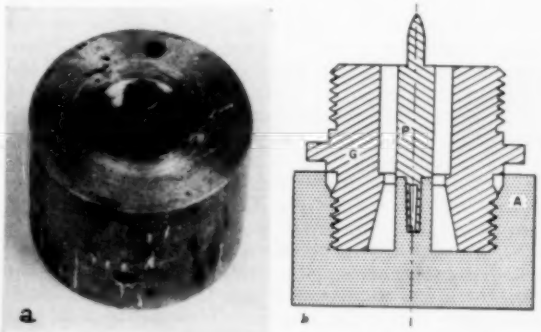

FIGURE 10. *Duralumin jig.*

a, Jig; b, cross section showing coaxial electrodes in place preparatory to soldering the assembly.

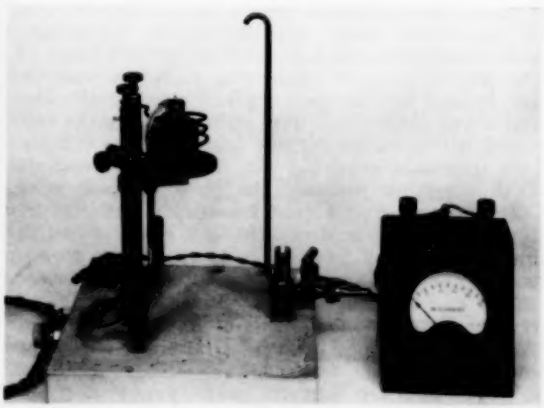

FIGURE 11. *Heating element used for soldering the resistive button to its electrodes, with the dural jig in place and a pyrometer for determining the temperature of the electrodes.*

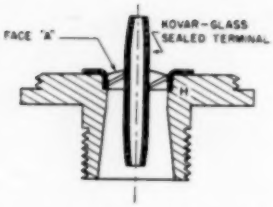

FIGURE 12. *Cross-sectional view of a resistive element using a Kovar-glass seald terminal for the electrodes and supporting substrate for a resistive film.*

Face A is metalized to form the resistive annulus.

and gradually worked about until it was properly seated. The fit between the parts was a loose one to permit the flow of solder between them to form a solid electrical and mechanical bond over the whole circumference of each junction. Very low-temperature melting solder was not found satisfactory as it produced a poor mechanical bond. While enough solder was used to insure good bonding completely around the circumferences of the electrodes, the excessive use of solder often resulted in shorting of the element, the excess flowing through the unit completely and bridging the dielectric on the under side.

When thinning a conducting paint with turpentine, only the amount to be used in a given day was prepared. Where large quantities were prepared at one time and left in storage, the solvents gradually evaporated resulting in a more concentrated mixture which had higher conductivity. Moreover, as the concentration increased, a single coating produced a thicker film. Consequently, elements made at different times from the same mixture had widely different resistance values.

4.3. Evaporated and Plated Elements

Resistive elements of approximately 1 milliohm were also constructed by another method, in which the resistive film was deposited by the evaporation [6] and plating of pure silver on a flat surface consisting of the coaxial electrodes and the separating dielectric. In one type, using this technique, Kovar-glass sealed terminals were used, as illustrated in figure 12. The proper ratio of diameters, γ, for the annular ring formed by the glass surface between the electrodes was determined from eq (4); but, as the ratio varied within rather narrow limits for the different type terminals available, the over-all physical size of the terminal became the prime consideration. Only those having a face reasonably flat and free from sharp irregularities or breaks, especially at the lines of juncture between glass and metal, were used. The terminals selected had all metal surfaces tinned and had an approximate γ of 2:1 and an over-all diameter of about ½ in. with a center electrode, which was tubular. Before soldering one into its brass shell, the center electrode was shaped at both ends into fingered female pins similar to a type N.

[6] H. W. Weinhart and H. G. Wehe, Metal electrodes deposited on quartz crystals by the evaporation process; R. A. Heising, Quartz crystals for electrical circuits, p. 333-355 (D. Van Nostrand, New York, N. Y., 1946)

Better elements resulted when the evaporated and plated silver film was deposited on silver-plated electrodes. Each step necessary in depositing the evaporated and plated film is listed in the following text. To silver plate the electrodes:

a) The tinning was dissolved from the Kovar with HCl.
b) The exposed metal surfaces were scrubbed under tap water using a fine abrasive, and rinsed.
c) A copper flash was applied immediately in a copper-cyanide plating bath (a necessary step since unprotected Kovar oxidized very quickly if left exposed to the air).
d) After rinsing in tap water, a silver strike was applied in a standard silver-cyanide strike solution and this was followed by plating 2 to 5 ten-thousandths of an inch of silver in a standard cyanide plating bath.
e) After rinsing once more in tap water, the surfaces were cleaned with acetone and dried. Then the resistive film was formed as follows:
f) A thin silver film approximately 0.1 μ thick was evaporated upon the entire surface.
g) The silver was built up to a total thickness of no more than 2.5 μ by plating in a standard high-concentration plating bath.

Steps e, f, and g were performed as quickly as possible. A delay between these successive steps of as little as 1 hour was enough for contamination of the surfaces to occur, resulting in poor electrical contact between the film and the electrodes. A final protective coating of lacquer, Krylon, was applied to the surface to prevent mechanical injury.

The second type of unit was similar to that described in the section devoted to the fired-paint technique. After the metallized insulator was soldered between the electrodes, the conductive film on the end of the button was ground away, and the electrodes and the insulator were ground until the face that they presented was flat and free from flaws, particularly where the metal and dielectric joined. Once again, all exposed metal surfaces were silver plated before evaporating upon them. However, when silver was plated directly upon the electrodes, it did not cover the thin ring of solder on the surface at the lines of juncture between the dielectric and metal. All processing steps required in depositing the evaporated and plated film on this type unit are listed below. To cover the electrodes with a silver plate:

h) The metal surfaces were scrubbed under tap water using a fine abrasive and then rinsed.
i) The unit was dipped into 20-percent HCl and rinsed again in tap water.
j) This was followed by a dip into a hot caustic solution (2 percent of NaOH per gallon of water at 150° F).
k) The metal surfaces were then scrubbed and rinsed in tap water.

Upon completion of step k, the remaining steps, namely, copper flashing, silver flashing and silver-plating of the electrodes, the evaporation of the silver

ilm and the final plating were the same as steps c through g. Aluminum, the only other metal tried in this process, gave unsatisfactory results because of poor adherence to the substrata.

5. Conclusion and Implications for Further Work

The processes described above are by no means the only ones by which resistive elements may be fabricated. However, there is sufficient experimental data on resistive elements made by these methods to prove their dependability. A chemical reduction process, commonly known as the silver-mirror process, is presently under consideration. The steps in the procedure are much the same as those outlined in the last section, with the exception that the chemical reduction of silver replaces the final steps of evaporation and plating.

From preliminary tests on a recently completed group of 1- to 5-ohm elements made with fired-on paints, it appears that this may be a simpler method than the clamped carbon type for fabricating high-resistance elements (1 to 10 ohms). Further tests are necessary to determine their stability.

No attempt was made to reproduce resistance values within any specific tolerance. The carbon sheet material used in the clamped assemblies has a specified tolerance of ± 10 percent, and consequently no element of this construction can be expected to be reproduced closer than this. The process that probably would lend itself best to close resistance tolerances is the one using the fired-on paints. It is conceivable that by controlling the degree of dilution and by using some other means of applying the paint, such as spraying or dipping, resistance values could be reproduced to within 5 to 10 percent.

Credit should be given to Vernon A. Lamb and William H. Metzger, Jr., for their valuable cooperation and technical assistance in investigating the various chemical problems encountered in making thin metallic film.

WASHINGTON, May 1953.

259947—53——2

Journal of Research of the National Bureau of Standards Vol. 51, No. 1, July 1953 Research Paper 2427

Properties of Some Masonry Cement

D. N. Evans, A. Litvin, A. C. Figlia, and R. L. Blaine

Seventeen brands of masonry cement were tested for soundness, strength, consistency, fineness, time of setting, shrinkage, water repellency, water retention, autoclave expansion, air entrainment, and resistance to freezing and thawing. Mortars were proportioned both by weight and by volume. Autoclave tests indicated potential unsoundness in some of the cements. Air entrained in the mortar was effective in increasing the ability to withstand freezing and thawing. The shrinkage of these cements differed greatly. The results of tests indicated also that the properties of these masonry cements were appreciably different from those previously reported in 1934.

1. Introduction

Masonry cements are used in building construction to a greater extent today than ever before. Possible reasons for the popularity are their general availability, the convenience of proportioning and mixing masonry mortars, and their desirable physical properties. Evidence of appreciable changes in the properties of these cements since the 1934 National Bureau of Standards survey of these materials [1]* has been presented by Watstein and Seese [2] and also has been evident in the acceptance-testing-work of the Bureau laboratories. In addition to the development of the materials, new methods and ideas of testing have been devised since the last major revision of the Federal Specification for Masonry Cements. It seemed desirable, therefore, to apply the knowledge of these new test methods and ideas of testing in making a survey of the properties of modern masonry cements before revising the specifications.

2. Scope of Investigation

Tests were made on 17 brands of masonry cement, purchased for the most part from building supply dealers east of the Mississippi River.

The following tests were made as required in Federal Specification SS–C–181b for masonry cement: Normal consistency, time of setting, soundness, strength, water retention, and water repellency.

In addition to these specified tests, determinations were also made of the fineness by the No. 325-sieve and air-permeability methods, soundness of neat cement pats in steam and of neat cement and mortar bars in the autoclave test, air entrainment, durability in freezing and thawing tests, and volume change of mortar bars and reinforced mortar bars. The freezing and thawing tests were made on mortar bars proportioned with 1 part of cement to 3 parts of blended sand, by volume. The other mortar tests were made on mortars proportioned both by volume and by weight.

*Figures in brackets indicate the literature references at the end of this paper.

3. Materials Tested

Cements. The 17 brands of masonry cement tested were purchased in 1947 at a time when cement was scarce, so these cements probably had no warehouse deterioration, and represented the product as manufactured. An attempt was made to get as many different types of cements as possible. The present selection of brands is not, however, representative of the quantities of the various types, as the authors have been informed that approximately 90 percent of the masonry cement sold at present is of the portland-cement-base type. Of the cements tested, Nos. 6 and 12 are believed to be largely natural cement; No. 7 is believed to contain some natural cement; No. 8 is believed to be a slag cement; and No. 15, a mixture of portland cement and lime. The others are believed to be mixtures of portland cement and limestone or raw mix.

Sand. The sands used were standard Ottawa silica sands, both "20–30" and "graded". The 20–30 Ottawa sand was used in the air-entrainment mortars (1 to 4) and in the mortars for compressive-strength tests (1 to 3, by weight). Mortars proportioned by volume were prepared with 1 part of cement and 3 parts of blended sand (one-half 20–30 Ottawa sand and one-half graded Ottawa sand).

4. Method of Testing

(a) Fineness on a No. 200 sieve, time of setting, soundness of pats in air and water, compressive strength of cubes (1 to 3, by weight) water retention, and water repellency were determined by the methods given in Federal Specifications SS–C–181b.

(b) The following tests were made according to the methods given in Federal Specification SS–C–158, with the exceptions as noted: Fineness on No. 325 sieve and by air-permeability method, soundness of pats in steam and of neat cement bars and mortar bars in the autoclave,[1] and air entrainment.[2]

(c) The following tests were made of the mortars proportioned by volume: Autoclave expansion at 7

[1] Specimens were removed from the molds at 48 hr and soundness determinations were made at 48 hr rather than 24 hr.

[2] The mortar in the air-entrainment test was tamped with a 1 by ½ in. tamper instead of a rod.

days, compressive strength, freezing and thawing, water retention, water repellency, and volume change of mortar bars and reinforced mortar bars.

The weights of the materials for the 1 to 3 by volume mortars were calculated by assuming the weight of a bag of cement to be the weight per cubic foot and assuming the dry weight of sand in 3 ft^3 of loose damp sand as being 240 lb. This proportion was selected because it is the usual recommendation in mortar specifications to mix 1 sack of masonry cement with 3 ft^3 of sand for masonry mortar. The sand used was a blend of one-half 20–30 and one-half graded Ottawa sand, with a fineness modulus of approximately 2.40. This sand is also the same as that required in the standard method of test for measuring mortar making properties of fine aggregate ASTM designation C87–47. This blend more nearly approximates masonry sand than does 20–30 Ottawa sand specified for the compressive strength test in Federal Specification SS–C–181b.

The mortars were mixed in a model C–10 Hobart mixer with a special paddle constructed with side strips of bronze attached to a center strip. The side strips were covered with sections of rubber tubing of such length that the ends brushed the side of the 3-qt bowl in which the mortar was mixed. The cement was added to the water in the mixing bowl and mixed for 30 sec. About half the sand was added and mixed for 30 sec. The rest of the sand was then added and mixing was continued for 60 sec. The mortar was then allowed to stand for 90 sec, with the bowl and mortar covered with a damp cloth, and then was remixed for an additional 60 sec, and the cubes were made in the regular manner.

It should be noted that the mortars used in this investigation are not the same as the mortars used in the investigation by Rogers and Blaine [1], and hence the results are not directly comparable. Of the 3 mortars used in the earlier investigation, 1 mortar was proportioned by weight, 1 part of cement to 3 parts of 20–30 Ottawa sand, the other 2 were proportioned 1 part of cement to 3 parts of mixed sand, 1 by weight and the other by rodded volume. The mixed sand was composed of 2 parts of 20–30 Ottawa sand to 1 part of pit-run Ottawa sand, the mixed sand having a fineness modulus of 2.62. The sand and cement were hand mixed in a metal vessel, water was added and the mixing continued for 5 min. After standing for 14½ min, they were again stirred for ½ min.

In the tests described herein, cubes were stored in the moist cabinet for 7 days, after which specimens for test at 28 days and 1 year were immersed in water at 70° F. Specimens to be tested after 1 year in air were stored in the laboratory air at 70° F and 50-percent relative humidity after the first 7 days. Six cubes were tested at each age after each condition of storage.

Specimens for the freezing and thawing test were mortar prisms 2 by 2 by 12 in. After 48 hr they were removed from the molds and stored in water for 12 days, then in laboratory air for 14 days. At the age of 28 days they were placed in water in 2¼ by 2¼ by 13-in. noncorroding metal containers and stored at 40° F for 48 hr. Then the containers holding the specimens were placed in rapidly circulating ethylene glycol at −20° F for 2 hr, then in the 40° F bath for 2 hr. Two freezing cycles were made each day. Specimens were stored at 40° F overnight and over weekends. After each five freezing cycles, each bar was weighed and sonic measurements [3, 4] were made. Measurements were continued to 100 cycles, except for bars broken prior to 100 cycles. Only 16 cements were used as there was not enough of cement 2 for this test.

(d) Two sets of mortar prisms 1 by 1 by 11 in. were made of the mortar of each cement. Reference points were placed in the ends of each of one set of prisms for length measurement, leaving an effective length of 10 in. between the inner ends of the points. Cold-rolled steel rods ¼ by 11¾ in., threaded the full length except for rounded ends, were imbedded in the other set of prisms, the rounded ends serving as reference points for length change. Molds were removed at 48 hr, and after an additional 5 days of storage in the moist closet, the prisms were placed in water at 70° F for 21 days, and then in air at 70° F and 50-percent relative humidity. Length measurements were made at 7 and 28 days and at frequent intervals thereafter until apparent equilibrium was reached. Examination of the reinforced prisms was made for evidence of cracking.

5. Results of Tests

Data on weight per bag, density, fineness in terms of percentage of weight of cement retained on No. 200 and No. 325 sieves, specific surface as determined by air permeability, normal consistency, initial time of set, and autoclave expansion of both neat cement and mortar are presented in table 1 for all 17 cements.

TABLE 1. *Weight, density, fineness, normal consistency, setting time, and linear autoclave expansion of 17 masonry cements tested*

Cement	Bag weight	Specific gravity	Weight retained on sieve No.—		Fineness (air permeability)	Normal consistency [a]	Initial setting time	Linear autoclave expansion	
			200	325				Neat cement	Mortar
	lb		*%*	*%*	*cm²/g*		*hr/min*	*%*	*%*
1	70	2.91	2.8	7.5	5,920	23.6	4:15	0.11	0.10
2	70	2.86	1.1	6.4	6,650	25.2	4:15	.16	.07
3	75	2.83	1.1	5.1	7,470	28.0	3:20	.56	.14
4	70	2.93	2.4	10.2	5,620	24.6	3:40	.01	.04
5	70	2.91	.7	2.7	6,370	29.0	4:25	.11	.05
6	65	2.87	5.8	13.8	9,490	33.2	5:10	6.2	1.60
7	70	2.90	1.3	4.8	5,550	29.6	4:20	0.64	0.18
8	80	2.78	.4	1.7	5,880	30.8	4:25	.03	.03
9	70	2.91	6.5	15.1	5,360	24.4	4:10	.08	.07
10	75	2.92	4.3	7.7	9,730	27.4	3:20	.03	.02
11	70	2.90	1.3	9.5	5,470	37.0	3:55	.12	.03
12	62.5	2.75	14.6	24.2	6,970	25.8	4:35	.16	.10
13	70	2.85	0	0	6,600	28.0	4:35	.16	.09
14	70	2.94	.5	1.9	7,110	26.2	4:35	.07	.07
15	62.5	2.72	17.5	25.0	6,850	25.2	3:45	.18	.08
16	70	2.90	4.0	11.2	6,840	27.4	7:30	.03	.03
17	70	2.93	6.3	13.4	7,470	25.2	4:25	.05	.04

[a] Ratio of weight of water to weight of dry cement times 100 required for penetration of 10 mm in the Vicat test.

TABLE 2. *Air entrainment, water retention, water repellency, 24-hour absorption and durability and weight loss in freezing and thawing*

Cement	Air entrainment	Water retention		Water repellency		Water absorption at 24 hr		Freezing and thawing	
	1:4 by volume	1:3 by weight	1:3 by volume	1:3 by weight	1:3 by volume	1:3 by weight	1:3 by volume	Durability factor [4]	Weight loss 100 cycles
	%	%	%	%	%	%	%		%
1	27.9	78	77	33	46	6.2	6.7	100	8.7
2	20.2	82	74	61	33	5.9	8.2		
3	7.3	83	76	48	54	8.8	9.0	[a] 14	[b] 17.2
4	20.1	78	68	39	41	6.8	7.5	100	8.2
5	16.7	69	74	42	37	5.0	5.3	100	4.7
6	18.2	87	86	64	76	11.1	10.7	100	4.1
7	19.0	69	68	37	34	9.0	9.3	100	10.4
8	3.7	59	60	70	34	24.0	9.1	[c] 9	9.4
9	15.1	68	54	43	52	7.3	7.8	100	3.9
10	23.9	86	90	33	34	4.6	5.9	100	7.6
11	14.0	66	63	33	42	6.1	6.2	94	19.3
12	15.3	74	73	26	55	10.2	9.2	100	3.3
13	19.4	73	77	30	36	6.9	7.1	97	11.6
14	29.0	67	76	36	37	6.6	6.9	100	8.6
15	4.8	76	59	30	67	10.1	9.7	[d] 3	[e]
16	10.8	76	78	53	55	10.1	9.3	100	15.6
17	23.5	88	87	34	32	5.2	5.5	100	9.1

[a] Failed at 30 cycles, disintegrated at 70 cycles.
[b] Weight loss at 65 cycles.
[c] Failed at 20 cycles.
[d] Failed at 5 cycles.
[e] Disintegrated at 10 cycles.

TABLE 3. *Compressive strengths and water requirements of mortars made with Ottawa silica sand*

Cement	1:3 by weight mortar			1:3 by volume mortar					Shrinkage of neat cement bars
	Compressive strength		Water requirement[a]	Compressive strength at—				Water requirement[a]	
	7 day	28 day		7 day	28 day	1 year (air)	1 year (water)		
	psi	*psi*		*psi*	*psi*	*psi*	*psi*		%
1	1,220	1,530	40	1,210	1,380	1,890	1,680	39	0.102
2	1,000	1,280	43	920	1,130	1,380	1,360	42	.077
3	1,030	1,430	49	1,030	1,540	2,750	1,850	48	.089
4	1,610	2,090	42	1,340	1,810	2,530	2,180	42	.082
5	1,980	2,330	46	1,830	2,160	3,380	2,280	44	.100
6	370	800	56	310	690	1,220	1,270	50	.108
7	770	1,220	51	710	1,040	2,030	2,120	48	.098
8	1,440	2,810	48	1,690	3,160	3,730	4,480	46	.102
9	1,030	1,520	44	860	1,320	1,610	2,000	43	.075
10	1,780	2,390	47	1,610	2,190	3,050	2,600	45	.129
11	1,830	2,870	56	1,700	3,000	3,310	4,275	52	.155
12	930	1,560	51	620	1,060	2,490	2,090	44	.078
13	1,570	2,050	44	1,410	1,840	2,250	2,030	41	.073
14	1,370	1,910	42	1,040	1,450	1,760	1,740	40	.076
15	820	1,390	50	460	850	1,240	1,500	47	.138
16	1,070	2,040	50	960	1,740	1,750	2,970	49	.130
17	1,450	1,640	46	1,270	1,620	1,950	2,010	44	.116

[a] Ratio of weight of water to weight of dry cement times 100. (Water required for normal flow of mortars).

Values for air entrainment, water retention, water repellency, and water absorption determined on mortars proportioned by weight and volume, as well as durability factors and weight loss resulting from freezing and thawing are given in table 2 for the same cements.

Additional data comprising compressive strength at several ages for mortars proportioned 1:3 by weight and by volume, together with their water requirements, are given in table 3. This table also presents data on shrinkage of neat-cement prisms, as well as the water requirement. A selection of the data on shrinkage is presented graphically in figure 1.

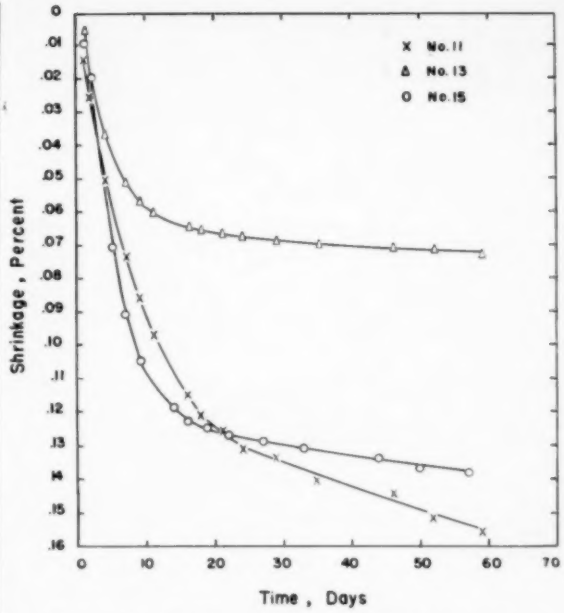

FIGURE 1. *Shrinkage of motar bars (3:1 by volume).*

Stored in air at 70° F. and 50-percent relative humidity. Initial length measured at age of 21 days upon removal from wet storage.

6. Discussion

Weight of Cements. The weight per bag ranged from 62.5 to 80 lb, and for 11 of the 17 masonry cements was 70 lb. In the investigation by Rogers and Blaine [1], the weights of 41 masonry cements, as rodded into a box, ranged from 39.7 to 89.9 lb/ft^3, the mean weight being 64.7 lb. No direct comparison can be made, as the rodded weight per cubic foot was not determined in this study, and the specific gravity was not determined in the 1934 investigation.

Specific gravity. Specific gravities of the cements ranged from 2.72 to 2.94, appreciably lower than the specific gravity of portland cement, which is approximately 3.15.

Sieve fineness. Residues on the No. 200 sieve ranged from 0.0 to 25.0 percent by weight. Only two cements failed to meet the requirement of Federal Specification SS-C-181b that not more than 12 percent of the cement shall be retained on the No. 200 sieve. Three cements had residues of 15 percent or more on the No. 325 sieve. In the 1934 investigation the residue on the No. 325 sieve was reported as: 7 having less then 10 percent, 13 having 10 to 15 percent, 14 having 15 to 25 percent, 2 having more than 40 percent, and 3 not reported. Determination of the air-permeability fineness was not made in 1934,

but from a comparison of the sieve residues, it may be assumed that the present cements are finer.

Normal consistency. The water requirement for normal consistency ranged from 23.6 to 37 percent, and only 3 cements required more than 30 percent. The water requirement for normal consistency is the ratio of the weight of water to the weight of cement expressed as percentage, for the water-cement paste to produce a penetration of 10 mm by the Vicat needle.

Air entrainment. The amount of entrained air as determined by the method for portland cement, using 1 part of cement to 4 parts of 20-30 Ottawa sand by weight, ranged from 3.7 to 29.0 percent. Four of the cements had air-entrainment values of less than 12 percent, 9 from 12 to 21 percent, and 4, more than 21 percent.

Water retention. Of the mortars proportioned by weight, only 1 had a water retention of less than 65 percent, and of the mortars proportioned by volume, 4 had water retentions of less than 65 percent. A majority of the mortars proportioned by weight showed slightly higher water retention than the mortars proportioned by volume, although there were exceptions.

Air-permeability fineness. The fineness of the cements as shown by the air-permeability method ranged from 5,360 to 9,730 cm^2/g, with an average of about 6,780. Masonry cements as a group are much finer than portland cement (about 2,700 to 3,500 cm^2/g by the same method). The air-permeability fineness of the masonry cements does not appear to be related to the sieve residue or to other properties, such as strength, water requirements, water retention, or water repellancy.

Time of setting. The time of initial set varied from 3 hr 20 min to 7 hr 30 min. All cements reached final set in less than 24 hr.

Soundness. The test for soundness of pats in air, water, and steam did not indicate any evidence of unsoundness of any of the cements. However, it should be pointed out that these soundness tests for neat-cement pats are not sufficiently severe to distinguish between any of the cements tested. On the other hand, the autoclave expansion of neat-cement prisms, tested at 48 hr, ranged from 0.03 to 6.2 percent, with 3 cements having expansion greater than 0.50 percent, 7 having expansion less than 0.1 percent, and 7 having expansion between 0.1 and 0.2 percent. The autoclave expansions of the mortar bars proportioned by vloume and tested at the age of 7 days, though lower, fell for the most part in the same order as those of the corresponding neat cements.

In the investigation of white-coat plaster failure by Wells, Clarke, Newman, and Bishop [5], it was shown that the failures were caused by the delayed hydration and resulting expansion of the magnesia in the dolomitic lime. It was also shown by Wells, Clarke, and Levin [6], in their study of the expansive characteristics of hydrated limes and the development of a test for soundness, that expansion of the autoclaved bars was dependent not only on the amount of unhydrated magnesia but also on the strength of the test specimens. The limits suggested by these authors for the autoclave expansion of 1:1 cement to lime (by weight) prisms was 1 percent. In the present investigation of masonry cements only 1 of the 17 cements had an autoclave expansion of more than 1 percent.

The causes of lack of bond and appearance of spaces between the brick and mortar bed have been discussed at considerable length by Palmer [7], Davis and Troxell [8], and others. A recent paper by J. W. McBurney, "Cracking in masonry caused by expansion of mortar" [9], questions the assumption that cracking is necessarily caused by shrinkage. He shows that the openings between bricks and mortar usually ascribed to mortar shrinkage result actually from the mason's techniques in "cutting" joints. He reports damaging expansions resulting from delayed hydration of free magnesium oxide in masonry mortar.

Water repellency. The ratio of 1-hr absorption to 24-hr absorption was less than 0.9 in all cases, and ranged from 0.33 to 0.64 for mortars proportioned by weight, and from 0.32 to 0.76 for mortars proportioned by volume. The water absorbed at 24 hr ranged from 2.5 to 11.1 percent for mortars proportioned by weight, and from 5.3 to 10.7 percent for mortars proportioned by volume. The rate of absorption and total water absorbed usually was lower for mortars proportioned by weight, although there are some exceptions. The results of the water-repellency test in this investigation are in marked contrast to those reported by Rogers and Blaine. They tested cements for absorption in mortars X (1 cement to 3 parts 20-30 silica sand by weight) and mortar Y (1 part cement to 1.5 parts 20-30 silica sand and 1.5 parts pit-run silica sand). Of the mortars proportioned by weight, one crumbled when placed in water and 20 reached 90 percent of the 72-hr absorption in 1 hr or less. Of the mortars proportioned by volume, 2 crumbled when placed in water, and 26 reached 90 percent of the 72-hr absorption in 1 hr or less. This high rate of absorption was related by them to the failure in 10 cycles or less in the freezing and thawing test and resulted in the development of the water-repellency test that was included in Federal Specification SS–C–181a. They also noted that cements having water-repellent additions produced mortar having entrained air, and that most of these were resistant to freezing and thawing. It was also noted that with one exception all specimens having low strengths (less than 500 psi at 28 days) showed poor resistance to freezing and thawing, the one exception being a mortar having a high percentage of entrained air and a low rate of absorption.

Freezing and thawing. Determinations of the loss of weight and of the sonic modulus were made after each 5 cycles of freezing and thawing. Mortar prisms of cement 15 showed a failure at 5 cycles (decrease of 30 percent of the modulus of elasticity, as shown by sonic measurement) [4] and were so badly crumbled at 10 cycles that no further tests could be made. Mortar prisms of cement 8 had a

weight loss at 100 cycles of only 9.4 percent. However, the durability factor was only 9, and the sonic measurement indicated failure at 20 cycles. Mortar prisms of cement 3 had a weight loss of 17.2 percent at 65 cycles and were broken at 70 cycles, and failure was indicated at 30 cycles. The three cements that failed in the freezing and thawing test all had air-entertainment values of less than 8 percent. The tests were discontinued at 100 cycles. None of the cements used in this study had the high rate of absorption (90 percent of 24-hr absorption in 1 hr) or the low strength (less than 500 psi at 28 days) that were noted in several of the cements tested in 1934. The freezing and thawing test in this investigation shows a relation between entrained air and resistance to freezing and thawing but does not appear to show a good relation between rate of absorption or weight loss and resistance to freezing and thawing. Possibly a better relation of the tests would have been shown had the freezing and thawing tests been carried further. The freezing and thawing test is a rather severe shock test and may not have the same effect on mortar prisms cast in nonabsorbent molds that natural weathering has on mortar placed between bricks.

Compressive strength. Of the 17 cements tested, only cement 6 would be classed as a type I masonry cement (not less than 250 and 500 psi at 7 and 28 days, respectively). When the mortar cubes were proportioned by volume both cements 6 and 15 failed to meet the requirements (500 and 1,000 psi at 7 and 28 days, respectively) for type II masonry cement. For mortars proportioned by weight, the 7-day strength ranged from 370 to 1,980 psi, the 28-day strength from 800 to 2,810 psi; and the increase between 7 and 28 days ranged from 190 to 1,370 psi, or from 13 to 116 percent. The strength of the mortars proportioned by volume ranged from 310 to 1,830 psi at 7 days and from 690 to 3,160 psi at 28 days, with the increase in strength between the two ages ranging from 170 to 1,470 psi, or 14 to 122 percent. For the 12 cements that are believed to be portland cement and limestone, the mortars proportioned by weight had strengths ranging from 1,000 to 1,830 psi at 7 days and from 1,280 to 2,870 psi at 28 days, the increase in strength being from 190 to 1,040 psi, or from 13 to 90 percent. The compressive strength of specimens of 7 of the cements stored for 1 year in air appears to be appreciably higher than the corresponding specimens stored in water for 1 year. It is known that the degree of saturation of a specimen at the time of breaking affects the strength. Although the air-cured specimens were soaked before breaking it is not known whether the degree of saturation was the same in both sets. There is also the possibility that some specimens that were high in lime or limestone may have been weakened by leaching due to prolongued water storage. In the investigation in 1934, no attempt was made to bring the strength specimens stored in air and water to the same degree of saturation before breaking. The conclusion in the 1934 investigation was that air storage usually gave higher compressive strengths than water storage.

Water requirement. The water (expressed as percentage of dry weight of cement) required for a flow of 100 to 115 is shown in table 3. The mortars proportioned by volume appear to require slightly less water than the corresponding mortars proportioned by weight. The difference is not large enough to have much significance due to the wide range of flows used (from 100 to 115). The percentage of water required for normal flow of the masonry-cement mortars is about the same as that required for portland cement.

Shrinkage. The unreinforced mortar prisms had shrinkages ranging from 0.073 to 0.155 percent in 60 days. About three-fourths of this shrinkage occurred in the first week, with little change after 28 days. The change of length (shrinkage) against time is presented graphically in figure 1 for mortars made from cements, which represent the extremes of those tested. Note that cements 11 and 15 are alike in having high shrinkage but differ in rate of shrinkage at both early and late ages. Attention should be called to the probability that "The volumetric changes of a mortar cast in a non-absorbent mold and stored in air is no criterion to the volumetric changes that may be expected to occur in the same kind of mortar when used as the joint material in brickwork," a conclusion reported by Davis and Troxell (8).

The reinforced mortar prisms showed a shrinkage of 0.02 to 0.05 percent as evidenced by compression of the reinforcing rods. With the threaded rods, the cracks formed were for the most part extremely small and difficult to see. This is in contrast to the work reported by Watstein and Seese (2), who used regular reinforcing rods. Presumably, the regular rods with deformations at greater intervals caused larger and more widely spaced cracks. The study by Watstein and Seese also indicated that for masonry cements of comparable compositions, the shrinkage increased with the amount of water used. Their work also indicated that the resistance to cracking was increased with increased strength of the mortars and was lowered with increased shrinkage of the mortars. Their study included the bond between bricks and mortars and indicated that both high compressive strength and good water retention are important in producing high binding strength in brick assemblages. Adequate compressive strength are required in masonry mortars to insure load-bearing capacity, and a balance between strength and water retention is necessary to obtain a good bond between the brick and mortar.

General. Masonry cements may be made of one or more of a number of different proportions. For a cement of a given composition, the relation between different properties, such as fineness and strength, water requirement, and water retention, can be shown. For a large group of masonry cements of different materials and various amounts, the relationship becomes obscured by the properties of the different materials.

This study indicates that mortars proportioned by weight did not always have higher strength, water retention, and water repellency than the correspond-

ing mortars proportioned by volume. Both mortars made with cement 8 had the same weight of cement, and the higher strength of the mortars proportioned by volume is largely due to the difference in sand. With the other factors the same, the blended sand tends to produce stronger mortars than the 20–30 sand, as the smaller voids permit a more dense structure (1). Some of the differences between the mortars proportioned by weight and by volume are not of sufficient magnitude to be considered significant.

Some of the differences that may be noted between the masonry cements tested in 1947 and those tested in 1934 are: a marked tendency toward higher strength and slower rates of absorption, waterproofing agents have probably been largely replaced by air-entraining agents, it is probable that the majority of masonry cements now being made contain air-entraining agents, and most of the cements tested showed a good resistance to freezing and thawing.

7. Summary

Tests were made of 17 brands of masonry cements representing materials of different types. The results of tests were as follows:

1. The masonry cements tested had weight-per-bag values ranging from 62½ to 80 lb.

2. The specific gravity of the cements ranged from 2.72 to 2.94 percent.

3. The residue retained on a No. 200 sieve ranged from 0.0 to 17.5 percent, and on a No. 325 sieve the residue ranged from 0.0 to 24.2 percent. The fineness, as determined by the air-permeability apparatus, ranged from 5,470 to 9,730 cm^3/g. There was no relation between fineness and other properties of the cements.

4. All the cements attained final set within 24 hr.

5. The compressive strength of 2-in. cubes proportioned 1 to 3 by weight ranged from 310 to 1,980 psi at 7 days, and from 690 to 3,160 psi at 28 days. The 12 masonry cements of portland cement-base type had strengths ranging from 1,000 to 1,980 psi at 7 days and from 1,280 to 2,870 psi at 28 days. Strengths of mortars proportioned 1 to 3 by weight were slightly greater than those proportioned by volume. The 1-year tests indicated an appreciable increase in strength for most cements with both air and water storage.

6. The water-repellency values for the mortars proportioned by weight ranged from 0.26 to 0.70, and from 0.32 to 0.76 for mortars proportioned by volume. The requirement of Federal Specification SS–C–181b for water repellency is that the ratio of the 1- to 24-hr absorption shall not exceed 0.90.

7. Of the mortars proportioned by weight, only one had a water retention of less than 65 percent, and of mortars proportioned by volume, 4 had water-retention values less than 65 percent.

8. The air content of 1 to 4 mortars ranged from 3.7 to 29.0 percent.

9. Three of the cements having less than 10 percent of air in the 1 to 4 mortar had a very low durability factor. Only 2 of the 11 cements with more than 15 percent of air in the 1 to 4 mortar had a weight loss of more than 10 percent in 100 freezing and thawing cycles, and all had a very high durability factor.

10. Mortar bars of the different cements proportioned 1 to 3 by volume had shrinkage ranging from 0.075 to 0.16 percent in 60 days.

11. Neat pats made of these cements exhibited satisfactory soundness in both air and steam. The expansion of neat-cement bars as a result of autoclave treatment ranged from 0.03 to 6.2 percent. Fourteen of the cements had an expansion less than 0.20 percent, the expansions of the other 3 were 0.56. 0.64, and 6.2 percent.

8. References

[1] J. S. Rogers and R. L. Blaine, Investigation of commercial masonry cements, J. Research NBS **13,** 811 (1934) RP746.

[2] D. Watstein and N. A. Seese, Jr., Properties of masonry mortars of several compositions, ASTM Bul. 117 (August 1947).

[3] Gerald Picket, Equations for computing elastic constants from flexural and tortional resonance frequencies of vibrations of prisms and cylinders, ASTM Proc. **45** (1945).

[4] S. Walker, Freezing and thawing tests of concrete made with different aggregates, Am. Concrete Inst. Proc. **40,** 573 (1944).

[5] L. S. Wells, W. F. Clarke, E. S. Newman, and D. L. Bishop, Investigation of white-coat plaster failures, NBS Bldg. Materials and Structures Report 121 (1951).

[6] L. W. Wells, W. F. Clarke, and E. M. Levin, Expansive characteristics of hydrated limes and the development of an autoclave test for soundness, J. Research NBS **47,** 179 (1948) RP1917.

[7] L. A Palmer, Volume change in brick masonry materials, J. Am. Ceramic Soc. [8] **14,** 541–561 (August 1931).

[8] R. E. Davis and G. E. Trovell, Volumetric changes in portland cement mortars and concretes, proceedings, Am. Concrete Inst. **25,** 210–255 (1929).

[9] J. W. McBurney, Cracking in masonry caused by expansion of mortar (ASTM Preprint 101 (1952)). Proc. ASTM **52,** 1228 (1952).

Washington, October 20, 1952.

Journal of Research of the National Bureau of Standards Vol. 51, No. 1, July 1953 Research Paper 2428

Subsieve Particle-Size Measurement of Metal Powders by Air Elutriation

Rolla E. Pollard

Particle-size measurements of spherical metal powders by means of the Roller air analyzer, using samples up to 40 grams of powder, were found to be reproducible within approximately ±1 percent of the original weight of the sample for particle diameters up to 120 microns. The separation limits closely approximated those required by Stokes law ($V=Kd^2$) for particle diameters of 5 to 20 microns. For particle diameters of 20 to 70 microns, the size limits of fractions conformed approximately to the formula $V=K''d^{1.4}$. With particles larger than 70 microns, the accuracy of separation was uncertain.

Reproducible results also were obtained with irregularly shaped particles, such as those of electrolytic copper powder. However, the accuracy of calculated size limits was uncertain, no attempt being made to check them by other methods of measurement.

1. Introduction

Accurate and reproducible methods of determining particle size are of great importance in powder metallurgy. The size distribution of the particles markedly influences the inherent packing behavior of a powder. This vitally affects the pressing and sintering techniques employed and the properties of the sintered object produced.

Sieves are used almost universally for size analyses of particles large enough to be retained by a No. 325 sieve ($\simeq 44 \pm 3$ microns).

For smaller, or subsieve, particles, other methods of size measurements must be used Among the many methods currently employed, air elutriation has a distinct advantage because dry, sized fractions can be collected and used for further study.

One of the few commercially available devices for determining particle-size distribution by air elutriation is the Roller air analyzer developed by P. S. Roller [1, 2, 3, 4][1] at the U. S. Bureau of Mines. Tentative standard methods of particle-size analysis based on this apparatus are being considered by the Metal Powder Association [5], and the American Society for Testing Materials [6]. The Roller air analyzer has been used at the National Bureau of Standards for several years in connection with studies of the properties of metal powders. An investigation was made to determine the effects of certain variations in equipment and operating technique on the reproducibility of the results obtained and the accuracy of the separations. These variations included time of testing or criterion of end point, condition of interior surface of the settling tubes, particle-size distribution of sample, range of particle sizes within a fraction, size of sample, humidity of air, and particle shape. Two prime objectives of the investigation were to establish the approximate range of application of Stokes law to metal-powder elutriation under the conditions found in the Roller analyzer, and to determine, if possible, the relation between the diameters and falling velocities for particles of larger size.

[1] Figures in brackets indicate the literature references at the end of this paper.

2. Theoretical Background

Particle-size measurement by the Roller air analyzer is based on Stokes' law, according to which the terminal velocity of a particle falling freely in a homogeneous fluid is given by the formula

$$V=Kg\frac{(\rho-\rho_0)d^2}{\mu}, \tag{1}$$

where

V = terminal velocity, cm/sec
K = a constant that depends on the shape of the particle and the nature of the air flow
g = gravitational constant = 980 cm/sec^2
ρ = density of the particle, g/cm^3
ρ_0 = density of the fluid = 0.0012 g/cm^3 for air at 21° C and 760 mm
d = diameter of particle, cm
μ = viscosity of the fluid = 1.82×10^{-4} poise for air.

Stokes' law is strictly valid only for spherical particles and streamline flow. When $K=1/18$, then $V=g(\rho-\rho_0)d^2/18\mu$ or, with air as the fluid and d expressed in microns, $V=0.00299(\rho-\rho_0)d^2$. Under nearly ideal conditions (that is, a single sphere falling in a relatively large cylinder of quiescent fluid) the experimental measurement of the rate of fall of a sphere is a convenient method of determining the value of the viscosity of a fluid. Castleman [7] has analyzed a number of such measurements to determine the range of Reynolds numbers[2] over which Stokes' law gives accurate results. Castleman's mean curve coincides with the curve representing Stokes' law at approximately $R=0.5$. For iron and copper powders in air, this would correspond to diameters of 32 and 31 microns, respectively.

However, such calculations assume ideal conditions not found in an air separator, such as the Roller, where large numbers of particles enter the settling

[2] The Reynolds number, R, represents the ratio of the inertia terms to the frictional terms in the equations of motion of a fluid. In the case of a particle falling in a fluid, $R=dV\rho_0/\mu$.

chambers simultaneously and the movement of individual particles may be influenced or interrupted by the presence of other particles or by the containing wall. The air also possesses motion, which changes in direction and in velocity while in contact with the particles and with the walls of the chamber. Moreover, most particles produced commercially are not true spheroids but are irregular in shape, thus further complicating such tests. In this respect Wadell [8] has found that with nonspherical particles consistent results can be obtained in sedimentation or air elutriation tests only when the Reynolds number does not exceed 0.2 ($R < 0.2$).

3. Method and Materials

The Roller air analyzer consists, essentially, of a device by which powder particles are blown into a settling chamber through which dried and metered air moves at a uniform measurable velocity. Means are provided for collecting the particles carried out of the settling chamber and for removing and recirculating lodged particles. A diagram of the apparatus used in this investigation is shown in figure 1. Low-pressure air is cleaned in the dust trap, H, and the oil trap, G, before being dried in an activated alumina dryer, F. E is a vessel containing a moisture-indicating compound. Air flow is regulated by means of calibrated metering orifices, A, and manometers, C and D. The air stream passing through the jet, J, at high velocity impinges on the powder sample, K. The U tube, M, holding the sample is given a jerky, oscillatory motion by bumper arms rotating on the shaft, L. The oscillating motion of the U tube (288 oscillations a min) continually brings fresh material under the action of the jet and newly exposed powder particles of amenable sizes are blown into the settling tube, P. Theoretically, particles smaller than the selected size are carried out of the tube and collected in extraction thimble Q.

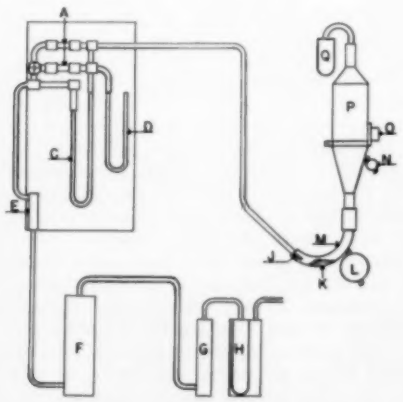

FIGURE 1. *Details of Roller air analyzer assembly.*

During the investigation it was found that alundum extraction thimbles, RA98 (coarse), were definitely superior to the paper thimbles originally used. For example, a paper thimble, during a 120-min run with dried air,[3] but without powders, will gain as much as 0.81 g in weight. This would amount to over 2 percent of the weight of a 40-g sample. During this time an alundum thimble will gain only 0.004 g. Moreover the alundum thimbles can be cleaned readily in nitric acid or aqua regia and reused.

Means are supplied for dislodging and recirculating material that sticks to the walls of the settling chamber by a tapping device, N, with two leather-faced hammers that strike the tube about 870 times a min. Later this device was supplemented by a Syntron vibrator, O, (type V–4, 7,200 vibrations a min).

Four settling tubes with inside diameters of 9, 4½, 2¼, and 1¼ in., respectively, were supplied with the apparatus. The three largest tubes vary in diameter by the ratio of 1/2. Therefore, to the limit of application of Stokes' law ($V = Kd^2$) successive separations made in these tubes at the same rate of air flow would yield fractions whose maximum particle diameter would vary in the same order by the ratio of 2. The same rate of air flow used in the 1¼-in. tube would give an air velocity lower than that calculated by Stokes' law by the ratio of $(1\frac{1}{8})^2/(1\frac{1}{4})^2$. Although it is not specifically mentioned by the manufacturer, it is possible that this change in ratio was intended as a correction for Stokes' law at high air velocities.

The metal powders used in the investigation are listed in table 1. The permalloy powders, PC and PF, were found to be predominantly spherical in shape, 90 to 95 percent of the particles having nearly perfectly circular projected images, as shown in figure 2. A mixture of the two powders (2 parts by weight of PC to 1 part of PF, designated in table 1 as PM) covered the subsieve particle-size range fairly well and was used extensively in checking the accuracy of particle-size analyses by microscopic measurements. The atomized copper and zinc powders were also largely spherical in shape, as shown in figures 3 and 4, respectively. approximately 80 percent of the projected images of these two powders were either circular or slightly elliptical with ratios of minor to major axes of 0.9 or more. It was observed that there was not much difference in size distribution among the several fractions whether the perfectly circular images were measured or the minor axes of all elliptical images were included. The controlling dimension in the separation of these particles, therefore, seems to be the minor axis.

The other powders of table 1 were more or less irregular in shape. For example, the irregular shape of the electrolytic copper, Cu B, powder is shown in figure 5. No attempt was made to check the par-

[3] The term "dried air" refers, in this text, to air dried in an activated alumina dryer to a nominal dewpoint range of −40° to −70° F.

FIGURE 2. *Almost perfectly spherical particles of +40-micron fraction of permalloy-mix powder*

Magnification × 100.

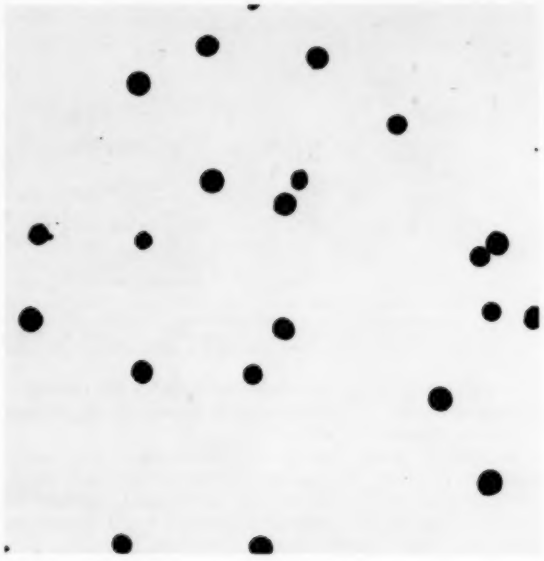

FIGURE 3. *Nearly spherical particles of 30- to 40-micron fraction of atomized copper,* Cu A, *powder.*

Magnification × 100.

FIGURE 4. *Nearly spherical particles of 30- to 40-micron fraction of atomized zinc.*

Magnification × 100.

FIGURE 5. *Irregularly shaped particles of +40-micron fraction of electrolytic copper,* Cu B, *powder.*

Magnification × 100.

TABLE 1. *Description, designation, and pertinent properties of metal powders used in the investigation*

Powder	Designation in text	Source	Method of manufacture	Particle shape	Subsieve	Apparent density	Theoretical solid density
					Percent	*g/cm³*	*g/cm³*
Permalloy, fine	PF	R–B–H Dispersions	Atomization	Spherical	100	2.68	[a] 8.70
Permalloy, coarse	PC	do	do	do	99.5+	4.40	[a] 8.70
Permalloy mix	PM	do	do	do	100−	3.75	[a] 8.70
Copper	Cu A	New Jersey Zinc	do	Nearly spherical	46 to 60	5.26	8.96
	Cu B	Charles Hardy	Electrolytic	Irregular	51 to 59	2.70	8.96
	Cu C	do	do	do	90 to 95	1.61	8.96
Iron	Fe A	Plastic metals	do	do	37 to 46	2.27	7.87
	Fe B1	do	Reduced mill scale	do	32 to 40	2.52	7.87
	Fe F2	do	do	do	35 to 50	2.46	7.87
	Fe C	General Aniline	Carbonyl	[b] Irregular	99+	3.10	7.87
Zinc	Zn	Charles Hardy	Atomization	Nearly spherical	99+	2.03	7.14

[a] Estimated from the nominal composition; Ni, 78.5%; Mo, 3.5%; balance, Fe.
[b] Many individual particles of this powder (GAW, grade C) were spherical, but some of the spheres had grown together during production or sintered together during heat treatment, so that much of the final product was irregularly shaped.

ticle-size distribution of such powders by microscopic measurements. They were used, however, in studies involving reproducibility.

Attempts were made to determine the solid particle density of some of the powders used, according to ASTM D153–39, "Standard Method of Test for Specific Gravity of Pigments". The results were not very satisfactory, however, because the density of the kerosine changed during vacuum treatment to remove air occluded in the powder sample during its introduction into the kerosine. This change in density caused errors in the determination of the true volume of the sample. The range for permalloy powders, for example, was 8.70 ± 0.06 g/cm³. This uncertainty undoubtedly could be reduced by employing suitable liquids of constant boiling point and possibly by using larger samples. It is believed, however, that the true solid density of all the powder particles used in this investigation, with the probable exception of the reduced iron powders Fe B, Fe B1, and Fe B2, are very close to the theoretical solid densities given in table 1.

4. Effects of Variations in Equipment and Testing Procedure on the Reproducibility of Results

4.1. Time of testing—criterion of end point

Separation by air elutriation, like separation by sieving, is never complete. One of the first problems encountered in using the Roller air analyzer, therefore, is the adoption of some convention for establishing an artificial end point. The method originally used by Roller [1, 3, 4] was to operate by 30-min intervals, weighing the amount collected for each interval. His stopping point, or artificial end point, was reached when the weight of powder collected in any interval was less than 10 percent of that collected in the first interval. This method also is recommended in a booklet published by the Metals Disintegrating Co. [9], and is being considered in the tentative standards of the MPA [5] and the ASTM [6]. The manufacturer, in the instructions sent with the apparatus, recommends a similar procedure but with 2-min intervals.

Later Roller [10], working with some ceramic materials, found that when the weight of fraction separated was plotted against the rate of separation, a straight line or characteristic was obtained, that when extrapolated to zero rate, gave the total amount of material of the selected-size range originally present in the sample. The time intervals used for portland cement ranged from ½ to 25 min. Roller [11] has recently applied this end-point method to the particle-size analysis of metal powders, using time intervals as short as 1 or 2 min, which, in the light of the results of the present investigation, appear to be of too short duration.

For example, a number of tests were made with the permalloy powder mix, PM, using time intervals of 2, 4, 8, 15, and 30 min. Some of the tests were stopped after the interval in which the amount collected was less than 10 percent of that collected in the first interval (10-percent end point). Others were continued until the collection per interval was less than 1 percent of the first interval (1 percent end point).

In figure 6 the amounts of the 0- to 10-micron fraction collected during some of these tests are plotted against the rate of separation, according to Roller's method [10, 11]. It will be noted that those portions of the curves representing the early stages of the test (which were used by Roller) tend to flatten out with decreasing time intervals. In the 2-min-interval curve, the 4 points representing the third, fourth, fifth, and sixth intervals may be fairly well represented by a straight line. Extrapolation of this line to zero rate, however, indicates a rather low result, 9.55 g, or 21.4 percent, of a 40-g sample as compared to 27 ± 1 percent as measured by the 10-percent end point.

This may be due, at least in part, to the fact that for very short time intervals the largest particles of the selected size range do not have time to leave the settling chamber. The resultant velocity, V_R, of a particle in a settling tube depends in magnitude and direction on the difference between the velocity of the air, V_A, and the free-falling velocity of the particle, V_F. The 4½-in. settling tube, for example, has a section of uniform diameter about 28 cm in length. In order for a particle to escape from this tube V_R must be greater than $28/60t$ cm/sec, where

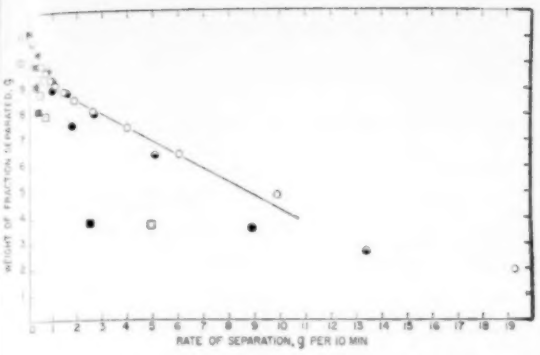

FIGURE 6. *Roller's end-point method applied to 0- to 10-micron fraction of permalloy-mix powder.*

Time intervals: ○, 2 min; ◒, 4 min; ●, 8 min; □, 15 min; ■, 30 min.

t is the time interval in minutes. For a separation of permalloy powder (ρ=8.7) with an air velocity calculated for a nominal particle diameter of 10 microns, it can be shown that the largest particle that could escape from the tube in a given time interval would be 9.1 microns for 1 min, 9.5 for 2 min, and 9.97 for 30 min. For very short time intervals, therefore, the actual separation would be at a diameter appreciably smaller than that for which the air velocity was calculated, and the results would be low, particularly if the size distribution of the sample were such that large numbers of borderline particles would be affected.

The influence of the time interval on the end-point criterion is illustrated in figure 7, which represents all of the tests made on the 0- to 10-micron fraction of the PM powder. The upper and lower solid curves represent, respectively, the highest and lowest values obtained with any time interval within the total testing time indicated on the scale of abscissas. The intermediate broken curves represent the lowest values obtained with 2-, 4-, 8- and 15-min intervals. The total number of tests include: 2-, 4-, and 8-min intervals—4 tests each, with 1 in each case carried to the 1-percent end point; 15-min intervals—8 tests, with 3- to the 1-percent end point; 30-min intervals—67 tests, with 3- to the 1-percent end point.

For tests with time intervals shorter than 30 min, test conditions were uniform, except that in those continued to the 1-percent end point a Syntron vibrator, O, figure 1, was used in addition to the regular hammer, N, figure 1. The 30-min-interval tests, however, included many in which the test conditions were varied considerably. For example, the three points just outside the "knee" of the upper curve (at 30, 60, and 90 min) were obtained without a vibrator but with humidified instead of dried air. Other tests were made with and without the vibrator and with samples varying in size from 20 to 100 g.

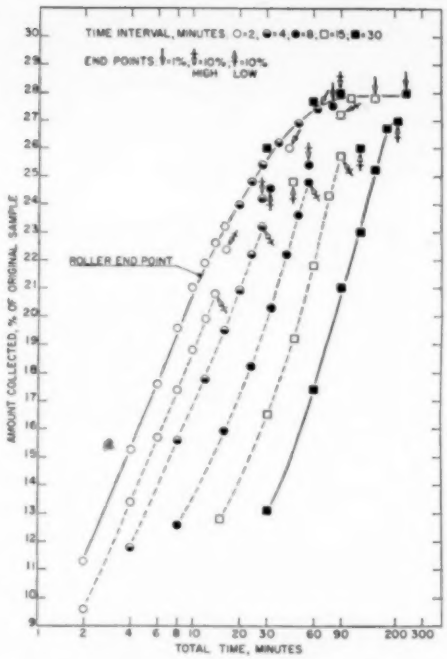
TIME INTERVAL, MINUTES. ○=2, ◒=4, ●=8, □=15, ■=30
END POINTS 1=1%, 2=10% HIGH, 3=10% LOW
ROLLER END POINT
AMOUNT COLLECTED, % OF ORIGINAL SAMPLE
TOTAL TIME, MINUTES

FIGURE 7. *Amount collected versus total time of testing for 0- to 10-micron fractions of permalloy-mix powder with 2-, 4-, 8-, 15-, and 30-min intervals.*

The solid curves represent the range of results obtained in a total of 90 tests. The broken curves represent the lowest values obtained with time intervals indicated by the symbols. The Roller end point is the end point determined in figure 6.

It will be noted that, for the 30-min interval, in spite of a very wide variation in initial separation rate (from 13 to 26 percent per interval), the results tended to converge so that the 10-percent end points (marked with barred arrows) varied no more than ± 1 percent of the original weight of the sample. For the shorter time intervals the 10-percent end points were progressively lower. These results show conclusively that to get within the end-point range of the 30-min intervals, tests with shorter intervals would have to be carried beyond the 10-percent end point. All the 1-percent end points (marked with plain arrows) were within this range except the 2-min interval, which was at the lower edge. Roller's end point (as determined in fig. 6) would be at 21.4 percent on the upper curve of figure 7.

It was concluded from these results that 30-min intervals and the 10-percent end-point criterion were most satisfactory. This procedure, therefore, was adopted as standard for all subsequent tests. Complete Roller analyses of permalloy and other metal powders are given in tables 2 to 9 inclusive.

TABLE 2. *Roller analyses of permalloy mix, PM, powder—40-g samples, minus No. 325 sieve, 30-min intervals, 10-percent end point, dry air*

Fraction (microns)	Number of tests	Diameter of settling tube	Stokes air velocity	Air flow	Average air velocity	Roller analysis—percentage by weight of original sample			Typical microscopic count—percentage by weight of fraction		
						Mean	Maximum deviation from mean	Standard deviation	Undersize	Oversize	Within size limits
Series 1—Tubes as received, hammer only, air velocity partly corrected [a]											
		Inches	*cm/sec*	*L/min*	*cm/sec*						
0 to 5	4	9	0.65	16.0	0.65	7.95	+5.1−2.2	3.00	.....	.....	.....
5 to 10	4	4½	2.6	16.0	2.6	11.75	+8.2−6.7	5.36	.....	.....	.....
10 to 20	4	2¼	10.4	16.0	10.4	42.52	+0.4−0.9	0.54	.....	.....	.....
20 to 40	4	1¼	41.6	16.0	33.7	27.40	+.4−0.5	.34	.....	.....	.....
+40	4	.....	.....	.....	.....	0.90	+.1−0.1	.07	.....	.....	.....
Recovery	4	.....	.....	.....	.....	90.50	+6.9−9.0	6.53	.....	.....	.....
Series 2—Tubes as received, hammer only											
0 to 20	3	2¼	10.4	16.0	10.4	68.9	+1.5−2.3	.....	.....	.....	.....
+20	3	.....	.....	.....	.....	30.5	+2.3−1.3	.....	.....	.....	.....
Recovery	3	.....	.....	.....	.....	99.4	+0.2−0.2	.....	.....	.....	.....
Series 3—Tubes as received, hammer only, air velocity partly corrected [a]											
0 to 10	[b] 30	4½	2.6	16.0	2.6	27.14	+0.6−0.4	0.32	0	0.7	99.3
10 to 20	[b] 30	2¼	10.4	16.0	10.4	43.71	+1.2−1.1	.66	0.6	.9	98.5
20 to 30	8	1¼	23.4	9.0	18.9	18.11	+4.1−4.5	3.13	.3	1.6	98.1
30 to 40	8	1¼	41.6	16.0	33.7	9.64	+4.6−3.5	2.66	24.8	4.7	70.5
+40	8	.....	.....	.....	.....	0.94	+0.3−0.1	0.16	5.8	0	94.2
Recovery	8	.....	.....	.....	.....	99.31	+.4−0.5	.32	.....	.....	.....
Series 4—Tubes as received, hammer and vibrator, air velocity partly corrected [a]											
20 to 30	3	1½	23.4	16.0	23.4	23.03	+1.4−1.0	1.02	0.2	5.7	94.1
30 to 40	3	1¼	41.6	16.0	33.7	6.07	+0.3−0.5	0.33	7.5	10.1	82.4
+40	3	.....	.....	.....	.....	0.70	+.1−0.1	.08	5.3	0	94.7
Recovery	3	.....	.....	.....	.....	99.40	+.2−0.2	.16	.....	.....	.....
Series 5—Tubes as received, hammer only, air velocity partly corrected [a]											
20 to 30	4	2¼	23.4	36.0	23.4	27.15	+1.2−1.0	0.79	0.9	12.4	86.7
30 to 40	4	1¼	41.6	16.0	33.7	1.88	+0.4−0.5	.35	.4	11.6	88.0
+40	4	.....	.....	.....	.....	0.82	+.1−0	.04	.....	0	100
Recovery	4	.....	.....	.....	.....	99.25	+.2−0.2	.15	.....	.....	.....
Series 6—Small tubes lapped, vibrator and hammer, air velocity partly corrected [a]											
20 to 30	10	1½	23.4	16.0	23.4	24.50	+1.2−0.6	0.50	0.1	16.3	83.6
30 to 40	10	1¼	41.6	16.0	33.7	2.70	+0.3−0.3	.18	0	20.8	79.2
+40	10	.....	.....	.....	.....	0.85	+.3−0.2	.16	.4	0	99.6
Recovery	10	.....	.....	.....	.....	99.34	+.4−0.7	.36	.....	.....	.....
Series 7—Small tubes lapped, vibrator and hammer, air velocity corrected ($V=K''d^{1.6}$ above 20 microns)											
20 to 30	5	1½	23.4	12.9	18.7	21.35	+0.5−0.5	0.33	0.6	1.3	98.1
30 to 40	5	1¼	41.6	13.3	27.9	4.54	+.3−0.2	0.18	.6	1.2	98.2
+40	5	.....	.....	.....	.....	1.82	+.5−0.3	0.19	.3	0	99.7
Recovery	5	.....	.....	.....	.....	99.16	+.3−0.4	0.26	.....	.....	.....

[a] Air flow corresponding to Stokes air velocity used in all tubes except 1¼ in., for which the air flow was calculated for 1⅛-in. diameter.
[b] These 30 tests include the 0- to 10- and 10- to 20-micron fractions of series 3, 4, 5, 6, and 7.

TABLE 3. *Roller analyses of atomized copper, Cu A, and electrolytic copper, Cu B, powders, minus No. 325 sieve, 30-min intervals, 10-percent end point, dry air*

Fraction (microns)	Number of tests	Diameter of settling tube	Stokes air velocity	Air flow	Average air velocity	Roller analysis—percentage by weight of original sample			Typical microscopic count—percentage by weight of fraction		
						Mean	Maximum deviation from mean	Standard deviation	Undersize	Oversize	Within size limits
Series 1—Cu B—25-g samples, tubes as received, hammer only, air flow partly corrected [a]											
		Inches	*cm/sec*	*L/min*	*cm/sec*						
0 to 5	14	9	0.67	16.5	0.67	4.92	+0.8−1.3	0.53	.....	.....	.....
5 to 10	14	4½	2.7	16.5	2.7	16.04	+.9−1.0	.56	.....	.....	.....
10 to 20	14	2¼	10.7	16.5	10.7	32.46	+1.4−1.6	.81	.....	.....	.....
20 to 40	14	1¼	42.9	16.5	34.7	37.41	+1.5−2.8	1.11	.....	.....	.....
+40	14	.....	.....	.....	.....	7.42	+2.3−3.9	1.81	.....	.....	.....
Recovery	14	.....	.....	.....	.....	98.19	+1.6−2.0	1.13	.....	.....	.....
Series 2—Cu B—25-g samples, tubes as received, hammer only											
0 to 20	3	4½	10.7	16.5	10.7	49.6	+1.1−1.3	.....	.....	.....	.....
+20	3	.....	.....	.....	.....	50.0	+1.2−1.1	.....	.....	.....	.....
Recovery	3	.....	.....	.....	.....	99.6	+0 −0	.....	.....	.....	.....
Series 3—Cu A—40-g samples, tubes as received, hammer only, air velocity partly corrected [a]											
0 to 5	5	9	0.67	16.5	0.67	0.98	+0.1−0.1	0.08	.....	.....	.....
5 to 10	5	4½	2.7	16.5	2.7	3.94	+.3−0.2	.19	.....	.....	.....
10 to 20	5	2¼	10.7	16.5	10.7	19.30	+.7−0.5	.57	.....	.....	.....
20 to 40	5	1¼	42.9	16.5	34.7	44.28	+3.1−3.0	2.54	.....	.....	.....
+40	5	.....	.....	.....	.....	30.12	+4.5−4.6	3.71	.....	.....	.....
Recovery	5	.....	.....	.....	.....	98.40	+1.3−0.5	0.71	.....	.....	.....
Series 4—Cu A—40-g samples, tubes as received, vibrator and hammer, air velocity partly corrected [a]											
0 to 10	8	4½	2.7	16.5	2.7	5.55	+0.1−0.4	0.16	0	2.3	97.7
10 to 20	8	2¼	10.7	16.5	10.7	18.06	+.6−0.9	.38	0	1.8	98.2
20 to 30	8	1½	24.1	16.5	24.1	26.18	+1.1−0.5	.53	0.3	11.3	88.4
30 to 40	8	1¼	42.9	16.5	34.7	18.30	+1.4−1.8	1.18	.9	10.9	88.2
+40	8	.....	.....	.....	.....	31.78	+1.4−1.8	1.02	0	0	100
Recovery	8	.....	.....	.....	.....	99.71	+0.3−0.5	0.24	.....	.....	.....
Series 5—Cu A—40-g samples, small tubes lapped, vibrator and hammer, air velocity corrected ($V=K''d^{1.4}$ above 20 microns)											
0 to 10	2	4½	2.7	16.5	2.7	5.2	+0.1−0.1	.....	0	1.3	98.7
10 to 20	2	2¼	10.7	16.5	10.7	17.0	+.1−0.2	.....	0.1	1.8	98.1
20 to 30	2	1½	24.1	13.1	19.1	14.5	+.4−0.4	.....	.1	3.2	96.8
30 to 40	2	1¼	42.9	13.6	28.6	13.4	+.6−0.7	.....	.8	1.9	97.3
+40	2	.....	.....	.....	.....	50.0	+.3−0.4	.....	2.2	0	97.8
Recovery	2	.....	.....	.....	.....	99.9	+.1−0.1	.....	.....	.....	.....

[a] Air flow corresponding to Stokes air velocity used in all tubes except 1¼ in., for which the air flow was calculated for 1⅛ in. diameter.

TABLE 4. *Roller analyses of hydrogen reduced iron powders,* Fe B1 *and* Fe B2, *40-g samples, minus No. 325 sieve 30-min intervals, 10-percent end point, dry air*

Fraction (microns)	Number of tests	Diameter of settling tube	Stokes air velocity	Air flow	Average Air velocity	Roller analysis—percentage by weight of original sample		
						Mean	Maximum deviation from mean	Standard deviation
Series 1—Fe B1—Tubes as received, hammer only, air flow partly corrected [a]								
		Inches	*cm/sec*	*L/min*	*cm/sec*			
0 to 5	23	9	0.6	14.5	0.6	1.67	+0.4−0.7	0.28
5 to 10	23	4½	2.4	14.5	2.4	1.04	+.6−0.5	.32
10 to 20	23	2¼	9.4	14.5	9.4	14.69	+.8−1.0	.57
20 to 40	23	1¼	37.6	14.5	30.5	63.92	+5.1−5.2	2.90
+40	23	.....	.....	.....	.....	15.70	+5.7−4.5	2.84
Recovery	23	.....	.....	.....	.....	97.62	+1.8−6.0	1.67
Series 2—Fe B2—Small tubes lapped, vibrator and hammer, air flow partly corrected [a]								
0 to 10	[b] 11	4½	2.4	14.5	0.6	4.47	+0.3−0.3	0.15
10 to 20	[b] 11	2¼	9.4	14.5	2.4	17.74	+.4−0.3	.27
20 to 30	6	1½	21.2	14.5	21.2	36.45	+.7−1.8	.86
30 to 40	6	1¼	37.6	14.5	30.5	33.70	+1.1−1.3	.83
+40	6	.....	.....	.....	.....	7.50	+0.9−1.1	.80
Recovery	6	.....	.....	.....	.....	99.76	+.1−0.3	.15
Series 3—Fe B2—Small tubes lapped, vibrator and hammer, air flow corrected ($V=K''d^{1.4}$ above 20 microns)								
20 to 30	5	1½	21.2	11.8	17.2	26.00	+1.0−0.8	0.75
30 to 40	5	1¼	37.6	12.2	25.8	32.38	+0.8−1.1	.74
+40	5	.....	.....	.....	.....	18.70	+.9−1.4	.86
Recovery	5	.....	.....	.....	.....	99.46	+.3−0.6	.31

[a] Air flow corresponding to Stokes air velocity used in all tubes except 1¼ in., for which the air flow was calculated for 1⅛-in. diameter.
[b] These tests include the 0- to 10- and 10- to 20-micron fractions of series 2 and 3.

TABLE 5. *Roller analyses of electrolytic iron powder,* Fe A, *40-g samples, minus No. 325 sieve, 30-min intervals, 10-percent end point, dry air*

Fraction (microns)	Number of tests	Diameter of settling tube	Stokes air velocity	Air flow	Average Air velocity	Roller analysis—percentage by weight of original fraction		
						Mean	Maximum deviation from mean	Standard deviation
Series 1—Tubes as received, hammer only, air flow partly corrected [a]								
		Inches	*cm/sec*	*L/min*	*cm/sec*			
0 to 5	12	9	0.6	14.5	0.6	1.66	+0.2−0.3	0.14
5 to 10	12	4½	2.4	14.5	2.4	5.77	+.4−0.5	.31
10 to 20	12	2¼	9.4	14.5	9.4	23.73	+.8−0.4	.44
20 to 40	12	1¼	37.6	14.5	30.5	61.89	+1.3−0.7	.59
+40	12	.....	.....	.....	.....	5.58	+1.1−1.6	.72
Recovery	12	.....	.....	.....	.....	98.48	+0.8−1.2	.63
Series 2—Small tubes lapped, hammer and vibrator, air flow partly corrected [a]								
0 to 10	[b] 11	4½	2.4	14.5	2.4	6.30	+0.2−0.4	0.18
10 to 20	[b] 11	2¼	9.4	14.5	9.4	23.18	+1.1−1.4	.86
20 to 30	5	1½	21.2	14.5	21.2	38.36	+1.0−0.8	.82
30 to 40	5	1¼	37.6	14.5	30.5	24.06	+1.3−0.8	.93
+40	5	.....	.....	.....	.....	6.78	+0.7−0.7	.58
Recovery	5	.....	.....	.....	.....	99.54	+.3−0.2	.16
Series 3—Small tubes lapped, hammer and vibrator, air flow corrected ($V=K''d^{1.4}$ above 20 microns)								
20 to 30	6	1½	21.2	11.8	17.2	25.37	+0.5−0.7	0.45
30 to 40	6	1¼	37.6	12.2	25.8	23.97	+.9−1.2	.88
+40	6	.....	.....	.....	.....	21.60	+.6−1.5	.75
Recovery	6	.....	.....	.....	.....	99.82	+.2−0.4	.17

[a] Air flow corresponding to Stokes air velocity used in all tubes except 1¼ in., for which the air flow was calculated for 1⅛-in. diameter.
[b] These tests include the 0- to 10- and 10- to 20-micron fractions of series 2 and 3.

TABLE 6. *Roller analyses of carbonyl iron,* Fe C, *and electrolytic copper,* Cu C, *powders, minus No. 325 sieve, 30-min intervals' 10-percent end point, dry air*

Fraction (microns)	Number of tests	Diameter of settling tube	Stokes air velocity	Air flow	Average air velocity	Roller analysis—percentage by weight of original sample		
						Mean	Maximum deviation from mean	Standard deviation
Series 1—Fe C, 30-g samples, tubes as received, hammer only								
		Inches	*cm/sec*	*L/min*	*cm/sec*			
0 to 5	14	9	0.6	14.5	0.6	27.73	+3.3−2.8	1.95
5 to 10	14	4½	2.4	14.5	2.4	53.07	+2.7−2.5	1.98
10 to 20	14	2¼	9.4	14.5	9.4	15.87	+2.8−1.9	1.51
+20	14	.....	.....	.....	.....	0.92	+1.3−0.4	0.46
Recovery	14	.....	.....	.....	.....	97.61	+1.8−3.7	1.70
Series 2—Fe C, 30-g samples, tubes as received, vibrator and hammer								
0 to 5	6	9	0.6	14.5	0.6	32.97	+1.2−0.8	0.70
5 to 10	6	3½	2.4	14.5	2.4	50.83	+1.2−1.0	.91
10 to 20	6	2¼	9.4	14.5	9.4	15.12	+0.8−0.3	.40
+20	6	.....	.....	.....	.....	0.73	+.2−0.2	.15
Recovery	6	.....	.....	.....	.....	99.62	+.4−0.4	.31
Series 3—Fe C, 30-g samples, tubes as received, vibrator and hammer								
0 to 10	4	4½	2.4	14.5	2.4	79.90	+0.4−0.9	0.53
10 to 20	4	2¼	9.4	14.5	9.4	18.62	+.9−0.4	.52
+20	4	.....	.....	.....	.....	0.82	+.1−0.1	.08
Recovery	4	.....	.....	.....	.....	99.35	+0 −0.1	.05
Series 4—Cu C, 15-g samples, tubes as received, vibrator and hammer								
0 to 5	5	9	0.67	16.5	0.67	20.08	+0.6−0.6	0.42
5 to 10	5	4½	2.7	16.5	2.7	38.91	+.9−0.8	.59
10 to 20	5	2¼	10.7	16.5	10.7	33.18	+.7−0.7	.50
+20	5	.....	.....	.....	.....	5.68	+.3−0.3	.19
Recovery	5	.....	.....	.....	.....	97.84	+.5−0.3	.28

TABLE 7. *Roller analyses of permalloy, PF, and atomized zinc,* Zn, *powders, 40-g samples, minus No. 325 sieve, 30-min intervals, 10-percent end point, dry air*

Fraction (microns)	Number of tests	Diameter of settling tube	Stokes air velocity	Air flow	Average air velocity	Roller analysis—percentage by weight of original samples			Typical microscopic count—percentage by weight of fraction		
						Mean	Maximum deviation from mean	Standard deviation	Undersize	Oversize	Within size limits
Series 1—PF powder, tubes as received, vibrator and hammer											
		Inches	*cm/sec*	*L/min*	*cm/sec*						
0 to 5	5	9	0.65	16.0	0.65	40.40	+1.0−1.0	0.93	.....	.....	.....
5 to 10	5	4½	2.6	16.0	2.6	40.94	+1.2−1.1	.93	.....	.....	.....
10 to 20	5	2¼	10.4	16.0	10.4	16.54	+0.4−0.5	.37	.....	.....	.....
+20	5	.....	.....	.....	.....	0.78	+.2−0.2	.13	.....	.....	.....
Recovery	5	.....	.....	.....	.....	98.52	+.2−0.4	.24	.....	.....	.....
Series 2—Zn powder, small tubes lapped, vibrator and hammer, air velocity partly corrected[a]											
0 to 5	[b] 10	9	0.53	13.1	0.53	22.77	+0.3−0.5	0.31	0	0	100
5 to 10	[b] 10	4½	2.1	13.1	2.1	34.06	+1.0−1.1	.74	0.2	0.2	99.6
10 to 20	[b] 10	2¼	8.5	13.1	8.5	25.09	+0.6−0.8	.47	.5	.4	99.1
20 to 40	5	1¼	34.1	13.1	27.6	15.50	+.3−0.2	.17	.3	7.2	92.5
+40	5	.....	.....	.....	.....	1.56	+.1−0.1	.08	.8	0	99.2
Recovery	5	.....	.....	.....	.....	98.88	+.7−0.7	.50	.....	.....	.....
Series 3—Zn powder, small tubes lapped, vibrator and hammer, air velocity corrected ($V = K''d^{1.4}$ above 20 microns)											
20 to 30	5	1½	19.2	10.9	15.9	8.74	+0.3−0.3	0.21	0.4	1.7	97.9
30 to 40	5	1¼	34.1	11.3	23.8	4.20	+.7−0.5	.42	1.4	0.6	98.0
+40	5	.....	.....	.....	.....	3.62	+.4−0.4	.35	2.0	0	98.0
Recovery	5	.....	.....	.....	.....	98.58	+.3−0.3	.23	.....	.....	.....

[a] Air flow coresponding to Stokes air velocity used in all tubes except 1¼ in. for which the air flow was calculated for 1¼ inch diameter.
[b] These 10 tests include the 0- to 5-, 5- to 10-, and 10- to 20- micron fractions of series 2 and 3.

TABLE 8. *Roller analyses of unsieved permalloy, PC, and atomized copper, Cu A, powders, with air velocity corrected ($V = K''d^2$ above 20 microns), 10-percent end point, vibrator and hammer, small tubes lapped, dry air*

Fraction (microns)	Number of tests	Diameter of settling tube	Stokes air velocity	Air flow	Average air velocity	Roller analysis—percentage by weight of original samples			Typical microscopic count—percentage by weight of fraction		
						Mean	Maximum deviation from mean	Standard deviation	Undersize	Oversize	Within size limits
Series 1—PC powder, unsieved, 40-g samples											
		Inches	*cm/sec*	*L/min*	*cm/sec*						
0 to 10	5	4½	2.6	16.0	2.6	0.56	+0.1−0.1	0.08	0	0	100
10 to 20	5	2¼	10.4	16.0	10.4	52.60	+ .4−0.4	.28	0	1.3	98.7
20 to 30	5	1½	23.4	12.9	18.7	32.60	+ .3−0.6	.35	0.1	1.5	98.4
30 to 40	5	1¼	41.6	13.3	27.9	9.74	+ .8−0.5	.49	.7	0.2	99.1
+40	5	.....	.....	.....	.....	3.96	+ .1−0.2	.10	.9	0	99.1
Recovery	5	.....	.....	.....	.....	99.46	+ .2−0.6	.29	.....	.....	.....
Series 2—PC powder, unsieved, 100-g samples											
0 to 20	5	2¼	10.4	16.0	10.4	50.00	+0.8−0.6	0.59	0	0	100
+20	5	.....	.....	.....	.....	49.78	+ .7−0.8	.58	1.4	0	98.6
Recovery	5	.....	.....	.....	.....	99.78	+ .1−0.2	.10	.....	.....	.....
Series 3—PC powder, accumulated +20 fractions, 40-g samples											
0 to 30	1	1¼	23.4	12.9	18.7	67.0	.....	.....	0	0.4	99.6
30 to 40	1	1¼	41.6	13.3	27.9	25.6	.....	.....	3.3	.7	96.0
40 to 50	1	1¼	65.0	18.2	38.2	5.3	.....	.....	0.7	1.7	97.6
50 to 60	1	1¼	93.6	23.4	49.3	1.3	.....	.....	.8	0.5	98.7
60 to 70	1	1¼	127.4	29.1	61.2	0.4	.....	.....	2.5	2.9	94.6
+70	1	.....	.....	.....	.....	.2	.....	.....	3.2	0	96.5
Recovery	1	.....	.....	.....	.....	99.8	.....	.....	.....	.....	.....
Series 4—Cu A powder, unsieved, 40-g samples											
0 to 30	5	1½	24.1	13.1	19.4	21.62	+1.1−0.8	0.75	0	0.3	99.7
30 to 40	5	1¼	42.9	13.6	28.6	10.98	+0.5−1.0	.54	0.1	2.7	97.2
40 to 50	5	1¼	67.0	18.6	39.1	11.02	+1.3−0.9	.76	.9	2.3	96.8
50 to 60	5	1¼	96.5	24.0	50.5	9.66	+0.5−0.4	.38	3.2	2.1	94.7
60 to 70	5	1¼	131.3	29.7	62.6	11.80	+ .5−0.9	.48	3.1	2.1	94.8
70 to 80	5	1¼	171.5	35.9	75.5	7.02	+ .4−0.4	.34	2.7	12.5	84.8
80 to 90	5	1¼	217.1	42.3	89.1	6.76	+ .4−0.5	.32	4.0	14.8	81.2
90 to 100	5	1¼	268.0	49.0	103.2	5.70	+ .3−0.4	.28	9.6	14.3	76.1
100 to 110	5	1¼	324.3	56.0	117.9	4.92	+ .7−0.4	.39	7.1	16.9	76.0
110 to 120	5	1¼	385.9	63.2	133.0	4.18	+ .6−0.8	.57	11.5	22.1	66.4
+120	5	.....	.....	.....	.....	5.14	+ .4−0.5	.32	12.1	0	87.9
Recovery	5	.....	.....	.....	.....	99.10	+ .3−0.4	.28	.....	.....	.....

TABLE 9. *Roller analyses of accumulated Roller fractions of permalloy mix, PM, powder, with air velocity corrected ($V = K''d^{1.4}$ above 20 microns) 10-percent end point, vibrator and hammer, small tubes lapped, dry air*

Fraction (microns)	Number of tests	Diameter of settling tube	Stokes air velocity	Air flow	Average air velocity	Roller analysis—percentage by weight of original sample	
						Mean	Maximum deviation from mean
Series 1—Accumulated 0 to 10 fraction, 40-g samples							
		Inches	*cm/sec*	*L/min*	*cm/sec*		
0 to 10	2	4½	2.6	16.0	2.6	81.6	+0.5 −0.6
10 to 20	2	2¾	10.4	16.0	10.4	15.8	+.1 −0
20 to 30	2	1½	23.4	12.9	18.7	1.0	+.1 −0.2
30 to 40	2	1¼	41.6	13.3	27.9	0.2	+0 −0.1
+40	2	.....	.....	.....	.....	0.1	+0 −0
Recovery	2	.....	.....	.....	.....	98.6	+0.6 −0.7
Series 2—Accumulated 10-20 fraction, 40-g samples							
0 to 10	2	4½	2.6	16.0	2.6	1.6	+0.4 −0.5
10 to 20	2	2¾	10.4	16.0	10.4	96.3	+.1 −0.1
20 to 30	2	1½	23.4	12.9	18.7	1.0	+.4 −0.5
30 to 40	2	1¼	41.6	13.3	27.9	0.4	+.3 −0.2
+40	2	.....	.....	.....	.....	0.1	+.1 −0.1
Recovery	2	.....	.....	.....	.....	99.3	+.6 −0.6
Series 3—Accumulated 20 to 30 fraction, 25-g sample							
0 to 10	1	4½	2.6	16.0	2.6	0	.....
10 to 20	1	2¾	10.4	16.0	10.4	17.6	.....
20 to 30	1	1½	23.4	12.9	18.7	76.7	.....
30 to 40	1	1¼	41.6	13.3	27.9	5.1	.....
+40	1	.....	.....	.....	.....	0.1	.....
Recovery	1	.....	.....	.....	.....	99.5	.....
Series 4—Accumulated 30 to 40 fraction, 8-g sample							
0 to 10	1	4½	2.6	16.0	2.6	0.3	.....
10 to 20	1	2¾	10.4	16.0	10.4	0.4	.....
20 to 30	1	1½	23.4	12.9	18.7	17.9	.....
30 to 40	1	1¼	41.6	13.3	27.9	76.1	.....
+40	1	.....	.....	.....	.....	5.4	.....
Recovery	1	.....	.....	.....	.....	100.1	.....
Series 5—Accumulated +40 fraction, 2.82-g sample							
0 to 10	1	4½	2.6	16.0	2.6	0.4	.....
10 to 20	1	2¾	10.4	16.0	10.4	0.4	.....
20 to 30	1	1½	23.4	12.9	18.7	0.4	.....
30 to 40	1	1¼	41.6	13.3	27.9	20.2	.....
+40	1	.....	.....	.....	.....	79.1	.....
Recovery	1	.....	.....	.....	.....	100.5	.....

4.2. Condition of Interior Surface of Settling Tube

The tabulated results show that for diameters up to 20 microns, good reproducibility (on the order of ±1 percent of the original weight of the sample) was obtained with powders such as Cu A, Cu B, Fe A, Fe B1, and Fe B2, which contained relatively small amounts (5 percent or less) of the 0- to 5-micron fraction (tables 3, 4, 5). Good results were also obtained with the PM powder (0- to 5-micron fraction, theoretically, about 13.5 percent) without the use of a vibrator if the initial separation was made at 10 microns (series 3, table 2). However, for separations made at 30 or 40 microns in the 1½- and 1¼-in. settling tubes as received, the results often varied widely. These variations were attributed to the rough condition of the interior surface of some of these tubes. The 9-, 4½-, and 2¼-in. tubes were made of welded stainless steel sheet, and the interior surfaces were smooth. The original 1¼-in. tubes supplied with the unit were made of brass tubing and failed after relatively short periods of service. One of these tubes was used only in series 1 of table 4, and gave reproducible results; another was used only for series 1 of table 5 and gave variable results. Whether or not these inconsistencies were due to the condition of the interior surfaces of these tubes cannot be stated, because they were not examined upon removal prior to returning them for replacement.

In all the other tabulated series of tests requiring the use of small tubes, 1¼- or 1½-in. diameter, austenitic stainless steel tubes were employed. Both of these tubes were made of stainless-steel tubing, machined to the required inside diameter, and the interior surfaces were relatively rough. Powder particles adhering to these rough surfaces were difficult to dislodge, and substantial amounts of undersized material were often carried over into the next fraction. In series 3 of table 2, for example, microscopic measurements of the 30- to 40-micron fraction showed the presence of 24.8 percent of undersize material, which had obviously remained as a residue from the prior 30 micron separation. Such condition caused wide variations in the results obtained for both the 20- to 30- and 30- to 40-micron fractions. The carryover of undersized material was considerably reduced with consequent improvement in reproducibility when a vibrator was used in addition to the regular hammer (series 4, table 2). Still further improvement in this respect was observed when the 30-micron separation was made in the smooth 2¼-in. tube (series 5, table 2), or when the interior surfaces of the smaller tubes were lapped (series 6, table 2). The amount of oversized material was reduced materially only by lowering the air velocity (series 7, table 2). Reproducible results were obtained with all other powders tested with these tubes when the interior surfaces were lapped (tables 3, 4, 5, 7, and 8).

4.3. Dislodgment of Small Particles

Efficient separations at the 5-micron level of powders such as PF, PM, Fe C, Cu C, and Zn, which contain substantial amounts (13.5 to 40.4 percent) of 0- to 5-micron fraction, were found to be difficult because of the tendency of particles to adhere to the walls of the settling tube. In such cases the hammer device alone was not sufficiently effective in dislodging the particles, consequently the results were variable and the total recovery was low (series 1, tables 2 and 6). But when a vibrator was used in addition to the regular hammer device, variations in results were diminished and the total recovery was markedly improved (tables 2, 6, and 7).

4.4. Size Range of Fraction

It will be noted from the tables that a separation at a larger particle diameter usually gave somewhat lower results than the accumulated weights of the finer fractions. In series 2 of tables 2 and 3, for example, the average for the 0- to 20-micron fractions of PM and Cu B powders was 68.9 and 49.6 percent, respectively, whereas the sums of the finer fractions (0- to 10- and 10- to 20-micron in series 3, table 2, and 0 to 5, 5 to 10, and 10 to 20 in series 1, table 3) were 70.8 and 53.4, respectively. This is believed to be a consequence of the uncertainty of the end point under some conditions. For the 0- to 20-micron fractions, the rate of separation for the initial 30-min intervals was very high (as much as 60 percent by weight of sample). However, this rate fell off rapidly, and at the 10-percent end point as much as 4 or 5 percent was still being blown over per interval. This clearly indicates that some of the border-line particles were not being separated.

Similar end-point uncertainty was found when accumulated, sized, fractions were analyzed by the Roller apparatus, as shown in table 9. The samples in these tests were the accumulated fractions of the 5 tests included in series 7 of table 2. These fractions contain many border-line particles that may be blown over or remain in the settling tubes, depending on the number of such particles present and the rate of separation. A sample of accumulated 20- to 30-micron fractions, for example, may contain some 18 and 19 microns as well as 31, 32, and possibly a few 33-micron particles. If a separation is made at 20 microns, the initial rate of separation will be low but will fall off slowly, so that by the time the end point is reached all of the undersize, most of the 20-micron, and many 21- and 22-micron particles will have been blown over. This may result in the separation of a nominal minus 20-micron fraction of appreciable size, even though repeated microscopic measurements have indicated that 98 to 99 percent by weight of the original sample was within the 20- to 30-micron size limits. When the separation is made at 30 microns, however, the initial rate of separation will be very high and will fall off rapidly, so that some of the border-line particles will remain in the tube to be blown over during the 40-micron separation.

4.5. Size of Samples

The size of sample, within the relatively small limits imposed by the diameter of the sample tube (M, fig. 1), appeared to have little effect on Roller particle-size analyses. This has been indicated previously by the inclusion of tests (3 for each weight) of samples, weighing 20, 30, 40, 60, 80, and 100 g, in the results represented by figure 6. It was noted, however, that the results for the 80- and 100-g samples were near the lower limit of the range, and large numbers of such tests might broaden the range. On the other hand, with very small samples, particularly of fine powders, the small losses of material unavoidably obtained become increasingly important on a percentage basis (see total recovery values of tables 2, 6, 7, and 8). In this investigation, consistent results were obtained by following the suggestion of the Metal Disintegrating Co. [9] in using samples weighing about 10 times the numerical value of the apparent density of the powder, with a maximum of 40 g in most cases.

4.6. Humidity of Air

The tendency of small particles to stick to each other or to the walls of the settling tubes was found to be markedly affected, in some cases, by the humidity of the air supplied to the settling tubes. The solid curves, E, A, and B shown in figure 8 represent the range of results obtained during the separation of the 0- to 10- or 0- to 5-micron fractions of the PM, Fe C, and Cu B powders with dried air and with hammer only. The broken curves E′, A′, and B′ represent the results obtained with humidified air and with hammer only. The air was humidified by passing it, in two stages, through alundum thimbles immersed in large bottles of water. The relative humidity, as measured by wet- and dry-bulb thermometry, was about 90 percent.

Curves E and E′ of figure 8 show that high humidity greatly increased the separation rate of the 0- to 10-micron fraction of the PM powder. The final results, however, were within the range of those obtained with dried air. The effect of humidity on the initial rate of separation of the 0- to 5-micron fraction of the Cu B was negligible, but the final results were considerably higher than those obtained with dried air (curves B and B′). Humidity had little effect on carbonyl iron powder, the results at all stages being within the range of those obtained with dried air (curves A and A′). With this powder, and with Cu C powder, more efficient dislodgment of particles was obtained by the use of a vibrator in addition to the hammer as shown by curves C and D (see also tables 2, 6, 7, and 8).

It is probable that the varying effect of high humidity may be connected with the static charges picked up by the particles during separation. These charges may vary in nature and magnitude with the humidity of the air, as well as with the size and composition of the particle.

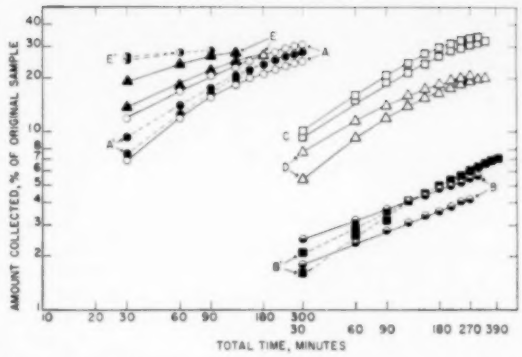

FIGURE 8. *Effect of the humidity of the air stream on the separation of fine fractions of metal powders.*

Curve E, 0- to 10-micron fraction of permalloy-mix powder obtained with dried air without vibrator; E′, same conditions except for relative humidity of the air—about 90 percent; A, 0- to 5-micron fraction of carbonyl iron, Fe C, powder obtained with dried air without vibrator; A′, same except for relative humidity of the air—about 90 percent; B, 0- to 5-micron fraction of electrolytic copper, Cu B, powder obtained with dried air without vibrator; B′, same except for relative humidity of the air—about 90 percent; C, 0- to 5-micron fraction of carbonyl iron, Fe C, powder obtained with dry air and with vibrator and hammer; D, 0- to 5-micron fraction of electrolytic copper, Cu C, powder obtained with dry air and with a vibrator in addition to the regular hammer.

4.7. Particle Shape

With the metal powders used in these experiments, particle shape was found to have no effect on the Roller analyses insofar as reproducibility was concerned. With the modifications in equipment previously discussed, and with reasonably uniform operating conditions, reproducible results were obtained with all powders tested at air velocities calculated for diameters of 5 to 40 microns. However, the accuracy of these separations, or rather the accuracy of the values assigned to the size limits of the fractions, depends on the relation that is assumed to exist between the diameter of the particle and its falling velocity. The accuracy of some of these assumptions will be discussed in the next section.

5. Accuracy of Separations

The accuracy of Roller analyses was checked by microscopic measurements on sized fractions of permalloy, atomized copper, and atomized zinc powders. Samples of these powders, dispersed in xylene containing a few drops of cedar oil on plain glass slides, were mounted on a microscope; the images were projected with transmitted light upon a screen at 1,000 magnifications; and measured to the nearest millimeter. While it is recognized that there are inherent errors in this method of measurement, they are minute with respect to the present application of the method and, therefore, may be overlooked.

Microscopic measurements indicated that separations of these nearly spherical particles closely approximated the requirements of Stokes law for diameters of 5 to 20 microns. The parabolic curve A

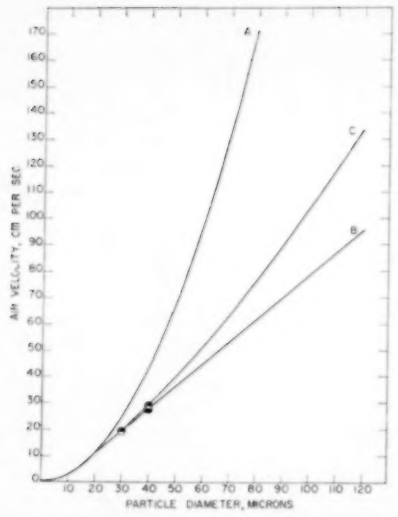

FIGURE 9. *Curves showing theoretical relationships between air velocity and diameter of particle.*

Curve A, $V=Kd^2$; B, $V=C+K'd$; C, $V=K''d^{1.4}$. Symbols ◓ and ● represent experimentally determined values.

of figure 9, for example, shows the theoretical values for the terminal falling velocities of spherical PM particles, as calculated by Stokes law, plotted against the particle diameter in microns. In actual separations at air velocities taken from this curve, it was found that a minimum of 98.5 percent by weight of the 0- to 10- and 10- to 20-micron fractions were within the designated size limits, as shown by the microscopic counts of series 3 of table 2. Similar results were obtained with 0- to 5-, 0- to 10-, 0- to 20-, 5- to 10-, and 10- to 20-micron fractions of Cu A, PF, Zn, and PC powders, as shown in tables 3, 7, and 8.

For separations at larger diameters, air velocities calculated by Stokes law were too high. For example, the air velocities required for separations of PM powder at 30 and 40 microns would be 23.4 and 41.6 cm/sec, respectively (see curve A, fig. 9). It was found, mostly by trial and error, that accurate separations of this powder could be obtained with air velocities of 18.7 cm/sec for 30 microns, and either 27 or 28 cm/sec for 40 microns.

Dallevalle [12], citing the work of Allen [13] and Martin [14], states that, between the region of streamline motion, where V varies as the square of the particle diameter, and the region of fully turbulent motion, where V varies as the square root of the particle diameter, there is a rather extensive region where a straight line relationship exists and V varies as the first power of the particle diameter.

Curve B of figure 9 is a straight line through the points 18.7 and 27 determined experimentally as suitable for accurate separations at 30 and 40 microns respectively. This line cuts the parabola of Stokes law at about 20 microns. Tests were made of PC powder, using air velocities taken from curve B for separations at diameters ranging by 10-μ increments from 40 to 90 microns (40, 50, 60, etc.). These velocities were found to be too low for accurate separations. The nominal 70- to 80-micron fraction, for example, when measured microscopically actually was 100 percent within the 60- to 70-micron range. Microscopic counts were made of each of the fractions to determine approximately the actual separation points. These points, when plotted on logarithmic coordinates against the air velocities used, fell near a straight line with a slope of approximately 1.4.

This suggests a relationship similar to that used by Burke and Plummer [15], who related their own and other available data to the general formula for the resistance to motion, R, of a particle in a fluid $R=k\rho_0^{n-1}\mu^{2-n}(d/2)^n V^n$. The force causing motion is for a sphere, $F=(\pi d^3/6)\ (\rho-\rho_0)g$. At terminal velocity $R=F$ and

$$V^n=\frac{(2)^n\pi g}{6k}\,(\rho-\rho_0)\,\rho_0^{1-n}\mu^{n-2}d^{3-n}. \qquad (2)$$

When $n=1$, this equation becomes Stokes law for streamline motion, and when $n=2$, it becomes Newton's law for turbulent motion.

Burke and Plummer suggest that in the intermediate region $1<n<2$, and probably changes smoothly and continuously between the two limiting values.

If n is made equal to 1.25, eq (2) becomes

$$V=2\left[\frac{\pi g(\rho-\rho_0)}{6k}\right]^{0.8}\rho_0^{-0.2}\mu^{-0.6}d^{1.4}. \qquad (3)$$

With $k=16.07$, this gives for permalloy powder $V=18.7$ at 30 microns and $V=27.9$ at 40 microns. A theoretical curve for PM powder with air velocities calculated by this formula is shown as curve C in figure 9.

Tests were made on unsieved PC and Cu A powders with air velocities calculated by eq (3) for particle diameters larger than 20 microns. The results shown in table 8 were comparable to microscopic measurements for particle diameters up to 70 microns, a minimum of 94.6 percent by weight of the 60- to 70-micron fraction being within the specified size limits. These results indicate that, for particles larger than those which obey Stokes law, the exponent n of eq (2) changes very rapidly from a value of 1 at 20 microns to about 1.25 at 30 microns. Between 30 and 70 microns the change in n, if any, is too small to be detected by this method of testing. Above 70 microns the separations became progressively less sharp. There appeared to be some preponderance of oversized material in the larger fractions that may indicate that n changes in this region to a value larger than 1.25. However, an increasing overlapping of size range among consecutive fractions (both undersize and oversize) made it impossible to draw definite conclusions. In spite of this overlapping, the results continued to be reproducible up to 120 microns, as may be seen in series 4 of table 8.

As previously stated, no attempt was made to check the Roller analyses of powders composed of irregularly shaped particles by microscopic measurements. Some work has been done in this field, but at the present time, the exact nature of the dimensions that control the measurement of an irregularly shaped particle by air elutriation is not well understood nor is the possible relationship of these dimensions to any visible dimensions or to the surface area or volume of the particle.

6. Summary

Subsieve particle size analyses of a number of metal powders were made with a Roller air analyzer, using 30-min. intervals and a 10-percent end-point criterion. This procedure was found to be satisfactory for samples of normal size distribution. The end point was somewhat uncertain, however, when (1) the initial rates were very low but persistent, as in a separation near the lower limit of an accululated, sized fraction, and (2) the initial rates were very high but fell off rapidly, as in a separation near the upper limit of an accumulated sized fraction, or with a relatively large range of sizes within the fraction such as 0 to 30 microns.

Particle shape appeared to have no effect on the reproducibility of the tests. Results reproducible within approximately ± 1 percent by weight of sample were obtained with very irregularly shaped particles for diameters up to 40 microns, and with spherical particles for diameters up to 120 microns provided the following conditions were fulfilled:

1. An alundum extraction thimble was used to collect the fractions.

2. The inside surfaces of the settling tubes were smooth.

3. A Syntron vibrator was used in addition to the regular hammer, particularly for powders containing relatively large amounts of the 0- to 5-micron fraction.

4. The size of the sample, while not cirtical, was maintained at approximately 10 times the apparent density as a lower limit, with 40 g as a maximum in most cases.

The effect of high humidity on the separation of metal powders was not consistent. With some powders the rate of separation was markedly increased, but with others no effect was noted. In view of this uncertainty, it would seem advisable to use dried air or air of relatively constant humidity for all tests.

The accuracy of analyses of spherical powders was checked by microscopic measurements of the fractions. With these powders Stokes law applied for diameters of 5 to 20 microns, and the air velocity could be calculated accurately as proportional to the square of the particle diameter ($V=Kd^2$). For larger diameters, the air velocity was found to be proportional to the 1.4 power of the diameter ($V=K''d^{1.4}$). At still larger diameters, increased overlapping of size range among consecutive fractions prevented any definite conclusions, except that the results continued to be reproducible.

Grateful acknowledgment is made to W. Earl Lindlief, formerly of the National Bureau of Standards, who assisted in the planning and supervision of the early part of the investigation; and to John C. Everts and Caroline Plummer Jeffries for their patient and efficient assistance in the monotonous and time-consuming tasks of making the vitally important particle-size counts and analyses.

7. References

[1] P. S. Roller, Separation and size distribution of microscopic particles—an air analyzer for fine powders, U. S. Bureau of Mines Tech. Pap. No. 490 (1931).
[2] P. S. Roller, U. S. Patent 2019507 (1935).
[3] P. S. Roller, Measurement of particle size with an accurate air analyzer, ASTM Proc. **32** (II) 607 (1932).
[4] P. S. Roller, Size distribution of ceramic powders as determined by a particle size analyzer, J. Am. Ceram. Soc. **20,** 167 (1951).
[5] MPA Standard 12–51T, Subsieve analysis of granular metal powders by air classification (1951).
[6] ASTM Tentative method for sub-sieve analysis of granular metal powders by air classification (under consideration) (1952).
[7] R. A. Castleman, Resistance to the steady motion of small spheres in fluids, NACA Technical Note 231 (1926).
[8] H. Wadell, New sedimentation formulas, Physics **5,** 281 (1934).
[9] Metals Disentegrating Co., Elizabeth, N. J., Particle size analysis of metal powders (1946).
[10] P. S. Roller and P. V. Roundy, Surface area of portland cement, ASTM symposium on particle size measurement (1941).
[11] P. S. Roller, Metal powder size determination by Roller air analyzer, ASTM symposium on powder metallurgy (1952).
[12] J. M. Dallevalle, Micromeritics (Pitman Publishing Corp., New York, N. Y., 1943).
[13] H. S. Allen, The motion of spheres in a viscous fluid, Phil. Mag. [5] **50,** 323 (1900).
[14] G. Martin, On the diameters of irregularly shaped crushed sand particles lifted by air currents of different speeds and different temperatures, Trans. Brit. Ceram. Soc. **26,** 21 (1926).
[15] S. P. Burke and W. B. Plummer, Suspension of macroscopic particles in a turbulent gas stream, Ind. Eng. Chem. **20,** 1196 (1928).

Washington, December 12, 1952.

Journal of Research of the National Bureau of Standards Vol. 51, No. 1, July 1953 Research Paper 2429

Eigenvectors of Matric Polynomials [1]

Murray Mannos

It is the object of this paper to compare the eigenvectors of an arbitrary $n \times n$ matrix A over the complex field with those of the matric polynomial $f(A)$. While it is well known that each eigenvector of A is an eigenvector of $f(A)$, it is not, in general, true that A and $f(A)$ have identical eigenvectors. In this regard a necessary and sufficient condition that A and $f(A)$ have identical eigenvectors is given. The condition is that both (1) and (2) hold:

(1) $f'(\lambda) \neq 0$ for all eigenvalues λ of the matrix A corresponding to nonlinear elementary divisors.

(2) The values of $f(\mu)$ are distinct for all eigenvalues μ of the matrix A corresponding to linear elementary divisors.

When either (1) or (2) fails to hold, then $f(A)$ has eigenvectors that are not eigenvectors of A. This situation is also discussed.

The vector space of eigenvectors of the matrix A corresponding to the eigenvalue λ shall be denoted by $V_\lambda[A]$. The vector space spanned by the eigenvectors of A shall be denoted by $V[A]$. Further, $d\{V_\lambda[A]\}$ and $d\{V[A]\}$ shall denote their dimensions. It is clear that each eigenvector of A is an eigenvector of $f(A)$. That is, $V_\lambda[A] \subseteq V_{f(\lambda)}[f(A)]$ for each eigenvalue λ of A. Thus $V[A] \subseteq V[f(A)]$.

Let J be the Jordan canonical form of A. Then there exists a nonsingular matrix P such that $P^{-1}AP=J$ and so $P^{-1}f(A)P=f(J)$.

Lemma 1. *The eigenvectors of A and $f(A)$ are identical if, and only if, the eigenvectors of J and $f(J)$ are identical.*

Proof. This follows from the fact that $P\xi$ is an eigenvector of PBP^{-1} if ξ is an eigenvector of the matrix B.

Since $P\{V_\lambda[J]\}=V_\lambda[A]$, it follows that

$$d\{V[f(A)]\}-d\{V[A]\}=d\{V[f(J)]\}-d\{V[J]\},$$

where $P\{V_\lambda[J]\}$ denotes the space of all vectors $P\xi$, where ξ is an eigenvector of J corresponding to λ.

Lemma 2. *If $D=diag\ [\alpha,\alpha, \ldots,\alpha; \beta,\beta, \ldots,\beta; \ldots; \pi,\pi, \ldots,\pi]$, where $\alpha,\beta, \ldots,\pi$ are distinct, then $V[D]=V[f(D)]$. Furthermore, the eigenvectors of D are identical with those of $f(D)$ if, and only if, $f(\alpha), f(\beta), \ldots, f(\pi)$ are all distinct.*

Proof. If D is of order n, it is clear that both the eigenvectors of D and $f(D)$ each generate the whole n-dimensional vector space. If $f(\alpha)=f(\beta)$, then it is easily seen that $f(D)$ has eigenvectors corresponding to the eigenvalue $f(\alpha)=f(\beta)$, which are not eigenvectors of D.

Lemma 3. *If*

$$J_m(\lambda)=\begin{bmatrix} \lambda & 1 & 0 & \ldots & 0 & 0 & 0 \\ 0 & \lambda & 1 & \ldots & 0 & 0 & 0 \\ \cdot & \cdot & \cdot & & \cdot & \cdot & \cdot \\ \cdot & \cdot & \cdot & & \cdot & \cdot & \cdot \\ \cdot & \cdot & \cdot & & \cdot & \cdot & \cdot \\ 0 & 0 & 0 & \ldots & 0 & \lambda & 1 \\ 0 & 0 & 0 & \ldots & 0 & 0 & \lambda \end{bmatrix},$$

then

$$f(J_m(\lambda))=\begin{bmatrix} f(\lambda) & f'(\lambda) & \frac{f''(\lambda)}{2!} & \frac{f'''(\lambda)}{3!} & \ldots & \frac{f^{(m-1)}(\lambda)}{(m-1)!} \\ 0 & f(\lambda) & f'(\lambda) & \frac{f''(\lambda)}{2!} & \ldots & \frac{f^{(m-2)}(\lambda)}{(m-2)!} \\ 0 & 0 & f(\lambda) & f'(\lambda) & \ldots & \frac{f^{(m-3)}(\lambda)}{(m-3)!} \\ \cdot & \cdot & \cdot & \cdot & \cdot & \cdot \\ \cdot & \cdot & \cdot & \cdot & \cdot & \cdot \\ \cdot & \cdot & \cdot & \cdot & \cdot & \cdot \\ 0 & 0 & 0 & 0 & \ldots & f(\lambda) \ \ f'(\lambda) \\ 0 & 0 & 0 & 0 & \ldots & 0 \ \ f(\lambda) \end{bmatrix}.$$

Proofs of the lemma may be found in Wedderburn [2] and MacDuffee.[3]

Lemma 4. *If $f'(\lambda)=f''(\lambda)=\ldots=f^{(r)}(\lambda)=0$ and $f^{(r+1)}(\lambda)\neq 0$ $(r=1,2, \ldots,m-2)$, then*

$$d\{V_{f(\lambda)}[f(J_m(\lambda))]\}-d\{V_\lambda[J_m(\lambda)]\}=r,$$

and conversely. Also,

$$d\{V_{f(\lambda)}[f(J_m(\lambda))]\}-d\{V_\lambda[J_m(\lambda)]\}=m-1$$

if, and only if, $f'(\lambda)=f''(\lambda)=\ldots=f^{m-1}(\lambda)=0$.

Proof. If $f'(\lambda)=f''(\lambda)=\ldots=f^{(r)}(\lambda)=0$, but $f^{(r+1)}(\lambda)\neq 0$, it follows that the rank of the matrix $f(J_m(\lambda))-f(\lambda)I$ is $m-(r+1)$, as may be observed by noting the nonzero minor of order $m-(r+1)$ in the upper right-hand corner of the matrix. Thus the nullity of $f(J_m(\lambda))-f(\lambda)I$ is $r+1$. If the first $m-1$ derivatives of $f(x)$ vanish at $x=\lambda$, then the nullity of $f(J_m(\lambda))-f(\lambda)I$ is m. In a similar fashion one finds that the matrix $J_m(\lambda)-\lambda I$ has nullity equal to 1. This establishes the lemma.

Corollary. The matrices $J_m(\lambda)$ and $f(J_m(\lambda))$ have identical eigenvectors if, and only if, $f'(\lambda)\neq 0$.

It is to be noted that in this case $V_{f(\lambda)}[f(J_m(\lambda))]$

[1] Preparation of this paper was sponsored (in part) by the Office of Scientific Research, USAF.

[2] J. H. M. Wedderburn, Lectures on Matrices, (Am. Math. Soc., Colloquium Pub. vol. 17, New York, N. Y., 1934).

[3] C. C. MacDuffee, An Introduction to Abstract Algebra (John Wiley & Sons, New York, N. Y., 1940).

and $V_\lambda[J_m(\lambda)]$ are each spanned by the single column vector $[1,0,\ldots,0]^T$.

At this point it will be convenient to introduce the language of elementary divisors. Each block in the Jordan canonical form of a matrix A corresponds to an elementary divisor $(x-\lambda)^m$, and conversely. Each such block is called the hypercompanion matrix $J_m(\lambda)$ of the polynomial $(x-\lambda)^m$.

Suppose the nonlinear elementary divisors of the matrix A corresponding to the eigenvalue λ are of the form $(x-\lambda)^{m_\lambda^{(1)}}, (x-\lambda)^{m_\lambda^{(2)}}, \ldots, (x-\lambda)^{m_\lambda^{(k_\lambda)}}$, where $m_\lambda^{(i)}$ $(i=1,2,\ldots,k_\lambda)$ are integers such that $m_\lambda^{(1)}\geq m_\lambda^{(2)}\geq\ldots\geq m_\lambda^{(k_\lambda)}>1$. Furthermore, suppose that $(x-\lambda)^{m_\lambda^{(i)}}$ appears as an elementary divisor $n_\lambda^{(i)}$ times. Let $p_\lambda=\sum_{i=1}^{k_\lambda} n_\lambda^{(i)}$ denote the total number of nonlinear elementary divisors of A corresponding to the eigenvalue λ. Denote by n_λ the number of linear elementary divisors of A corresponding to the eigenvalue λ. Further, denote by K_λ the direct sum of the hypercompanion matrices of the elementary divisors corresponding to λ. Set

$$d_\lambda=d\{V_{f(\lambda)}[f(K_\lambda)]\}-d\{V_\lambda[K_\lambda]\}.$$

Lemma 5. If the first $m_\lambda^{(1)}-1$ derivatives of $f(x)$ vanish at $x=\lambda$, then $d_\lambda=\sum_{i=1}^{k_\lambda} n_\lambda^{(i)}(m_\lambda^{(i)}-1)$; whereas, if the first $r<m_\lambda^{(1)}-1$ derivatives of $f(x)$ vanish at $x=\lambda$, but $f^{(r+1)}(\lambda)\neq 0$, then $d_\lambda=\sum_{i=1}^{l-1} n_\lambda^{(i)} r+\sum_{i=l}^{k_\lambda} n_\lambda^{(i)}(m_\lambda^{(i)}-1)$, where $m_\lambda^{(l)}$ is the largest of the integers $m_\lambda^{(i)}$ $(i=1,2,\ldots,k_\lambda)$ such that $m_\lambda^{(i)}\leq r$.

Proof. This follows from lemma 4, the fact that the nullity of $K_\lambda-\lambda I$ is the sum of the nullities of the characteristic matrices of the hypercompanion matrices of the individual elementary divisors corresponding to the eigenvalue λ and a similar statement about the nullity of $f(K_\lambda)-f(\lambda)I$.

Corollary. The matrices K_λ and $f(K_\lambda)$ have identical eigenvectors if, and only if, $f'(\lambda)\neq 0$.

Proof. This follows from the fact that $d_\lambda=0$.

The Jordan canonical form $J=\operatorname{diag}[K_\alpha,K_\beta,\ldots,K_\pi]$ of A is a direct sum of matrices K_λ, where $\lambda=\alpha,\beta,\ldots$ runs through the distinct eigenvalues of A. The subsequent theorems of this paper involve the following main conditions:

Condition 1. $f'(\lambda)\neq 0$ for all eigenvalues λ of the matrix A corresponding to nonlinear elementary divisors.

Condition 2. The values $f(\mu)$ are distinct for all eigenvalues μ of the matrix A corresponding to linear elementary divisors.

The first theorem concerns the case where condition 1 does not hold, whether condition 2 holds or not.

Theorem 1. If condition 1 does not hold, then

$$d\{V[f(A)]\}-d\{V[A]\}=\sum_\lambda d_\lambda,$$

where λ varies through all distinct eigenvalues of A corresponding to nonlinear elementary divisors, and d_λ is computed as in lemma 5.

Proof. One notes first that

$$V[J]=V_\alpha[J]+V_\beta[J]+\ldots+V_\pi[J],$$

and

$$V[f(J)]=V_{f(\alpha)}[f(J)]+V_{f(\beta)}[f(J)]+\ldots+V_{f(\pi)}[f(J)].$$

If $f(\alpha), f(\beta), \ldots, f(\pi)$ are distinct, for a fixed eigenvalue λ, the nullity of $J-\lambda I$ is the same as the nullity of $K_\lambda-\lambda I$, and the nullity of $f(J)-f(\lambda)I$ is the same as the nullity of $f(K_\lambda)-f(\lambda)I$. It follows that

$$d\{V[f(J)]\}-d\{V_\lambda[J]\}=d_\lambda.$$

Summing over distinct eigenvalues, one obtains

$$d\{V[f(J)]\}-d\{V[J]\}=\sum_\lambda d_\lambda.$$

By the statement following the proof of lemma 1 it follows that

$$d\{V[f(A)]\}-d\{V[A]\}=\sum_\lambda d_\lambda.$$

If $f(\alpha)=f(\beta)=\ldots=f(\rho)$, then the nullity of $f(J)-f(\alpha)I$ minus the sum of the nullities of $J-\alpha I$, $J-\beta I,\ldots,$ and $J-\rho I$ is $d_\alpha+d_\beta+\ldots+d_\rho$ and

$$d\{V_{f(\alpha)}[f(J)]\}-d\{V_\alpha[J]\}-d\{V_\beta[J]\}-\ldots-d\{V_\rho[J]\}=d_\alpha+d_\beta+\ldots+d_\rho$$

Summing, one obtains in either case

$$d\{V[f(A)]\}-d\{V[A]\}=\sum_\lambda d_\lambda,$$

where λ runs through all the distinct eigenvalues of A corresponding to nonlinear elementary divisors.

The next theorem concerns the case in which condition 1 holds but condition 2 does not.

Theorem 2. If condition 1 holds, than $V[A]=V[f(A)]$. In this case $\sum_\lambda d_\lambda=0$, where λ varies over all distinct eigenvalues corresponding to nonlinear elementary divisors.

If $f(\alpha)=f(\beta)=\ldots=f(\rho)$, suppose that

$$d\{V_{f(\alpha)}[f(J)]\}=d\{V_\alpha[J]\}+d\{V_\beta[J]\}+\ldots+d\{V_\rho[J]\}=s.$$

Then as in lemma 2 the s-dimensional space $V_\alpha[J]+V_\beta[J]+\ldots+V_\rho[J]$ contains vectors that are not eigenvectors of J, but $V_{f(\alpha)}[f(J)]$ consists solely of eigenvectors of $f(J)$ corresponding to $f(\alpha)$.

Corollary. If $f(\alpha)=f(\beta)=\ldots=f(\rho)$, then

$$d\{V_{f(\alpha)}[f(A)]\}-d\{V_\alpha[A]\}=\sum_\lambda d_\lambda+(p_\lambda+n_\lambda),$$

where λ runs over all eigenvalues among $\alpha,\beta,\ldots,\rho$ which correspond to nonlinear elementary divisors and

where $p_\lambda+n_\lambda$ is the total number of elementary divisors (nonlinear and linear) corresponding to λ.

Finally, the next result covers the case in which conditions 1 and 2 both hold.

Theorem 3. The matrices A and $f(A)$ have identical eigenvectors if, and only if (1) $f'(\lambda)\neq 0$ for all eigenvalues λ of the matrix A corresponding to nonlinear elementary divisors, and (2) the values $f(\mu)$ are distinct for all eigenvalues μ of the matrix A corresponding to linear elementary divisors.

Remark 1. It may readily be seen that $V[J]$ and $V[f(J)]$ each can be generated by a set of linearly independent vectors, each of which has a 1 in a single component and 0 in all the remaining components. Thus if $J=P^{-1}AP$ is the Jordan canonical form of A, than $V[f(A)]$ can be generated by a subset of the column vectors of P.

Remark 2. A simple application of the foregoing theory shows that if A is a 2×2 matrix, then A and $f(A)$ have the same eigenvectors unless either (1) A is diagonable and has distinct eigenvalues α, β for which $f(\alpha)=f(\beta)$, or (2) A is nondiagonable and $f(x)=k(x)(x-\alpha)^2+c$, where α is the eigenvalue of A, $k(x)$ is an arbitrary polynomial, and c is an arbitrary constant.

The following example is given as an illustration:

$$\text{Let } A=\begin{bmatrix} 1 & 0 & 0 & 0 & 0 & 0 & 0\\ 0 & 0 & 1 & 0 & 0 & 0 & 0\\ 0 & 0 & 0 & 1 & 0 & 0 & 0\\ 0 & 0 & 0 & 0 & 0 & 0 & 0\\ 0 & 0 & 0 & 0 & 0 & 0 & 0\\ -1 & -1 & -1 & -1 & -1 & -2 & -1\\ 1 & 0 & 1 & 1 & 0 & -1 & 0 \end{bmatrix}$$

and $f(x)=x^6+x^5-x^4-x^3+2$.

$$\text{For } P=\begin{bmatrix} 1 & 0 & 0 & 0 & 0 & 0 & 0\\ 0 & 1 & 0 & 0 & 0 & 0 & 0\\ 0 & 0 & 1 & 0 & 0 & 0 & 0\\ 0 & 0 & 0 & 1 & 0 & 0 & 0\\ 0 & 0 & 0 & 0 & 1 & 0 & 0\\ 0 & 0 & 0 & 0 & 0 & 1 & 0\\ 1 & 1 & 1 & 1 & 1 & 1 & 1 \end{bmatrix}$$

it may be verified that

$$P^{-1}=\begin{bmatrix} 1 & 0 & 0 & 0 & 0 & 0 & 0\\ 0 & 1 & 0 & 0 & 0 & 0 & 0\\ 0 & 0 & 1 & 0 & 0 & 0 & 0\\ 0 & 0 & 0 & 0 & 1 & 0 & 0\\ 0 & 0 & 0 & 0 & 0 & 1 & 0\\ -1 & -1 & -1 & -1 & -1 & -1 & 1 \end{bmatrix}$$

and that the Jordan canonical form of A is

$$J=P^{-1}AP=\begin{bmatrix} 1 & 0 & 0 & 0 & 0 & 0 & 0\\ 0 & 0 & 1 & 0 & 0 & 0 & 0\\ 0 & 0 & 0 & 1 & 0 & 0 & 0\\ 0 & 0 & 0 & 0 & 0 & 0 & 0\\ 0 & 0 & 0 & 0 & 0 & 0 & 0\\ 0 & 0 & 0 & 0 & 0 & -1 & 1\\ 0 & 0 & 0 & 0 & 0 & 0 & -1 \end{bmatrix},$$

where

$$\begin{cases} K_1=J_1(1)=[1], \\ K_0=\begin{bmatrix} 0 & 1 & 0 & 0\\ 0 & 0 & 1 & 0\\ 0 & 0 & 0 & 0\\ 0 & 0 & 0 & 0 \end{bmatrix}, \quad J_2(0)=\begin{bmatrix} 0 & 1 & 0\\ 0 & 0 & 1\\ 0 & 0 & 0 \end{bmatrix}, \quad J_1(0)=[0], \\ K_{-1}=J_2(-1)=\begin{bmatrix} -1 & 1\\ 0 & -1 \end{bmatrix}. \end{cases}$$

Since

$$\begin{cases} f(0)=f(1)=f(-1)=2, \\ f'(0)=f'(-1)=0, \quad f'(1)\neq 0, \\ f''(0)=0, \end{cases}$$

it follows that

$$f(J)=J^6+J^5-J^4-J^3+2I=\begin{bmatrix} 2 & 0 & 0 & 0 & 0 & 0 & 0\\ 0 & 2 & 0 & 0 & 0 & 0 & 0\\ 0 & 0 & 2 & 0 & 0 & 0 & 0\\ 0 & 0 & 0 & 2 & 0 & 0 & 0\\ 0 & 0 & 0 & 0 & 2 & 0 & 0\\ 0 & 0 & 0 & 0 & 0 & 2 & 0\\ 0 & 0 & 0 & 0 & 0 & 0 & 2 \end{bmatrix}$$

It is readily seen that $V_1[J]$ is generated by $[1,0,0,0,0,0,0]^T$, $V_0[J]$ is generated by $[0,1,0,0,0,0,0]^T$ and $[0,0,0,0,1,0,0]^T$, and $V_{-1}[J]$ is generated by $[0,0,0,0,0,1,0]^T$. Since $V[J]=V_1[J]+V_0[J]+V_{-1}[J]$, it follows that $d\{V[J]\}=4$. Since $f[J]$ is a scalar matrix, $d\{V[f(J)]\}=7$. Hence $d\{[f(A)]\}-d\{V[A]\}=3$. The same result is arrived at by the use of theorem 1, where $\sum_\lambda d_\lambda$ is calculated as in lemma 5. Since $f'(0)=0$, $f''(0)=0$, and $f'(-1)=0$, where 0, -1 are the eigenvalues corresponding to nonlinear elementary divisors, it follows that

$$d_0=n_0^{(1)}(m_0^{(1)}-1)=1\cdot 2=2$$

and

$$d_{-1}=n_1^{(1)}r=1\cdot 1=1$$

and

$$\sum_{\lambda} d_{\lambda} = d_0 + d_{-1} = 2 + 1 = 3,$$

as before. By the corollary following theorem 2,

$$d\{V_2[f(A)]\} - d\{V_1[A]\} = d_0 + d_{-1} + p_0 + p_{-1} + n_0 + n_{-1}$$
$$= 2 + 1 + 1 + 1 + 1 + 0 = 6,$$

which checks with the observed results above.

From a glance at the above eigenvectors generating $V[J]$, it is clear that $V[A]$ is generated by the first, second, fifth, and sixth-column vectors of P. Since $f(A)$ is a scalar, $V[f(A)]$ is generated by all seven column vectors of P.

The author thanks A. H. Clifford, O. Taussky, and N. Wiegmann for their helpful suggestions.

WASHINGTON, December 1, 1952.

Journal of Research of the National Bureau of Standards Vol. 51, No. 1, July 1953 Research Paper 2430

The System Barium Oxide-Boric Oxide-Silica

Ernest M. Levin and George M. Ugrinic

A phase equilibrium diagram for the system BaO-B_2O_3-SiO_2 has been constructed from data, obtained essentially by the quenching method, on 178 ternary compositions. One new compound, $3Ba\cdot O3B_2O_3\cdot 2SiO_2$, melting at 1,009° C and possessing an extremely flat primary field appears, and its optical properties and X-ray diffraction data are given. The $BaO\cdot 4B_2O_3$ and SiO_2 primary phase areas include almost 70 percent of the diagram, and over these areas exists a large region of two-liquid immiscibility. Limited data indicates that the immiscibility gap decreases with increasing temperature. The solid solution region between $2BaO\cdot 3SiO_2$ and $BaO\cdot 2SiO_2$ extends into the interior of the diagram and is complex in nature. An isofract diagram for the quenched glasses is shown. For precise temperature control of a quenching furnace, a self-adjusting, bridge-type controller is described briefly.

1. Introduction

The system barium oxide-boric oxide-silica is of fundamental importance in the ceramic field, and the three end members comprise the major constituents of the large class of barium crown glasses. Other important constituents maybe aluminum- or zinc-oxide in the dense barium crown glasses, lead in the barium flints, and alkalis in the light barium crowns or flints [1].[1] Barium oxide surpasses nearly all other oxides in imparting both high index and low dispersion to glass. Many of the well-corrected, present-day optical systems, such as are found in photographic and projectional equipment, have resulted largely from the use of high barium-oxide-content glasses, which have a favorable relationship between index and dispersion.

The Glass Section of the National Bureau of Standards has been engaged in an extensive study of the refractivity, dispersion, and density in the glass-forming region of the barium-borosilicate system [2]. The phase equilibrium diagram for the system is of paramount importance in the interpretation of the data as regards the structure of these glasses. The high silica-boric oxide portion of the system, also, has possible application to the development of improved enamels and ceramic glazes. Notwithstanding the fundamental and practical importance of the ternary diagram, however, no systematic study of the phase equilibrium relationships has been reported.

The ternary system is of additional interest from several theoretical considerations. It contains one binary system (BaO-B_2O_3) with an immiscibility gap and another (BaO-SiO_2) with a portion of the liquidus curve approaching that of two-liquid immiscibility. In the BaO-SiO_2 system, $BaO\cdot 2SiO_2$ and $2BaO\cdot 3SiO_2$ show unusual behavior for refractory oxide systems, in that they form a complete isomorphous solid solution series without a maximum or a minimum. As a secondary objective, it was hoped that investigation of the ternary system might provide additional information on these problems.

[1] Figures in brackets indicate the literature references at the end of this paper.

2. Experimental Procedure

2.1. Raw Materials

The starting materials were silica gel ($SiO_2\cdot nH_2O$), boric acid (H_3BO_3), and either barium nitrate ($Ba(NO_3)_2$) or barium carbonate ($BaCO_3$). The silica gel, 99.99 percent pure on an ignited weight basis, was specially prepared by an acid digestion process in the Chemistry Division of the National Bureau of Standards. The remaining starting materials were of reagent quality, meeting ACS specifications.

2.2. Preparation and Analysis of Mixtures

Because of the volatility of boric acid and the extreme hygroscopicity of boric oxide [3, 4], it was found advantageous in preparing ternary mixtures to add the boric oxide already combined with the baria. For this purpose a stock quantity of each of the four barium borates, $3BaO\cdot B_2O_3$, $BaO\cdot B_2O_3$, $BaO\cdot 2B_2O_3$, $BaO\cdot 4B_2O_3$, was prepared by mixing, grinding, sintering or fusing the appropriate amounts of boric acid and barium nitrate or carbonate. The product was ground to pass a No. 200 mesh screen and heated again. The process of grinding and reheating was repeated 2 or 3 times, until a homogeneous product, by petrographic examination, was obtained. Barium carbonate was used as the source of BaO for preparing $3BaO\cdot B_2O_3$; for the other borates, barium nitrate was used. The barium borates thus prepared were analyzed [4] for BaO and B_2O_3. Previous experience had indicated the approximate excess of boric acid required to formulate each compound, and in no case did the actual chemical composition vary from the theoretical compound composition by more than 0.5 percent. No attempt was made to adjust compositions to theoretical values, and the analyzed values were applied in subsequent calculations.

Stock quantities of the 4 barium silicates, $2BaO\cdot SiO_2$, $BaO\cdot SiO_2$, $2BaO\cdot 3SiO_2$, and $BaO\cdot 2SiO_2$,

259947—53——4

TABLE 1. *Agreement between some formulated and analyzed compositions*

Composition number	Starting materials	Composition					
		Formulated [a]			Analyzed [b]		
		BaO	B_2O_3	SiO_2	BaO	B_2O_3	SiO_2
		%	%	%	%	%	%
C—$2BaO{\cdot}SiO_2$ [c]	$BaCO_3$, SiO_2	83.63	.....	16.37	83.53	.....	16.47
E—$BaO{\cdot}2SiO_2$ [c]	$BaCO_3$, SiO_2	56.08	.....	43.92	55.94	.....	44.06
24	$BaO{\cdot}2B_2O_3$, $2BaO{\cdot}3SiO_2$	55.24	35.60	9.26	55.11	35.51	9.38
29	$BaO{\cdot}4B_2O_3$, $BaO{\cdot}2SiO_2$	47.69	25.92	26.39	47.78	25.98	26.24
J—$3BaO{\cdot}3B_2O_3{\cdot}2SiO_2$ [c]	[d] $BaCO_3$, SiO_2, H_3BO_3	58.30	26.48	15.22	58.48	26.24	15.28

[a] From composition and amounts of starting materials.
[b] By analytical determination.
[c] Stock supply.
[d] 400-g batch prepared. B_2O_3 added as boric acid, which accounts for a little larger discrepancy, in this case between formulated and analyzed compositions.

and of 1 ternary compound, $3BaO{\cdot}3B_2O_3{\cdot}2SiO_2$, were prepared in a similar manner. Barium carbonate exclusively was used as the source of BaO in preparing the barium silicates.

Most of the ternary compositions were prepared to lie on joins connecting the compositions of barium borates, barium silicates, and the one ternary compound $3BaO{\cdot}3B_2O_3{\cdot}2SiO_2$. In making up such series, the amounts of conjugate stock compounds required to yield 3-g mixtures were calculated, by applying the well-known lever principle. The calculated amounts, weighed into dry bottles, were shaken thoroughly with a mechanical mixer for a minimum of 1 hr, ground with a mechanical grinder for 1 hr, and then heated for several hours at some temperature between the solidus and the liquidus. The products were ground to pass a No. 200 mesh sieve and were resintered at a slightly higher temperature, but still below the liquidus. Once again, the products were ground and passed through a No. 200 mesh sieve. This treatment, in most cases, gave a fairly uniform product, as examined with a polarizing microscope. In a few instances, it was necessary to heat the material a third time. All heating was done in platinum crucibles by using an electrically heated furnace. Analysis of representative mixtures prepared as described showed satisfactory agreement between actual and theoretical compositions. Table 1 gives this agreement for several compounds and mixtures. The few compositions not on tie lines were made from appropriate quantities of either 2 already prepared mixtures or 3 stock compounds.

Analysis of ternary compositions consisted of determinations for ignition loss, silica, and baria; boric oxide was obtained by difference. Half-gram samples were decomposed by 1:1 HCl, evaporated almost to dryness, and the moist residue evaporated three times with 10-ml portions of methyl alcohol to remove the boric oxide. Silica was determined by double dehydration in the usual way; baria was precipitated and weighed as $BaSO_4$.

Figure 1 shows the 178 compositions investigated, together with the joins along which most of them were fromulated. It may be noted that many compositions in close proximity to each other were formulated on different joins, thus contributing statistically to the over-all accuracy of the method.

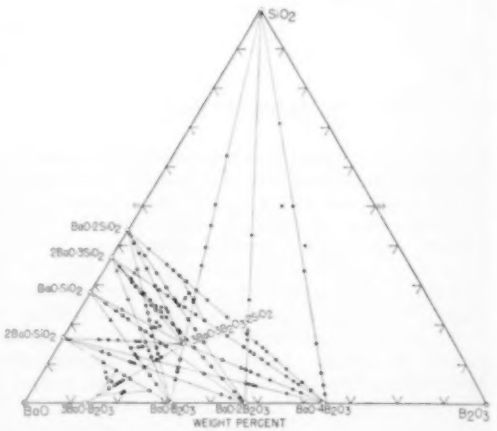

FIGURE 1. *Compositions studied in the system* $BaO–B_2O_3–SiO_2$, *together with the joins along which most of them were formulated.*

It might also be emphasized that the prepared compositions always consisted of crystalline or mixtures of crystalline and glassy phases, as equilibrium conditions could be approached more rapidly by melting than by crystallization from above the liquidus.

2.3. Apparatus and Method

Phase equilibria relationships in the system were obtained by the well established quenching technique [5, 6]. Charges of about 20 mg were heated in the relatively constant temperature zone (hottest region) of a vertical tube, platinum 80 percent-rhodium 20 percent wound, resistance furnace [7]. Constant-temperature control in this zone to within ± 0.3 deg. C was achieved with the use of a newly designed, self-adjusting, a-c bridge-type controller, described later.

Temperatures were measured with platinum versus platinum-rhodium (10%) thermocouples, which were originally calibrated against a standard thermocouple by the Pyrometry Laboratory of the National Bureau of Standards. All temperature values are given on the International Temperature Scale of 1948, based on absolute millivolts [8]. Be-

tween 630.5° and 1,063.0° C (the gold point) the differences between the International Temperature Scales of 1948 and 1927 are less than 0.5 deg. C. At 1,500° C, however, the International Scale of 1948 is 2.3 deg. C less than the scale of 1927; and at 2,000° C, the difference is 6.4 deg. C [9]. In reviewing the literature of high-temperature phase studies, it is found that many investigators go into great detail concerning the accuracy of thermocouple calibrations, yet never specify the temperature scale used. It cannot be safely assumed that all temperature values after January 1, 1948, are reported on the International Temperature Scale of 1948, even though on that day, by international agreement, the change from international to absolute units became effective. The changeover at the National Bureau of Standards, for example, did not become effective until January 1, 1949. Since 1914 the Geophysical Laboratory of the Carnegie Institution of Washington has used a temperature scale based on the work of Day and Sosman. The scale is in good agreement with the International Temperature Scale of 1948, up to about 1,550° C.

The thermocouple calibrations were checked periodically against the melting points of barium tetraborate (889° C) [4], the ternary compound, $3BaO{\cdot}3B_2O_3{\cdot}2SiO_2$ (1,009° C), gold (1,063° C), barium borate (1,105° C) [4] and barium disilicate (1,416° C).[2]

Quenched samples were crushed and examined with the polarizing microscope, using the standard immersion media methods. Refractive indices measured by this method are accurate to within ± 0.003 for n_D.

X-ray diffraction powder patterns (with copper K alpha radiation) were made for a number of compounds and mixtures. A commercial type Geiger counter X-ray spectrometer equipped with a synchronous motor-driven scanning unit and attached to an electronic high-speed recorder was used for this purpose.

2.4 Adjusting, Bridge-type Controller

A self-adjusting, bridge-type controller suitable for precise temperature control of a quenching furnace was designed and assembled from commercially available components by F. A. Mauer of the National Bureau of Standards. Like the electric-furnace thermostat developed by H. S. Roberts at the Geophysical Laboratory in 1925 [7], the controller operates on the change of resistance that accompanies a change in temperature of the furnace winding. The contacting galvanometer has been replaced by a servo amplifier (A, fig. 2), which provides power to operate a reversible, two-phase motor, M. As the amplifier operates on a 60-cycle a-c signal, the power for the furnace is adjusted by means of a variable autotransformer. This transformer is positioned by the reversible motor and provides the power required to maintain the furnace winding at the temperature prescribed by the resistance setting. The temperature is maintained constant, of course, only if volatilization of the winding is negligible.

[2] In accordance with the International Temperature Scale of 1948.

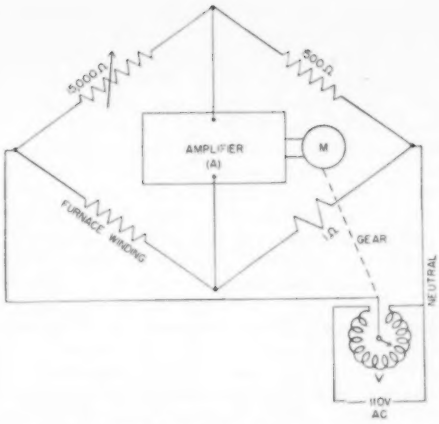

FIGURE 2. *Schematic diagram of self-adjusting, bridge-type controller for high-temperature furnace.*

A, Servo amplifier; M, reversible balancing motor, 27 rpm; V, variable autotransformer.

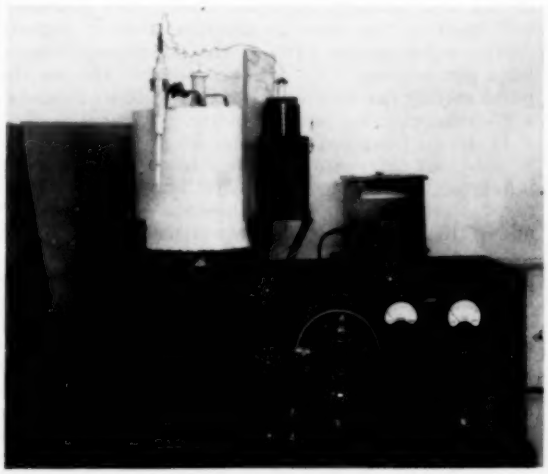

FIGURE 3. *Temperature controller together with the quenching furnace and the temperature measuring equipment.*

Figure 2 shows a schematic diagram of the controller, and figure 3 shows the controller, together with the quenching furnace and the temperature measuring equipment.

The controller offers a combination of features that have not been available in any one instrument. These principal advantages are as follows:

1. Control of temperature to within ± 0.3 deg. C.
2. Elimination of process lags by use of the furnace winding as the sensing element.
3. Use of alternating current to heat the furnace. This feature is important because a-c power is readily available, permits the use of a variable autotransformer to adjust the voltage without

wasting power, and also permits amplification of the signal from the bridge.

4. Incorporation of proportional speed floating control with automatic reset. When the temperature departs only slightly from the control point, the autotransformer moves at a rate proportional to the departure. In the case of a large unbalance, the motor turns at an essentially constant speed until balance is reached. Because the motor rotates as long as the temperature remains different from the required temperature, the variac automatically assumes a new position for each temperature setting and even compensates for change in the line voltage of up to 20 percent. As long as power requirements and line voltage remain constant, oscillations of the balancing motor are barely perceptible. Consequently, even if the controller is switched off, the temperature will remain within a few degrees of the control point. This characteristic simplifies the problem of controlling the furnace in a desired temperature range so that it can be ready for use on the following day.

5. Simplification of operating procedure. A single knob is used for resetting the control point. Because of the reset action described above, the controller will position the variable autotransformer without further attention, to provide the power requirement for a new setting of the balance point. The control point setting can be varied continuously by means of a 10-turn precision potentiometer.

It should be noted that since an a-c bridge circuit is used, an impedance balance must be effected if maximum precision is desired. The bridge output can be recorded on an oscilloscope and capacitors added to the high-impedance arms of the bridge until a true null can be obtained [10].

The principal maintenance problem is presented by the variable autotransformer brushes. During operation, the "hunting" of the controller keeps the brushes moving back and forth between adjacent windings. Experience indicates that after about 6 months of operation, arcing may occur between the brushes and the slightly roughened windings. In this case, the brushes are cleaned or replaced, and the windings are cleaned according to the manufacturer's instructions.

3. Limiting Binary Systems

3.1. System BaO-B_2O_3

The binary system BaO-B_2O_3 was reported by Levin and McCurdie [4]. It is distinguished by a region of two-liquid immiscibility extending from about 70 percent of B_2O_3 (30 percent of BaO) to almost pure B_2O_3. Extrapolation from ternary data to the binary indicated that the reported binary liquidus temperatures were uniformly low by about 10° C. New determinations on the binary compounds confirmed this conclusion. A corrected diagram is reproduced as figure 4.

3.2. System B_2O_3-SiO_2

Only limited information is available about the system B_2O_3-SiO_2, and no liquidus values are known,

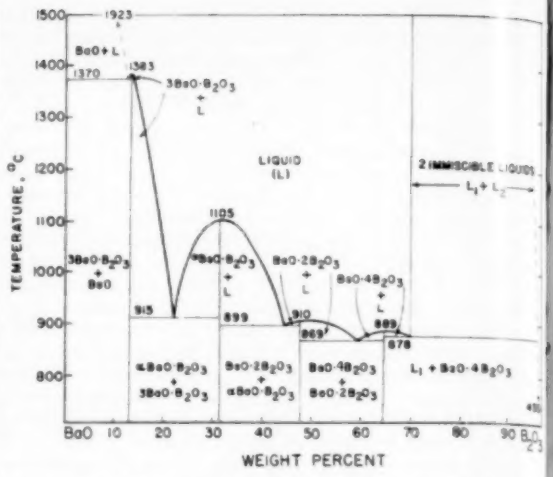

FIGURE 4. *Phase equilibrium diagram for the system* BaO–B_2O_3 [4].
Liquidus values have been raised by a uniform amount of 10° C.

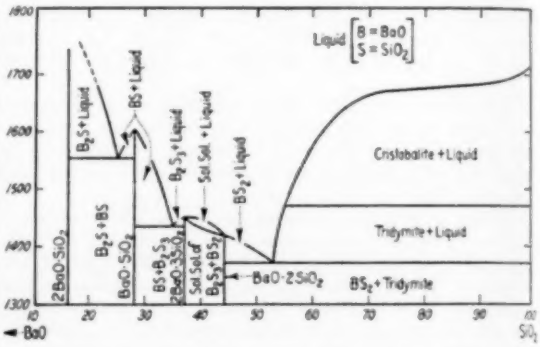

FIGURE 5. *The Binary system* BaO-SiO_2, [12, 15].
Liquidus values not changed to International temperature scale of 1948.

as no mixture in the system has been crystallized. Morey [11] was unable to crystallize any mixture in the system, either from a dry mix or by hydrothermal treatment. Greig [12], and Cousin and Turner [13] believe that the oxides as liquids are completely miscible in all proportions. The latter authors, on the basis of thermal expansion and density-composition curves, could find no indication of compound formation. N. K. Dertev and T. H. Khudyakova [14], however, believe that several compounds (formulas unspecified) are possible.

3.3. System BaO-SiO_2

The binary system BaO-SiO_2, as shown in figure 5, was investigated originally by Eskola [15] and modified later by Greig [12]. It shows two regions of particular interest. In the first, dibarium trisilicate ($2BaO$-$3SiO_2$) and barium disilicate (BaO-$2SiO_2$) form a complete solid solution series. The liquidus

TABLE 2. *Comparison of X-ray diffraction data for compounds in the system* BaO-SiO_2

$2BaO \cdot SiO_2$				$BaO \cdot SiO_2$				$2BaO \cdot 3SiO_2$				$BaO \cdot 2SiO_2$			
(a)		(b)		(a)		(b)		(a)		(b)		(a)		(b)	
d	I[d]	d	I	d	I	d	I	d	I	d	I	d	I	d	I
Å	%	Å	%	Å	%	Å	%	Å	%	Å	%	Å	%	Å	%
		5.1	10	5.19	19			7.11	15	7.0	12	7.00	14		
		4.4	10	4.20	10	4.22	13	6.06	11	6.05	6	6.87	13	6.7	9
4.23	20	4.23	19	3.73	55 (3)	3.70	40 (2)			5.00	6	5.63	17		
		3.78	7	3.58	17			3.93	13	4.33	6	4.75	12		
		3.53	12	3.43	100 (1)	3.41	100 (1)	3.79	100 (1)	3.75	100 (1)	4.15	8		
3.43	63	3.44	64 (3)	3.36	57 (2)	3.34	22	3.71	75	3.68	80 (2)	4.02	77 (3)	4.00	100 (1)
3.17	16	3.18	29	3.13	50	3.13	34	3.51	10			3.57	32	3.55	20
3.11	14	3.12	28			3.02	10	3.44	10	3.43	6	3.39	14		
3.03	100 (1)[c]	3.04	100 (1)			2.94	8	3.33	87 (2)	3.30	70	3.36	23		
2.95	95 (2)	2.94	100 (2)	2.84	32	2.81	28	3.28	76 (3)	3.26	42	3.27	25	3.28	23
2.91	82 (3)			2.75	18	2.77	24	3.15	48	3.13	35	3.15	100 (1)	3.14	60 (2)
2.69	10	2.69	18	2.71	23					2.99	6	3.11	87 (2)		
2.56	8			2.59	9	2.59	10	2.78	74	2.78	75 (3)	2.86	27		
2.53	14	2.53	20			2.45	8	2.61	8	2.60	9	2.76	40	2.77	36
2.44	36	2.44	32	2.36	31	2.35	25			2.55	6	2.69	7		
2.40	25	2.4	32	2.30	35			2.41	8	2.40	9	2.61	12	2.60	10
2.30	6	2.31	10	2.24	31	2.25	34	2.36	35	2.35	14	2.36	16		
2.24	27	2.255	45	2.19	5			2.28	45	2.27	23	2.35	16	2.35	22
2.12	24	2.13	32	2.14	11	2.14	11	2.23	32	2.225	23	2.26	32	2.27	50 (3)
2.10	36	2.11	33	2.09	19	2.09	40 (3)	2.21	24	2.205	13	2.23	29	2.23	50
2.02	8	2.03	16	2.08	36			2.14	60	2.14	41	2.21	51		
1.975	22	1.98	29	2.04	45	2.05	30	2.09	22	2.08	18	2.16	25	2.17	50
		1.94	7	2.01	7			2.04	12	2.04	12	2.06	21	2.06	25
1.909	17	1.91	24	1.977	7	1.99	15	1.981	20	1.98	17	2.05	32		
1.867	22	1.87	28	1.896	32	1.90	29	1.918	14	1.91	14	2.00	7		
1.788	10	1.80	14	1.852	16	1.86	17	1.881	8	1.88	7	1.923	12	1.91	15
1.762	33	1.77	49	1.795	9	1.79	10			1.86	7	1.877	17	1.87	20
		1.73	10	1.781	9			1.825	14	1.825	16	1.827	8		
1.710	47	1.715	48	1.761	12	1.76	13	1.811	17			1.783	16	1.78	12
1.686	11	1.69	15	1.737	12	1.72	14	1.789	25	1.79	20	1.732	9		
1.659	7	1.66	9	1.608	33			1.760	11	1.76	16	1.706	31		
1.645	8	1.64	25	1.635	4			1.745	11	1.71	8	1.601	13		
1.598	5	1.605	8	1.606	7	1.61	7	1.654	22	1.65	12	1.584	9	1.59	10
1.578	3	1.58	7	1.570	10	1.56	9	1.636	10	1.63	6	1.571	15		
1.554	3			1.545	7			1.617	7	1.615	6	1.481	8	1.48	13
		1.52	12	1.517	13	1.525	11			1.60	6	1.458	11	1.46	10
1.511	6	1.51	13	1.486	8					1.58	6	1.408	6		
1.470	4	1.475	8	1.477	8			1.557	11	1.555	8	1.392	6		
1.455	5	1.46	12	1.468	12			1.518	7	1.52	8	1.378	9		
1.442	12	1.445	12	1.448	10			1.513	8			1.292	16	1.29	10
1.432	10	1.435	16	1.430	11			1.505	6	1.505	6	1.288	16		
1.416	7	1.42	9	1.415	8			1.481	6	1.48	6	1.285	10		
1.370	10	1.375	20	1.392	10	1.40	10	1.474	10			1.281	10		
		1.345	12	1.366	10	1.375	9	1.450	6						
1.338	5			1.333	9			1.422	11	1.42	8				
1.315	10	1.32	25	1.315	10	1.315	8	1.406	4						
1.292	5	1.28	16	1.306	7			1.394	31	1.395	14				
1.263	10	1.265	23	1.291	7			1.350	8	1.35	6				
1.248	10	1.25	15	1.279	12	1.28	5	1.342	6	1.33	8				
		1.24	11	1.270	8			1.322	13	1.32	6				
		1.215	8			1.24	5	1.290	10	1.30	15				
		1.19	21			1.15	5	1.249	5	1.25	9				
		1.17	11					1.241	7	1.24	6				
		1.155	25					1.225	5	1.22	6				
		1.14	7					1.200	7	1.20	8				
										1.17	6				
										1.135	9				

[a] Data from present investigation.
[b] Data by A. E. Austin [20].
[c] d=interplanar spacing.
[d] I=relative intensity.
[e] (1), (2), (3)=three strongest peaks in order of intensity.

curve shows no maximum or minimum. R. Thomas [16] concluded from his investigation of the system BaO-Al_2O_3-SiO_2 that dibarium trisilicate is not a compound at all but is merely that particular composition at or near the maximum in a solid solution series.

Another point of interest is the shape of the liquidus curve in the cristobalite primary phase area [12]. Indicative of an approach to two-liquid immiscibility, the curve is almost horizontal for a change in composition of nearly 30 percent. Ol'shanskiĭ [17] investigated the system BaO-SiO_2 above the liquidus, between the temperatures of 1,800° and 2,570° C, but could find no trace of immiscible liquids. However, the S-shaped form of the portion of the liquids curve under discussion is typical of unmixing, or of a miscibility gap, occurring completely below the liquidus [18].

Before investigating the interior of the ternary system, it was considered desirable from the standpoints of experience and of possible additional information that might be gained, to check several of the

TABLE 3. *Data on liquidus determinations in the system* BaO–B_2O_3–SiO_2

A. Compositions in the $BaO \cdot 2SiO_2$ primary field

Composition number	Composition, by weight			Treatment		n of quenched glass (25° C)	Phases present		
	BaO	B_2O_3	SiO_2	Time held before quenching	Temperature		Primary	Other	Glass
	Percent	*Percent*	*Percent*	*hr*	*°C*				
1–107	51.21	15.02	33.77	2	1,066	1.609			All
				½	1,040		×		×
2– 30	51.89	12.95	35.16	1	1,103	1.612			All
				1	1,100		Rare		×
3– 47	53.83	6.94	39.23	1	1,243	1.607			All
				1	1,238		Rare		×
4– 94	54.60	18.91	26.49	1	1,002	1.622			All
				16	997		Very rare		×
				½	999	1.623			All
5– 64	54.61	19.48	25.91	½	995	.....	Rare		×
				½	991		×	$3BaO \cdot 3B_2O_3 \cdot 2SiO_2$	×
				1½	1,055	1.620			All
6– 49	54.94	15.78	29.28	1	1,050	.....	Rare		×
				2½	1,000	.....	Heavy		×
				1½	986		×	$3BaO \cdot 3B_2O_3 \cdot 2SiO_2$	×
7– 93	55.16	11.70	33.14	½	1,150	1.630			All
				¾	1,146	.....	Rare		×
8– 48	55.58	6.93	37.49	1	1,243	1.616			All
				1	1,238		Rare		×
9–100	55.69	16.95	27.36	1	1,050	1.627			All
				1	1,045		Very rare		×
10–186	56.35	2.89	40.76	½	1,345	1.614			All
				½	1,340		Rare		×
11–185	56.56	5.30	38.14	½	1,277	1.623			All
				½	1,273		° Rare		×
				1	1,078	1.627			All
12– 63	56.71	14.61	28.68	1	1,070	.....	×		×
				1	1,000	.....	Heavy		×
				1	980		×	$3BaO \cdot 3B_2O_3 \cdot 2SiO_2$	×
13–184	56.89	8.83	34.28	1	1,214	1.623			All
				1	1,210		° Rare		×
14–163	57.25	12.84	29.91	1	1,130	1.624			All
				1	1,125		Rare		×
15–182	57.73	18.06	24.21	1	1,023	1.633			All
				1	1,019		Rare		×
16–181	57.81	18.86	23.33	1	1,005	1.632			All
				¾	1,003	.....	Very rare		×
				1	995		×	$3BaO \cdot 3B_2O_3 \cdot 2SiO_2$	×
17–206	58.6	17.2	24.2	1	1,048	1.632			All
				1	1,044	.....	Rare		×
				1½	1,010	1.633			All
18– 41	59.15	17.63	23.22	1	1,005	.....	×		×
				19	984		Heavy	$3BaO \cdot 3B_2O_3 \cdot 2SiO_2$	×
19– 90	59.47	15.79	24.74	1½	1,049	1.638			All
				1	1,045		Rare		×
				1	1,085	1.635			All
20– 91	59.88	13.94	26.18	1	1,081	.....	×		×
				1	1,070	.....	Heavy	$2BaO \cdot 3SiO_2$	×

B. Compositions in the $1BaO \cdot 3SiO_2$ primary field and solid-solution area

21– 51	59.02	6.97	34.01	1	1,278	1.626			All
				1	1,273		[b] ss		×
22– 62	59.98	7.01	33.01	½	1,244	1.630			All
				½	1,238		[b] ss		×
23–175	60.21	16.16	23.63	1	1,042	1.638			All
				½	1,037		Rare		×
24– 26	60.41	11.83	27.76	1	1,125	1.638			All
				¾	1,120		Rare		×
25–176	60.49	14.53	24.98	¾	1,073	1.633			All
				¾	1,068		[c] Rare		×
26–177	61.13	10.81	28.06	1	1,152	1.638			All
				1	1,147		[c] ×		×
				½	1,000	1.643			All
27–202	61.42	18.13	20.45	1	999	.....	Very rare		×
				1	991		Moderate		×
				1	981		Heavy	$3B_2O \cdot 3B_2O_3 \cdot 2SiO_2$	×
28–178	61.46	8.90	29.64	¼	1,201	1.638			All
				¼	1,196		Rare		×
29– 42	61.47	6.96	31.57	1	1,245	1.638			All
				1	1,240		[b] ss		×
30–179	61.68	7.63	30.69	1	1,226	1.638			All
				1	1,223		[b] ss		×
31– 54	61.74	13.40	24.86	½	1,089	1.640			All
				1	1,085		Rare		×
32– 79	62.29	14.71	23.00	¾	1,064	1.642			All
				1	1,061		Rare		×
33–180	62.49	2.90	34.61	½	1,365	1.637			All
				½	1,360		[b] ss		×
34–172	62.53	18.30	19.17	1	994	1.647			All
				1	990		Rare		×
				½	980		×	$3BaO \cdot 3B_2O_3 \cdot 2SiO_2$	×
35– 52	62.87	16.08	21.05	1½	1,040	1.642			All
				1¼	1,035	.....	Ware		×

See footnotes at end of table.

TABLE 3. *Data on liquidus determinations in the system* BaO–B_2O_3–SiO_2—Continued

B. Compositions in the $1BaO \cdot 2SiO_2$ primary field and solid solution area—Continued

Composition number	Composition, by weight			Treatment		n of quenched glass (25° C)	Phases present		
	BaO	B_2O_3	SiO_2	Time held before quenching	Temperature		Primary	Other	Glass
	Percent	*Percent*	*Percent*	*hr*	*°C*				
36–78	63.42	17.38	19.20	2	1,001	1.645			All
				1	998		Ware		×
37–58	63.59	3.05	33.36	1	1,350	1.640			All
				1	1,345		[b] ss		×
38–59	64.80	9.13	26.07	1	1,182	1.645			All
				1	1,177		[c] Rare		×
39–83	64.92	16.95	18.13	1½	1,001	1.648			All
				2	998		Rare		×
				1½	984		Moderate		×
				1	968		Heavy	$3BaO \cdot 3B_2O_3 \cdot 2SiO_2$	×
40–60	66.01	15.21	18.78	1	1,036	1.649			All
				1	1,031		Rare		×
41–76	66.62	18.25	15.13	1½	976	1.654			All
				1	973		Rare		×
42–55	67.15	11.62	21.23	1	1,102	1.654			All
				1	1,097		[c] Rare		×
43–173	67.22	9.10	23.68	½	1,164	1.654			All
				½	1,159		Very rare		×
44–187	67.52	18.13	14.35	¾	947	1.661			All
				¾	943		Rare		×
45–171	67.65	16.67	15.68	1	982	1.668			All
				1	977		Rare		×

C. Compositions in the $BaO \cdot SiO_2$ primary field

46–84	67.81	9.88	22.31	½	1,145	1.666			All
				½	1,141		Rare		×
47–127	68.48	13.81	15.71	½	995	1.659			All
				1	989		×		×
48–188	68.57	17.19	14.24	1	965	1.670			All
				1	961		Rare		×
49–85	68.61	7.94	23.45	1	1,237	1.667			All
				1	1,232		Rare		×
50–86	69.88	4.84	25.28	½	1,352	~1.67	Very rare		×
				2	964	1.664			All
51–31	70.02	17.68	12.30	1¼	960		Rare		×
				1½	950		Moderate		×
				1	943		Moderate	$BaO \cdot B_2O_3$	×
52–22	70.22	15.71	14.07	1	1,016	1.665			All
				½	1,013		Rare		×
53–23	71.04	7.86	21.10	1	1,305	1.669			All
				1	1,298		×		×
54–168	72.01	17.69	10.30	½	975	1.672			All
				⅔	970		Rare		×
55–126	72.08	12.05	15.87	½	1,189	1.683			All
				1	1,184		Rare		×
56–125	74.13	9.91	15.96	½	1,250	1.681			All
				½	1,244		Rare		×
57–70	74.93	18.16	6.91	1	961				All
				½	959		Rare		×
58–169	75.69	12.08	12.23	½	1,160				All
				½	1,155		Very rare		×
59–110	76.06	18.24	5.70	1	950	1.684			All
				1	946		Rare		×
60–37	76.11	15.70	8.19	¾	1,038	1.680			All
				¾	1,030		Rare		×
61–158	76.83	17.88	5.29	1	954	1.696			All
				1	949		×		×
62–157	77.61	17.53	4.86	1	959	1.695			All
				½	954		Rare		×
63–200	78.02	17.34	4.64	1	962	1.698			All
				1	957		Rare		×
				1	952		Moderate	$3BaO \cdot B_2O_3$	×

D. Compositions in the $2BaO \cdot SiO_2$ primary field

64–124	76.01	7.95	16.04	½	1,308	~1.69			[d] All
				½	1,302		Rare		×
65–170	76.71	10.54	12.75	1	1,263	1.696			All
				1	1,258		Rare		×
				½	1,200		Moderate		×
				½	1,160		Moderate	$BaO \cdot SiO_2$	×
66–71	77.99	11.78	10.23	1	1,224	~1.694			[d] All
				1½	1,206		×		×
67–201	78.40	16.12	5.48	1	1,055	1.698			All
				1	1,050		Rare		×
68–156	78.72	13.43	7.85	1	1,274	1.704			All
				1	1,270		×		×
69–155	79.16	14.43	6.41	2	1,223	1.704			All
				1	1,217		Rare		×
70–72	79.39	8.84	11.77	½	[e] 1,359		Moderate		[d] ×
				½	1,344		Heavy		×

See footnotes at end of table.

TABLE 3. *Data on liquidus determinations in the system* $BaO–B_2O_3–SiO_2$—Continued

E. Compositions in the $3BaO·B_2O_3$ primary field

Composition number	Composition by weight			Treatment		*n* of quenched glass (25° C)	Phases present		
				Time held before quenching	Temperature		Primary	Other	Glass
	Percent	*Percent*	*Percent*	*hr*	°C				
71–199	77.82	19.76	2.42	1	910	1.698			All
				1	906	.....	Very rare		×
				½	900	.....	Moderate	Rare $BaO·B_2O_3$	×
				1	[c] 875	.....	Heavy	$(BaO·B_2O_3)(BaO·SiO_2)$	×
72–109	80.04	16.42	3.54	¾	1,077	1.705			All
				1	1,073	.....	Rare		×
73–108	83.05	15.05	1.90	1½	1,206	.....			[a] All
				½	1,198	.....	×		[b] ×

F. Compositions in the $BaO·B_2O_3$ primary field

74–165	54.88	43.79	1.33	½	897	1.620			All
				½	892	.....	Moderate		×
75–166	56.46	41.38	2.16	½	926	1.622			All
				½	921	.....	Rare		×
76–116	62.80	28.13	9.07	¾	1,002	1.645			All
				1¼	999	.....	Rare		×
				¾	996	.....	Moderate	$3BaO·3B_2O_3·2SiO_2$	×
77–115	63.47	28.42	8.11	¾	1,028	1.646			All
				½	1,023	.....	Rare		×
78–114	64.93	29.06	6.01	1	1,054	1.649			All
				¾	1,050	.....	×		×
79–113	65.09	23.23	11.68	1½	993	1.652			All
				1	988	.....	Rare		×
80–77	65.82	23.06	11.12	2	992	1.653			All
				1	987	.....	Moderate		×
81–75	66.98	20.08	12.94	1	989	1.656			All
				¾	985	.....	Rare		×
82–61	67.22	21.30	11.48	1	984	1.653			All
				¾	979	.....	Rare		×
83–21	69.41	23.56	7.03	1	1,025	1.663			All
				1	1,020	.....	×		×
84–73	69.58	25.73	4.69	1	1,077	1.663			All
				1½	1,074	.....	Rare		×
85–112	69.84	21.07	9.09	¾	1,003	1.662			All
				¾	999	.....	Rare		×
86–74	70.24	18.32	11.44	2	982	1.662			All
				1	958	.....	Rare		×
				¾	954	.....	Moderate	$BaO·SiO_2$	×
87–167	71.38	18.66	9.96	⅔	968	1.680			All
				½	963	.....	Rare		×
88–36	71.41	25.52	3.07	1	1,057	1.664			All
				¾	1,053	.....	Moderate		×
89–35	74.23	19.63	6.14	1	951	1.674			All
				1	946	.....	Rare		×
90–111	74.70	18.85	6.45	1	939	1.678			All
				1	934	.....	×		×
91–189	77.00	20.00	3.00	1	925	1.696			All
				½	920	.....	Rare		×

G. Compositions in the $BaO·2B_2O_3$ primary field

92–96	39.30	55.04	5.66	½	845	1.568			All
				½	841	.....	Rare		×
				½	835	.....	Moderate	$BaO·4B_2O_3$	×
93–147	40.26	52.80	6.94	½	841	1.573			All
				⅓	839	.....	Rare		×
94–119	40.57	55.81	3.62	¼	858	1.572			All
				1	853	.....	Rare		×
95–151	42.42	55.09	2.49	½	877	1.578			All
				1	872	.....	Moderate		×
96–148	42.65	47.25	10.10	½	841	1.588			All
				½	838	.....	Rare		×
97–149	43.49	45.30	11.21	½	840	1.589			All
				½	835	.....	Rare		×
98–120	44.21	49.81	5.98	½	870	1.592			All
				¼	867	.....	Rare		×
99–162	46.25	46.44	7.31	½	885	1.595			All
				½	880	.....	Rare		×
100–152	48.05	47.56	4.39	¾	884	1.598			All
				¾	881	.....	Rare		×
101–203	48.55	46.90	4.55	½	884	1.602			All
				½	877	.....	Moderate		×
102–164	52.90	45.71	1.39	½	906	1.617			All
				½	900	.....	Rare		×
103–80	53.69	44.37	1.94	½	897	1.618			Al
				1	894	.....	Rare		×l

See footnotes at end of table.

TABLE 3. *Data on liquidus determinations in the system* BaO–B_2O_3–SiO_2—Continued

H. Compositions in the $BaO \cdot 4B_2O_3$ primary field

Composition number	Composition, by weight			Treatment		n of quenched glass (25° C)	Phases present		
	BaO	B_2O_3	SiO_2	Time held before quenching	Temperature		Primary	Other	Glass
	Percent	*Percent*	*Percent*	*hr*	°C				
104–193	18.0	62.0	20.0	½	874	1.45–1.542			All 2 glasses
				1	871		Rare		2 glasses
105–134	23.24	43.11	33.65	2	830	1.457–1.53			All 2 glasses
				3	825		Rare		2 glasses
106–29 [1]	29.05	70.95	.....	¼	880	1.464–1.535			All 2 glasses
				¼	876		Rare		2 glasses
107–133	29.63	54.99	15.38	18	841	1.44–1.55			All 2 glasses
				2	836		Rare		2 glasses
108–137	32.33	59.98	7.69	1	861	1.545			All 2 glasses
				½	856		Rare		2 glasses
109–138	33.34	61.85	4.81	2	870	1.548			All 2 glasses
				½	865		Rare		2 glasses
110–132	34.18	63.42	2.40	½	875	1.55			All
				¾	872		Rare		×
111–43	36.70	59.87	3.43	1	864	1.556			All
				1	860		Rare		×
112–101	37.62	56.94	5.44	½	854	1.563			All
				½	851		Moderate		×
113–146	38.71	56.41	4.88	½	845	1.565			All
				½	840		Rare		×
114–118	39.33	57.86	2.81	½	830	1.567	Moderate	$BaO \cdot 2B_2O_3$	×
				½	861				All
				¼	857		Rare		×

I. Compositions in the SiO_2 primary field

115–136	10.10	18.75	71.15	2	[2] 960	1.459	×		2 Glasses
116–135	17.51	32.49	50.00	17	830	~1.45–~1.55			All 2 glasses
				1½	821		×		2 Glasses
117–195	20.0	30.0	50.0	½	[2] 860	~1.56	×		2 Glasses
118–194	20.0	40.0	40.0	½	[2] 826	1.56–1.55	×		2 Glasses
				½	821		×	$BaO \cdot 4B_2O_3$	2 Glasses
119–145	25.55	11.41	63.04	½	[2] 1,278	~1.47–~1.57	×		2 Glasses
120–142	29.85	27.18	42.97	18	1,018	~1.46–~1.58			All 2 glasses
				2	960		×		2 Glasses
121–144	34.13	15.25	50.62	½	1,350	~1.46–~1.56			All 2 glasses
				½	1,314		×		2 Glasses
122–161	37.76	16.87	45.37	1	[2] 1,201	~1.57	×		2 Glasses
123–141	38.54	35.09	26.37	1	[2] 922	~1.46	×		2 Glasses
				56	910		×		2 Glasses
124–140	42.63	38.82	18.55	1	915	~1.59			All 2 glasses
				2	910		×		2 Glasses
125–27	39.28	51.91	8.81	3	826	1.573			All
				1½	823		×		×
				1½	814		×	$BaO \cdot 2B_2O_3$	×
126–102	40.36	48.52	11.12	½	838	1.577			All
				½	830		×		×
				1	816		×	$BaO \cdot 2B_2O_3$	×
127–44	41.37	45.43	13.20	1	834	1.582			All
				1	830		Rare		×
				16	810		×	$BaO \cdot 2B_2O_3$	×
128–160	41.72	18.64	39.64	1	[2] 1,200		×		×
129–103	41.81	44.02	14.17	½	860	1.588			All
				½	850		×		×
				½	835		×	$BaO \cdot 2B_2O_3$	×
130–104	42.46	42.01	15.53	¼	860	1.588			All
				¼	847		×		×
131–139	43.91	39.08	16.11	1	891	1.592			All
				½	880		×		×
				2	870		×	$3BaO \cdot 3B_2O_3 \cdot 2SiO_2$	×
132–131	45.05	20.12	34.83	1	1,102	1.595			All
				1	1,055		Rare		×
				1	955	1.600			All
133–45	45.56	32.52	21.92	1½	950		Rare		×
				1	900		×	$3BaO \cdot 3B_2O_3 \cdot 2SiO_2$	×
134–29	47.69	25.92	26.39	½	1,101	1.606			All
				1	996		×		×
135–105	48.79	22.49	28.72	1½	1,008	1.610			All
				1	1,004		×		×

See footnotes at end of table.

TABLE 3. *Data on liquidus determinations in the system* $BaO–B_2O_3–SiO_2$—Continued

Composition number	Composition, by weight			Treatment		n_D of quenched glass (25° C)	Phases present		
	BaO	B_2O_3	SiO_2	Time held before quenching	Temperature		Primary	Other	Glass
	Percent	*Percent*	*Percent*	*hr*	°C				
I. Compositions in the SiO_2 primary field—Continued									
136–191	49.79	22.34	27.87	½	1,005	1.615			All
				½	1,000		Rare		×
137–46	49.89	19.13	30.98	1½	1,015	1.611			All
				1½	1,010		×		×
138–106	50.59	16.94	32.47	1	1,032	~1.61			All
				1	1,026		×	$BaO·2SiO_2$	×
139–143	50.64	22.62	26.74	1	1,002	1.616			All
				1	996		×		×
140–192	50.69	21.41	27.90	½	1,005	1.615			All
				½	1,000		Rare		×
141–190	51.43	23.08	25.49	1	1,000	1.615			All
				1	986		Rare		×
				1	993		×	$3BaO·3B_2O_3·2SiO_2$	×
J. Compositions in the $3BaO·3B_2O_3·2SiO_2$ primary field									
142–66	44.98	41.87	13.15	1	850	1.593			All
				2	844		×		×
143–97	45.80	39.94	14.26	1	897	1.601			All
				1	892		Rare		×
144–163	47.43	44.49	8.08	½	904	1.600			All
				1	901		Rare		×
145–65	47.92	35.05	17.03	1	965	1.607			All
				1	960		Rare		×
146–121	48.49	42.74	8.77	1	924	1.604			All
				1	919		×		×
147–122	49.02	41.86	9.12	1	936	1.605			All
				1	932		Rare		×
148–204	49.25	45.96	4.79	½	890	1.604			All
				½	886		Moderate	Very rare $BaO·2B_2O_3$	×
149–205	49.95	45.02	5.03	½	904	1.606			All
				½	899		Rare		×
150–67	50.85	28.24	20.91	1	986	1.613			All
				1	980		Rare		×
151–198	52.06	21.14	26.80	1	995	1.617			All
				1	989		×		×
152–98	52.09	25.33	22.58	½	997	1.623			All
				½	992		×		×
153–123	52.10	26.78	11.12	¼	985	1.617			All
				¼	979		Rare		×
154–38	53.41	43.90	2.69	1½	900	1.615			All
				1	894		Rare		×
				2	886		Moderate	$BaO·2B_2O_3$	×
155–90	53.56	21.92	24.52	1	998	1.620			All
				1	995		Rare		×
156–92	53.66	30.78	15.56	½	1,033	1.622			All
				¼	998		×		×
157–50	54.11	27.18	18.71	1	1,000	1.622			All
				1	996		Moderate		×
158–34	54.32	24.37	21.31	1½	1,001	1.625			All
				1½	998		Moderate		×
159–39	54.38	39.45	6.17	1	957	1.620			All
				1¼	954		Rare		×
160–93	54.46	20.67	24.87	1	999	1.622			All
				1	995		Rare		×
				1½	984		Moderate	$BaO·2SiO_2$	×
161–24	55.24	35.50	9.26	½	988	1.628			All
				1	981		Rare		×
162–87	55.72	32.52	11.76	¼	1,002	1.628			All
				½	998		Rare		×
163–40	56.56	29.47	13.97	1	1,005	1.629			All
				1	1,000		Moderate		×
164–68	57.15	26.79	16.06	1½	1,008	1.631			All
				1½	1,005		Moderate		×
165–32	57.67	24.37	17.96	1½	1,008	1.633			All
				1	1,004		Moderate		×
				1	985	1.631			All
166–57	57.72	34.85	7.43	¾	980		Rare		×
				1	951		Moderate		×
				1	940		Large	$BaO·B_2O_3$	×
167–25	57.83	23.66	18.51	1	1,005	1.634			All
				1	1,001		Rare		×
168–88	58.11	21.83	20.06	2	1,005	1.631			All
				2	1,000		×		×
169–69 [b]	58.30	26.48	15.22	½	1,013	1.638			All
				½	1,011		Very rare		×
170–89	58.63	19.51	21.86	2½	1,002	1.634			All
				1	998		Rare		×
171–174	59.82	18.43	21.75	1	997	1.638			All
				1	994		×		×
172–197	61.30	19.49	19.21	1	995	1.641			All
				1	990		Rare		×
173–117	61.41	27.52	11.07	1	1,007	1.642			All
				1	1,005		Rare		×
				1	994		Moderate	$BaO·B_2O_3$	×

See footnotes at end of table.

TABLE 3. *Data on liquidus determinations in the system* BaO–B_2O_3–SiO_2—Continued

J. Compositions in the $3BaO \cdot 3B_2O_3 \cdot 2SiO_2$ primary field—Continued

Composition number	Composition, by weight			Treatment		n of quenched glass (25° C)	Phases present		
	BaO	B_2O_3	SiO_2	Time held before quenching	Temperature		Primary	Other	Glass
	Percent	*Percent*	*Percent*	*hr*	*°C*				
174–56	62.44	23.23	14.33	1	996	1.641	.....	.....	All
				1	992		Moderate	.....	×
175–81	63.13	21.31	15.56	1	998	1.645	.....	.....	All
				1½	993		Rare	.....	×
176–82	64.20	18.70	17.10	1½	978	1.647	.....	.....	All
				1	974		Rare	.....	×
177–198	64.77	21.39	13.84	1	985	1.648	.....	.....	All
				1	981		Rare	.....	×
178–53	65.41	22.10	12.49	1	972	1.648	.....	.....	All
				1	969		Rare	.....	×
				2½	961		Moderate	$BaO \cdot B_2O_3$	×

[a] X-ray powder pattern of crystals grown at 1,100° C showed very slight irregular shift in *d* spacings from pure $BaO \cdot 2SiO_2$. No detectable change in optical properties.
[b] Solid solution with $BaO \cdot 2SiO_2$ and with barium borates, confirmed by optical and X-ray data.
[c] X-ray powder pattern of primary phase crystals showed a maximum shift of 0.02 A in *d* spacings from pure $2BaO \cdot 3SiO_2$. No detectable change in optical properties.
[d] Includes quench growths and barium platinates.
[e] Liquidus greater than this temperature.
[f] Temperature of a ternary invariant point.
[g] All glass devitrified to form quench growths.
[h] Glass and quench growths.
[i] To check liquidus of binary immiscibility region.
[j] Most difficult of the primary phase regions studied and, consequently, the least accurate; tridymite only form identified.
[k] Composition of $3BaO \cdot 3B_2O_3 \cdot 2SiO_2$.

features of the BaO–SiO_2 system. Melting points, optical properties, and X-ray diffraction data for all compounds in the system were determined; and a microscopic and X-ray study of the $BaO \cdot 2SiO_2$–$2BaO \cdot 3SiO_2$ solid solution area was made.

The melting points and optical properties of the compounds were found to be, in general, in close agreement with the reported values [15, 16]. Eskola [15] reported the melting point of dibarium silicate ($2BaO \cdot SiO_2$) as being above that of platinum. By a method of optical pyrometry [19], it was possible to estimate the melting point as 1,815 ±25° C. Microscopic examination of $2BaO \cdot SiO_2$ that had been heated above 1,800° C gave some new optical data. The material appeared as irregular grains showing good cleavage parallel to the plane containing the alpha and beta vibration directions; it was biaxial positive with a very small 2V (5 to 10°); $\alpha = 1.800$, $\beta = 1.80+$, $\gamma = 1.826$.

Table 2 gives a comparison of the X-ray powder pattern diffraction data obtained in this study with that of Austin's [20]. Although agreement between the two sets of data is reasonably good, enough differences exist to warrant recording. It can be seen from table 2 that minor differences exist in interplanar spacings and relative intensities between corresponding patterns. The present study reveals additional interplanar spacings for most of the compounds, in particular for $BaO \cdot 2SiO_2$. Perhaps the most notable difference in the corresponding pairs of patterns is the lack of agreement of the three major peaks (identified as (1), (2), and (3) in table 2). Only the numbers (1) and (2) peaks for $2BaO \cdot SiO_2$ and the number (1) peaks for $BaO \cdot SiO_2$ and $2BaO \cdot 3SiO_2$ agree between the two sets of data. The remainder of the peaks are either interchanged in order of intensity or are entirely different. The discrepancies in order of intensity of the three major peaks for corresponding sets of data are due probably to orientation. In this study, an attempt was made to minimize orientation in the sample during specimen mounting. The finely ground material (passing a No. 200 mesh screen) was neither packed nor scraped at any stage of preparation but was sprinkled freely over a microscope slide (which served as a specimen holder) that had been smeared with a thin layer of petrolatum.

Study of the $BaO \cdot SiO_2$–$2BaO \cdot 3SiO_2$ solid solution area was based on the following four compositions: 100 percent of $BaO \cdot 2SiO_2$ (0 percent of $2BaO \cdot 3SiO_2$), 70.8 percent of $BaO \cdot 2SiO_2$ (29.2 percent of $2BaO \cdot 3SiO_2$), 37.5 percent of $BaO \cdot 2SiO_2$ (62.5 percent of $2BaO \cdot 3SiO_2$), and 0 percent of $BaO \cdot 2SiO_2$ (100 percent of $2BaO \cdot 3SiO2$). Results of the optical examination agreed with Eskola's study [15]. The X-ray data, however, did not conclusively show a solid solution series. The powder pattern for the composition containing 70.8 percent of $BaO \cdot SiO_2$ (29.2 percent of $2BaO \cdot 3SiO_2$) showed several double peaks which indicated the presence of two phases. Even after an additional melting and grinding of the mixture, these double peaks persisted. It is believed that single crystal work, which would permit the determination of unit cell sizes, would be the most suitable method of studying the solid solution area by means of X-rays.

4. Experimental Results and Discussion

4.1. General Statement

Table 3 gives the essential quenching data for the 178 compositions studied, grouped according to primary fields of crystallization. The compositions within each primary field are arranged according to increasing percentage of BaO. The locations of the

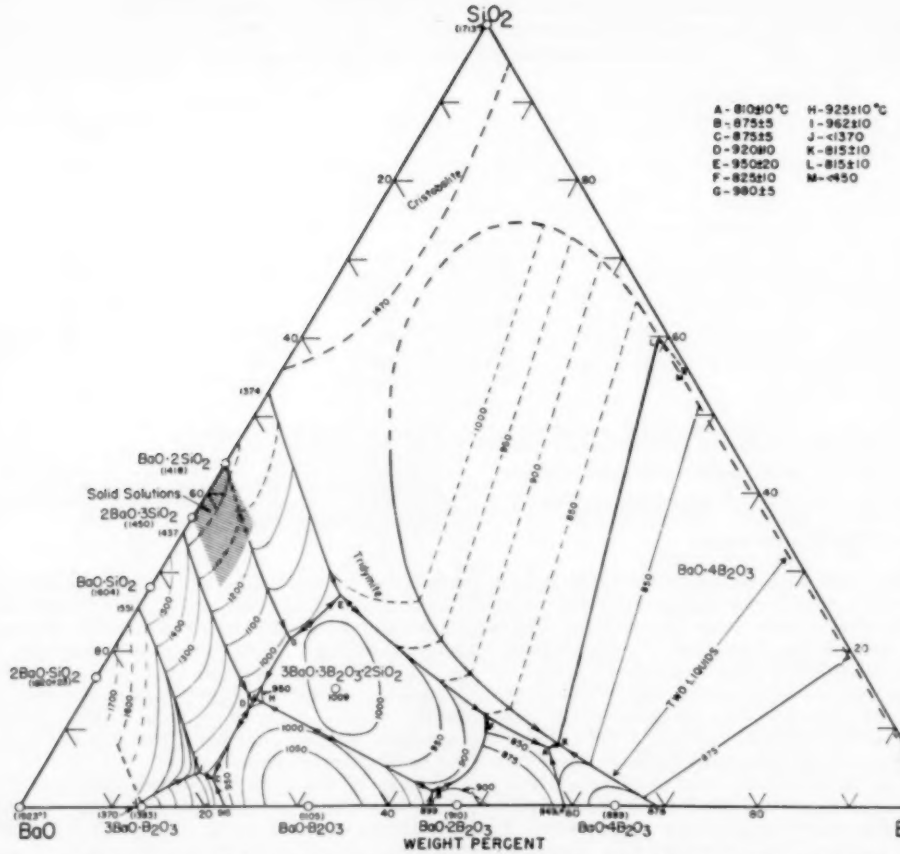

FIGURE 6. *Phase equilibrium diagram for the system* $BaO–B_2O_3–SiO_2$, *showing isotherms, boundaries, and invariant points.*

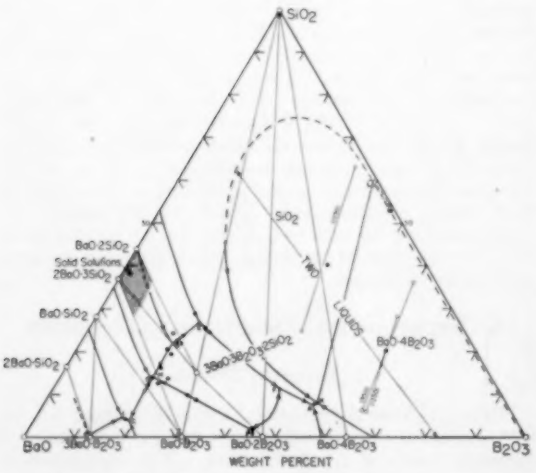

FIGURE 7. *Composition triangles in the system* $BaO–B_2O_3–SiO_2$.

compositions studied are shown in figure 1. The data from table 3 are plotted in figures 6 and 7.

Figure 6 shows the ternary diagram for the system, with the temperatures of the invariant points listed alongside. The heavy lines, solid and dashed, represent the phase boundaries and delineate the primary phase areas. The arrows indicate the direction of falling temperature, in the conventional manner. Isotherms are drawn generally at 100-deg intervals, but in some cases at 50- or 25-deg intervals. The temperatures for the polymorphic inversions of silica, such as quartz to tridymite and tridymite to cristobalite, could not be obtained experimentally, but for the case of the tridymite-cristobalite inversion the assumption was made that the inversion temperature is the same as for pure silica, namely, 1,470° C. Little data could be obtained in the regions very rich in BaO, for example, in the $2BaO·SiO_2$ and BaO primary phase areas, (1) because of the reaction of the samples with platinum at high temperatures to form barium platinates, (2) because of the extremely rapid rate of devitrification of samples during quenching, and (3) because of the rapid hydration of samples

after quenching. Experimental difficulties due largely, it is believed, to the high viscosity of the melts were encountered, likewise, in studying most of the two-liquid immiscibility region and the silica primary phase area. It should be noted that such factors were encountered as very fine crystals difficult to identify, evidences of nonequilibrium conditions, failure to obtain clear-cut separation of the immiscible liquids, and inability over most of the silica field to determine liquidus temperatures. This portion of the diagram, therefore, is of a tentative nature, but it is thought that the relationships as shown are essentially correct.

Each of the eight binary compounds shows a primary phase region in the ternary diagram (fig. 6). Only one ternary compound, $3BaO{\cdot}3B_2O_3{\cdot}2SiO_2$, is found. The system contains 5 ternary eutectics, lettered A, B, C, D, E; five ternary invariant points not eutectics (reaction points) lettered F, G, H, I, J; and 2 quintuple points, lettered K and L, at which 2 liquid phases are in equilibrium with 2 crystalline phases and vapor. With the exception of point J, temperatures of these invariant points range between 810° and 980° C. The invariant point J is under 1,370° C, the value of the binary eutectic between BaO and $3BaO{\cdot}B_2O_3$. However, as point J is located near the binary eutectic, it is to be expected that its liquidus value is not much lower. One other invariant point, M, representing the equilibrium between silica, boric oxide, and $BaO{\cdot}4B_2O_3$ is postulated [21] to lie somewhere in the narrow region between the B_2O_3–SiO_2 binary and the boundary between the two immiscible liquids and one-liquid regions. The most prominent feature of the diagram is the large extent of the area of two immiscible liquids, which covers approximately 50 percent of the diagram. It is also interesting to note that the $BaO{\cdot}4B_2O_3$ and SiO_2 primary phase areas include almost 70 percent of the diagram.

Figure 7 shows the eleven composition triangles formed in the system by the Alkemade lines. For the purpose of clarity, isotherms are not shown. Three secondary binary systems are evident: $BaO{\cdot}SiO_2$–$BaO{\cdot}B_2O_3$, $3BaO{\cdot}3B_2O_3{\cdot}2SiO_2$-$BaO{\cdot}B_2O_3$, and $3BaO{\cdot}3B_2O_3{\cdot}2SiO_2$-$BaO{\cdot}2B_2O_3$ (see also fig. 8, D, E, F). It cannot be stated with assurance whether or not the system $3BaO{\cdot}3B_2O_3{\cdot}2SiO_2$-$BaO{\cdot}2SiO_2$ is a binary because the exact nature and extent of the solid solution field is not known (see fig. 8, A). The system $3BaO{\cdot}3B_2O_3{\cdot}2SiO_2$-$BaO{\cdot}B_2O_3$-$BaO{\cdot}2B_2O_3$ is seen to be a secondary ternary system. Crystallization paths for compositions in that portion of the baria-borosilicate system where liquid immiscibility does not occur are, in general, straightforward and familiar types. Typical crystallization paths in a two-liquid area are discussed by Flint and Wells [3].

4.2. Stability Fields of the Binary Compounds

a. $BaO{\cdot}2SiO_2$

Barium disilicate forms solid solutions with $2BaO{\cdot}3SiO_2$ and probably with the barium borates, the partial limits of these solid solutions are shown in figure 6. Compositions studied in the $BaO{\cdot}2SiO_2$ primary field are given in table 3, part A. Liquidus temperatures vary from the melting point of $BaO{\cdot}2SiO_2$ (1,418° C)[3] to a minimum of 950° C (point E). Optical properties of the primary phase crystals within the limits of experimental measurements did not differ from those of pure $BaO{\cdot}2SiO_2$. X-ray diffraction powder pattern data of primary phase crystals grown at 1,100° C for two compositions (11 and 13 of table 3) showed a very slight and irregular shift of *d* spacings from the pure $BaO{\cdot}2SiO_2$. The shift averaged less than 0.01 A, which is about the expected limit of accuracy of the experimental conditions. When liquidus temperatures along the join $BaO{\cdot}2SiO_2$-$3BaO{\cdot}3B_2O_3{\cdot}2SiO_2$ are plotted (fig. 8, A), a distinct and experimentally significant discontinuity is found in the liquidus curve at about 1,250° C. At this break, the minimum deviation of the curve from one which would show no breaks (that is, a straight line) is 50° C, a value undoubtedly above the limit of experimental error. It must be concluded, therefore, that the break in the curve is is indicative of a relatively sharp phase change. It would seem likely that the break represents the transition temperature oetween two closely related solid solutio ı phases, but the nature of these phases is not known.

b. $2BaO{\cdot}3SiO_2$

Dibarium trisilicate forms solid solutions with $BaO{\cdot}2SiO_2$ and with the barium borates. The partial limits of the solid solutions are shown in figure 6. Compositions studied in the $2BaO{\cdot}3SiO_2$ primary field are given in table 3, B.

Primary phase crystals from compositions 21, 22, 29, 30, 33, 37 (table 3, B) gave distinct evidence of being solid solution crystals, both by optical and X-ray methods. No detectable differences in optical properties from pure $2BaO{\cdot}3SiO_2$ were found for the primary phase crystals obtained from the remaining compositions. However, crystals from the compositions 25, 26, 38, and 42 showed small and irregular shifts in *d* spacings, to a maximum extent of 0.02 A. X-ray data were not obtained for all compositions in the field, but it seems from the limited data available that all or most of the compositions would show similar slight differences.

When the liquidus temperatures are plotted for the join $3BaO{\cdot}3B_2O_3{\cdot}2SiO_2$–$2BaO{\cdot}3SiO_2$, a discontinuity is found in the liquidus curve at about 1,250° C (fig. 8, B), or the same temperature as the break in the $3BaO{\cdot}3B_2O_3{\cdot}2SiO_2$-$BaO{\cdot}2SiO_2$ join. The liquidus curve for the join $BaO{\cdot}B_2O_3$-$2BaO{\cdot}3SiO_2$ (fig. 8, C) similarly shows a break in the $2BaO{\cdot}3SiO_2$ solid solution field, but it is not as pronounced and occurs at a lower temperature (approximately 1,125° C). The latter join is more nearly parallel to the isotherms than the other two joins mentioned, and, consequently, the location of the break may be less accurate.

[3] Temperature values on the $BaO{\cdot}SiO_2$ binary have not been converted to the International Temperature Scale of 1948.

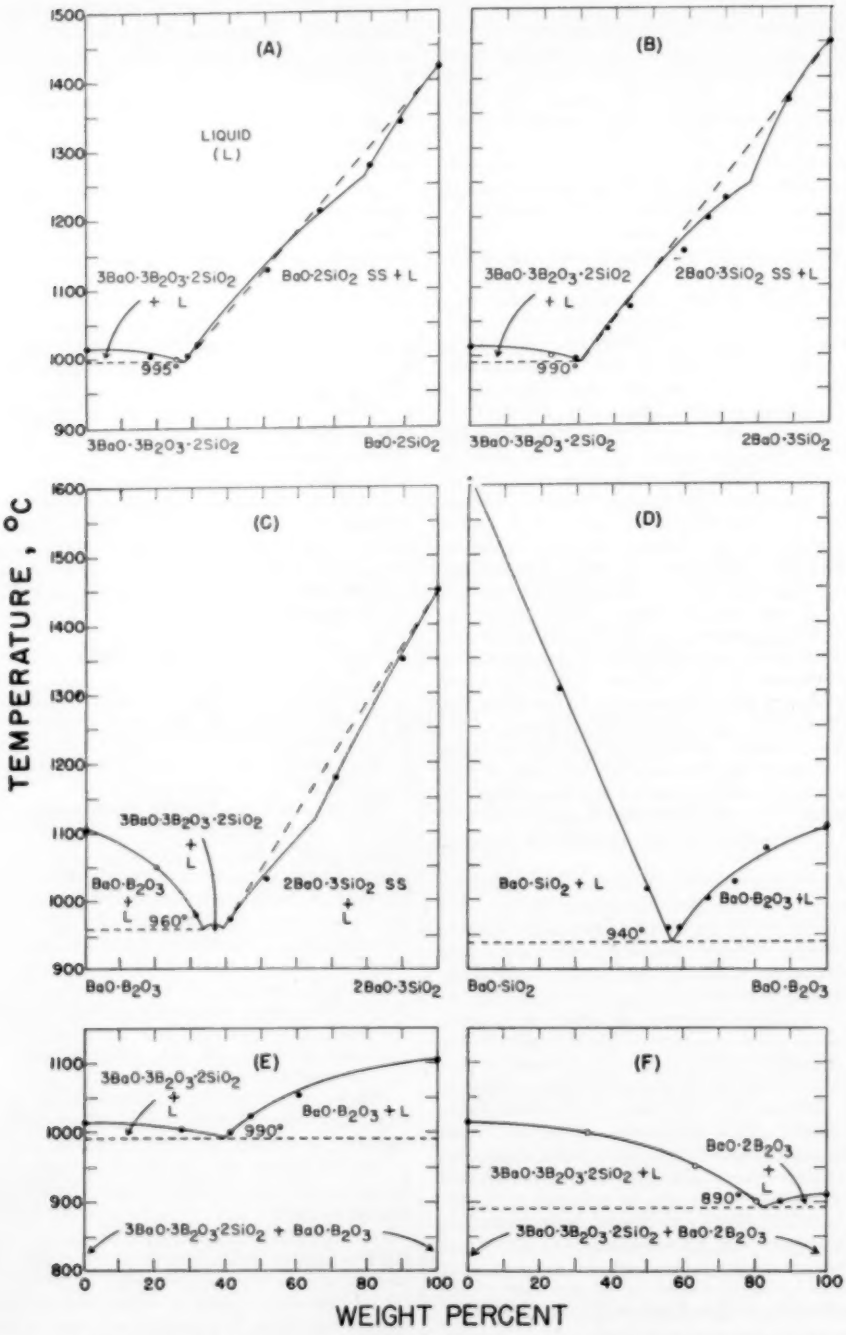

FIGURE 8. *Some binary and pseudo binary systems investigated in the system* $BaO–B_2O_3–SiO_2$

●, Actual composition; ○, extrapolation from isotherms; ss, solid solution.

his study of the system BaO-Al_2O_3-SiO_2, [illegible] found varying indices of refraction for all compositions within the field surrounding the composition $2BaO{\cdot}3SiO_2$; and, therefore, he proposed that $2BaO{\cdot}3SiO_2$ is not a true compound but merely a particular composition at or near the maximum in a solid solution series. X-ray powder pattern data appeared to confirm his conclusion, although the variations in d values were not as pronounced as the variations in indices of refraction. In the present study, the reverse situation is true, namely, that X-ray measurements in many instances appear to show very slight differences that are not revealed by optical methods. The present study, likewise, does not conclusively prove the existence of a $2BaO{\cdot}3SiO_2$ primary phase field of unvarying composition and properties.

The question as to whether or not dibarium trisilicate is a compound becomes especially important when drawing the composition triangle (fig. 7). Obviously, if dibarium trisilicate is not a compound, no Alkemade line can originate from its composition point. Finally, the method of eutectic matrix composition [22, 23] was tried.

Seven pertinent ternary compositions, shown by the dots in figure 7, were selected for study. The formulated compositions were melted and stirred above the liquidus in order to obtain homogeneity. The melts were then crystallized by subjecting them to a slow cooling schedule. The phases in the devitrified samples were identified by petrographic examination.

Most of the samples contained varying amounts of quench growths and small amounts of glass, indicating that equilibrium conditions and complete devitrification were not achieved. In most cases only two crystalline phases were identified. This may be explained on the basis that devitrification of the solid solution crystals consumed all the available liquid before a third phase crystallized. In the case of one composition (*a*, table 4) for which no solid-solution phase appeared, a different explanation is necessary, as, for example, too small a percentage of fine-grained material intermixed with the quench growths of another phase.

Figure 9 and table 4 show the location of the compositions studied, together with the phases identified. Compositions *b*, *c*, and *e* after devitrification showed three phases: $3BaO{\cdot}3B_2O_3{\cdot}2SiO_2$, $BaO{\cdot}B_2O_3$, and a solid solution with optical properties closely resembling $2BaO{\cdot}3SiO_2$. Only $3BaO{\cdot}3B_2O_3{\cdot}2SiO_2$ and $BaO{\cdot}B_2O_3$ were found in composition *a*. The data from the four mentioned compositions are consistent with the compatability triangles as drawn. If the correct Alkemade line were really the join $3BaO{\cdot}3B_2O_3{\cdot}2SiO_2$-$BaO{\cdot}SiO_2$, a possibility if $2BaO{\cdot}3SiO_2$ is only a composition in a partial solid solution series between $BaO{\cdot}2SiO_2$ and $BaO{\cdot}SiO_2$, a $BaO{\cdot}B_2O_3$ phase should not have been obtained for compositions *b* and *e*, but rather some indication of $BaO{\cdot}SiO_2$. Furthermore, composition *g* gave no indication of a $3BaO{\cdot}3B_2O_3{\cdot}2SiO_2$ phase whereas *a*, only a few percent away, showed a moderate amount of $3BaO{\cdot}3B_2O_3{\cdot}2SiO_2$. It seems reasonable to suppose that an Alkemade line, as drawn, passes between the two compositions. Compositions *b* and *e* both showed $BaO{\cdot}B_2O_3$, whereas compositions *d* and *f*, nearby, did not. The only join that satisfies this result connects $3BaO{\cdot}3B_2O_3{\cdot}2SiO_2$ and $2BaO{\cdot}3SiO_2$. Because the composition $2BaO{\cdot}3SiO_2$ seems to represent the only logical point for the origination of two Alkemade lines, it must be concluded that $2BaO{\cdot}3SiO_2$ is a compound, regardless of the extent of the solid-solution region.

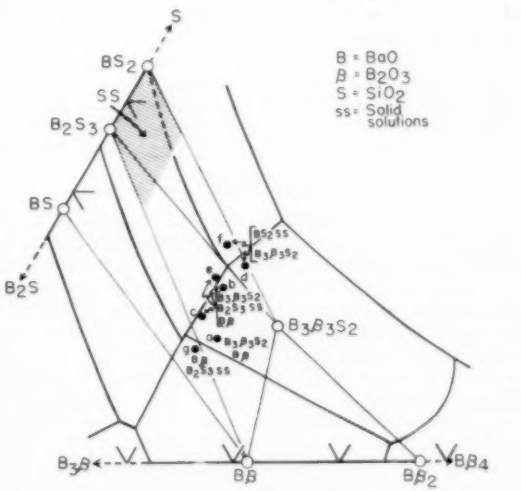

FIGURE 9. *Location of 7 glass compositions and phases identified in the devitrified glasses.*

TABLE 4. *Phases identified in seven devitrified glasses, in an attempt to determine by the method of eutectic matrix composition whether $2BaO{\cdot}3SiO_2$ is a compound or merely a particular composition*

Designation	Composition number in table 3	Composition (weight percent)			Phases identified (l=large amount; s=small amount; m=moderate amount; ss=solid solution)			
		BaO	B_2O_3	SiO_2	$3BaO{\cdot}3B_2O_3{\cdot}2SiO_2$	$BaO{\cdot}B_2O_3$	$2BaO{\cdot}3SiO_2$	$BaO{\cdot}2SiO_2$
		%	%	%				
a	177	64.8	21.4	13.8	m	l		
b	172	61.3	19.5	19.2	l	s	m (ss)	
c		65.3	19.0	15.7	s	m	s (ss)	
d		58.3	20.1	21.6	l			s (ss)
e	27	61.5	18.1	20.4	l	s	s (ss)	
f	17	58.8	17.3	23.9	m			m (ss)
g		67.4	20.2	12.4		l	s (ss)	

c. $BaO \cdot SiO_2$

Compositions determining the barium silicate primary phase area (fig. 6) are listed in table 3, part C. Optical properties of the $BaO \cdot SiO_2$ crystals agreed well with the recorded values [15, 16, 20]. The lowest temperature for any liquidus in the field is 875 ±5° C, at the ternary eutectic C. Barium silicate and barium borate form a true binary system, with a eutectic at about 940° C and 43 percent, by weight, $BaO \cdot SiO_2$ (fig. 8, D).

d. $2BaO \cdot SiO_2$ and BaO

Information on the field of dibarium silicate could be obtained from only seven compositions (table 3, part D). Six of these compositions were located along the $2BaO \cdot SiO_2$-$BaO \cdot SiO_2$ boundary. The seventh (No. 70), on about the 79 percent BaO isopleth, formed quench growths and barium platinates to the extent that the liquidus value could not be determined; and such was the case for all compositions in the field richer in BaO. Dashed isotherms were drawn by extrapolation from known boundary curves.

For similar reasons, together with the high temperatures involved, no liquidus values could be obtained in the BaO primary phase region. Because of the reaction of BaO at elevated temperatures with the platinum of a thermocouple, differential thermal analysis cannot be applied, as was discovered in the study of the BaO-B_2O_3 binary system [4]. It is apparent, however, that the BaO primary field must be limited to a small area in the corner of the diagram.

e. $3BaO \cdot B_2O_3$

Liquidus determinations in the tribarium borate field presented most of the same difficulties as in the $2BaO \cdot SiO_2$ and BaO areas; however, the three compositions studied (table 3, part E) served to delineate the tribarium borate field, which is the smallest in the system. Composition 71 (liquidus 908° C) was close to the ternary eutectic C (fig. 6), and a sample quenched from 875° C showed three crystalline phases ($3BaO \cdot B_2O_3$, $BaO \cdot B_2O_3$, and $BaO \cdot SiO_2$) in equilibrium with small amount of glass. A ternary reaction point is postulated at J (figs. 6 and 7), where the crystalline phases $3BaO \cdot B_2O_3$, BaO and $2BaO \cdot 2iO_2$ would be in equilibrium with glass. The invariant point J might be expected to be near in both temperature and composition to the binary eutectic between $3BaO \cdot B_2O_3$ and BaO at 1,370° C.

f. $BaO \cdot B_2O_3$

Eighteen compositions (table 3, F) were studied in the primary phase field of barium borate, and no experimental difficulties or unusual features were encountered. Four ternary invariant points C, D, H, and B (figs. 6 and 7) ranging in temperature from 875° to 925° C were located on its boundaries. Barium borate forms true binary systems with both $BaO \cdot SiO_2$ and $3BaO \cdot 3B_2O_3 \cdot 2SiO_2$ (fig. 8, D and E).

g. $BaO \cdot 2B_2O_3$

The 12 compositions studied in the barium diborate field are given in table 3, G. The compound forms a true binary system with $3BaO \cdot 3B_2O_3 \cdot 2SiO_2$ (fig. 8, F) and accordingly a temperature maximum is shown on the boundary curve BF of figure 6.

h. $BaO \cdot 4B_2O_3$

Compositions for this field are listed in table 3, H. Barium tetraborate occupies a primary phase region second in extent only to that of silica. It is interesting to note, also, that less than 5 percent of the field lies in a one-liquid region, whereas more than 95 percent is in the two-liquid immiscible area (fig. 6). As the percentage of silica increased, determinations of liquidus temperatures became successively more difficult because of sluggish crystallization of the viscous melts. The boundary between the two-liquid and the one-liquid region adjacent to the B_2O_3-SiO_2 binary was not determined and is shown as a dashed line (figs. 6 and 7). That this boundary must lie within several percent of the B_2O_3-SiO_2 binary is deduced from the limited data on the indices of refraction of the low index conjugate glass (see "*n* of quenched glass", table 3, H). The values are approximately the same or less than those for pure SiO_2 or B_2O_3, both of which are about 1.46 [24].

i. B_2O_3

If the compatability triangle formed by $BaO \cdot 4B_2O_3$, B_2O_3, and SiO_2 (fig. 7) is correct, no additional compounds showing a stable primary phase area can be formed within its boundaries. It is then necessary to postulate an invariant point M located in the narrow one-liquid region adjacent to the B_2O_3-SiO_2 binary, where the three primary phases coexist in equilibrium. In this event boric oxide would possess a very narrow primary field extending from the invariant point to pure boric oxide. Because of experimental difficulties, no attempt was made to substantiate this conclusion.

j. SiO_2

The silica primary phase area (fig. 6) occupies approximately 40 percent of the phase diagram, and the silica liquidus surface is distorted by the occurrence of liquid immiscibility. The field consists of a large portion in the two-liquid area limited on three sides by a portion in the one-liquid area. A narrow strip of one-liquid area is present along the B_2O_3-SiO_2 binary and extends to the postulated eutectic at M. Another portion of the one-liquid area extends along the BaO-SiO_2 binary to the eutectic at 1,374° C between $BaO \cdot 2SiO_2$ and SiO_2, and then penetrates the interior of the diagram adjacent to the primary phase fields of $BaO \cdot 2SiO_2$, $3BaO \cdot 3B_2O_3 \cdot 2SiO_2$, and $BaO \cdot 2B_2O_3$. The invariant point A representing the equilibrium between SiO_2, $BaO \cdot 2B_2O_3$ and $BaO \cdot 4B_2O_3$ is at 810° C. That the silica field must extend to the $BaO \cdot 4B_2O_3$ field was

is evident from the fact that SiO_2 and $BaO{\cdot}4B_2O_3$ were the only primary phases identified in the two-liquid area, and fields entering a two-liquid area must persist until liquid miscibility is again encountered.

Systematic investigation of the silica field was hampered by the extremely high viscosities of all the melts and the attendant slow rate of crystal growth and approach to equilibrium. Actual liquidus values could not be obtained for a number of compositions (115, 117, 119, 122, 123, 128 table 3, I); but phase identification in these cases was useful in approximating the limits of liquid immiscibility. In areas adjacent to the primary phase boundaries, it was not usually possible to determine the exact temperature of appearance or disappearance of the silica phase. Consequently, the silica area of the diagram is less accurate than the rest both as regards to temperature and boundaries.

Tridymite was the only form of silica identified. Even at temperatures as low as 823° C (No. 125 of table 3, I), or about 44 deg below the inversion temperature of pure tridymite to quartz, no quartz was formed in any of the mixtures. In the study of the system K_2O–MgO–SiO_2 [25], Roedder also found tridymite persisting metastably, to a eutectic point at 715 ±10° C. He concluded that a quartz liquidus stable at a higher temperature presumably existed, but because of the viscous nature of the glass, excessive time would be required to demonstrate the point.

4.3. Stability Field of the Ternary Compound $3BaO{\cdot}3B_2O_3{\cdot}2SiO_2$

This was the only ternary compound found in the system, and 37 compositions within its primary field were studied (table 3, J). The field occupies a large portion of the glass-forming region of the system, and it was observed qualitatively that rates of devitrification (or of crystal growth) with the exception of compositions in the silica field were much slower than for compositions in the other primary phase areas.

The compound $3BaO{\cdot}3B_2O_3{\cdot}2SiO_2$ melts congruently at 1,009° C. As seen from the spacing of the isotherms (fig. 6), its primary field is extremely flat, indicative of a high degree of dissociation of the compound in the liquid state [26]. The compound crystallizes as irregular, elongated, and fiber-like grains with positive sign of elongation. It is biaxial negative: $\alpha=1.669$, $\beta=1.696$, $\gamma=1.702$ (25° C), with a moderate optic axial angle of about 35°. The refractive index of the glass is 1.633. When the compound is formed by devitrifying glass, polysynthetic twinning is prominent. Data from the X-ray diffraction powder patterns are given in table 5.

Five ternary invariant points (B, H, G, E, F, fig. 6) are found along the boundaries of the $3BaO{\cdot}3B_2O_3{\cdot}2SiO_2$ field. The lowest of these invariant points is at 825°±10° C (point F). The ternary compound forms true binary systems with $BaO{\cdot}B_2O_3$ and with $BaO{\cdot}2B_2O_3$ (fig. 8, E, F). As discussed earlier, it is not believed that $3BaO{\cdot}3B_2O_3{\cdot}2SiO_2$ forms a true binary system with $BaO{\cdot}2SiO_2$, because the nature of the solid solution area is not known (fig. 8, A).

TABLE 5. *X-ray diffraction data for the compound* $3BaO{\cdot}3B_2O_3{\cdot}2SiO_2$, *showing interplanar spacings (d) and their relative intensities (I)*

d	*I*	*d*	*I*
A	%	*A*	%
4.96	35	2.17	23
4.91	47	2.14	20
4.65	48	2.09	25
4.09	17	2.06	35
3.95	46	2.04	32
3.69	53	1.989	17
3.59	16	1.868	11
3.51	6	1.808	3
3.43	13	1.776	7
3.29	89 (3)	1.759	10
3.09	100 (1)	1.742	13
2.96	98 (2)	1.722	4
2.82	58	1.659	6
2.75	12	1.642	8
2.72	16	1.602	17
2.65	25	1.579	4
2.50	50	1.529	8
2.47	8	1.484	9
2.34	13	1.461	4
2.20	23		

4.4. Two-Liquid Area

The approximate shape of the two-liquid area at the liquidus is shown in figure 6. An interesting feature of the immiscibility area is the marked increase in concentration of BaO in the less siliceous liquids, proceeding toward the interior of the diagram from the baria-boric oxide binary. The maximum content of BaO in the ternary liquids is about 43 percent, which is an increase of 11 percent over the BaO content of the corresponding binary liquid. A similar observation was made in the lime-boric oxide-silica system [3, 21] and in the ZnO-B_2O_3-SiO_2 system [27]; but in these systems both the CaO-SiO_2 and the CaO-B_2O_3 binaries and the ZnO-SiO_2 and ZnO-B_2O_3 binaries, respectively, exhibit large immiscible regions. In the present system only the BaO-B_2O_3 binary possesses a liquid immiscibility region, but the flat liquidus portion of the BaO-SiO_2 system indicating an approach to two-liquid immiscibility as discussed earlier (fig. 5) is probably a factor contributing to the wide extent of liquid immiscibility in the ternary system. In a study of the effect of lanthanum and barium in glass-forming systems, Brewster and his coworkers [1] present some very limited data on immiscibility in the system BaO-B_2O_3-La_2O_3. Their data indicate that in this system, the addition of La_2O_3 to the binary system BaO-B_2O_3 causes a decrease in extent of liquid immiscibility.

Geller and Bunting [28] in an investigation of the system PbO-B_2O_3-SiO_2 found a large region of two-liquid immiscibility similar to that in the CaO-B_2O_3-SiO_2 system. The PbO-B_2O_3 binary has an immiscibility gap [29], but none has been reported in the PbO-SiO_2 binary [30, 31]. The immiscibility area, nevertheless, shows an increase in concentration of

TABLE 6. *Tie-line compositions in the immiscibility area*

Composition number	Compositions									Liquidus	Separation
	Initial *			High SiO_2 glass			Low SiO_2 glass				
	BaO	B_2O_3	SiO_2	BaO	B_2O_3	SiO_2	BaO	B_2O_3	SiO_2		
	wt. %	wt. %	wt. %	wt. %	wt. %	wt. %	wt. %	wt. %	wt. %	°C	
104	18.0	62.0	20.0	29.62	64.21	6.17	4.80	59.24	35.96	872	925° C/16 hr.
				29.15	64.88	5.97	11.84	60.02	28.14	872	1,250° C/1 hr.
118	20.0	40.0	40.0	32.55	42.79	24.66	3.27	33.83	62.90	>823	1,250° C/1 hr.

* Formulated from end members and not analyzed.

PbO in the less siliceous liquids proceeding toward the interior of the diagram from the PbO-B_2O_3 binary. The PbO concentration varies from about 45 percent on the PbO-B_2O_3 binary, to a maximum of about 60 percent. Inspection of the PbO-SiO_2 diagram showed that the liquidus curve had not been determined beyond about 35 percent, by weight, of SiO_2. It is postulated, therefore, from the shape of the ternary immiscibility boundary that the liquidus curve in the unexplored area of the PbO-SiO_2 binary might be S-shaped as in the BaO-SiO_2 system.

A study was made of the compositions of conjugate liquids formed within the immiscible area by melting of two compositions, one in the $BaO{\cdot}4B_2O_3$ and the other in the SiO_2 primary field. The results are listed in table 6 and shown in a portion of figure 7. In figure 7, the solid dots in the $BaO{\cdot}4B_2O_3$ and SiO_2 fields represent the two initial compositions; and the open circles connected by straight lines, the analyzed values of the separated compositions.

The initial compositions were prepared from the end members, barium carbonate, silica gel and boric acid, by the described method of repeated grinding and partial fusion. These two compositions were not analyzed at the start, but the two separated compositions, regardless of the degree of separation, and the associated initial one must lie on a straight lind provided there has been no change on the initial composition during the heat treatment. Figure 7 shows that the three associated compositions do lie essentially on a straight line; and it is reasonable to assume that composition number 118 (in the silica field) was altered slightly during its preparation. In no case was separation of the conjugate immiscible liquids complete, but the intersection of the line passing through them with the boundaries of the immiscible area is a tie line for the particular temperature of separation.

The quintuple line KL is the boundary separating the $BaO{\cdot}4B_2O_3$ and SiO_2 primary fields. Any point on the quintuple line represents the equilibrium between two liquids of compositions K and L, two solids $BaO{\cdot}4B_2O_3$ and SiO_2, and vapor.

As separation of the immiscible liquids could not be achieved by gravity at the liquidus temperature or slightly above, the actual separations were made well above the liquidus. For composition number 104 (fig. 7 and table 6) separation was tried at two temperatures, 925° and 1,250° C, in an attempt to obtain information on the effect of temperature on the extent of two-liquid immiscibility. Because of incomplete separation, it was not possible to draw any conclusions from the lengths of the two tie lines. Inspection of the data, however, in two other respects was revealing: (1) The tie lines for the two temperatures of separation for composition 104 (fig. 7) showed a small but significant angle between them. This rotation of the tie line with increasing temperature is positive indication that the compositions of the conjugate liquids are changing with temperature [32]. (2) The indices of refraction, measured with the polarizing microscope, of clear fragments of the low silica (high index) conjugate glasses were as follows: 1.542 ±0.002 and 1.540 ±0.002 (25° C) for the glasses separated as liquids at 925° and 1,250° C, respectively. Extrapolations from figure 10 showing the indices of refraction of the quenched glasses indicate that a decrease in index of refraction of 0.002 corresponds to a decrease in BaO content of about 2 percent. Measurements of the high silica conjugate glasses were more difficult and less exact, but the index of refraction of the glass separated at 1,250° C was definitely higher (between 1.45 and 1.46) than the glass separated at 925° C (just under 1.45). It seems, therefore, from these data that the two-liquid area decreases in extent with increasing temperature.

A few preliminary experiments were performed using the high-temperature centrifuge developed by T. F. Newkirk and Fred Ordway [4] [33]. Much better separations than by gravity were obtained, and this approach offers new promise in the study of liquid immiscibility. Their equipment, however, is suitable only for small samples, and micromethods of analysis would have to be applied.

Recent studies on several selected compositions located near the boundary of the BaO rich immiscible liquid have shown that it is possible to quench these compositions as two glasses at one temperature and as one glass at some higher temperature, presumably where complete miscibility is encountered. Work is in progress with the view of determining the shape of the immiscibility dome.

4.5 Isofract diagram for quenched glasses

Figure 10 shows an isofract diagram for the quenched glasses. It can be seen that barium oxide

[4] Associated with the Portland Cement Association Fellowship at the National Bureau of Standards.

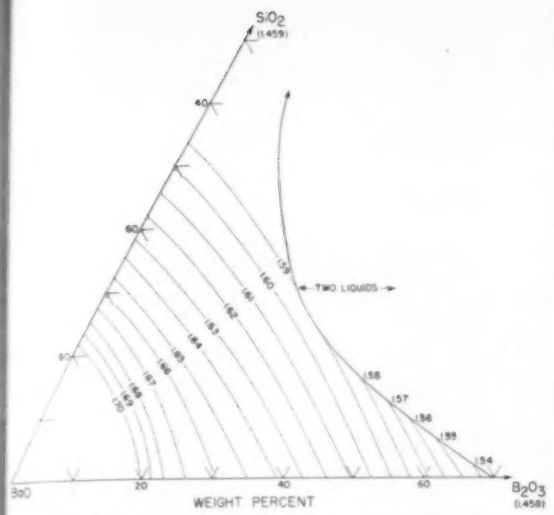

FIGURE 10. *Indices of refraction of quenched glasses in the system* $BaO–B_2O_3–SiO_2$.

imparts the greatest change in refractive index and that the increase in refractive index for a given addition of BaO becomes greater as the BaO corner is approached. Of particular interest is the convex nature of the isofracts, with the BaO vertex as a common center of curvature. Thus, indices of glasses lying on a BaO isopleth will show a maximum at about the center of the isopleth. These findings agree with those of Hamilton and his coworkers [2], who have made a detailed and accurate study of indices and densities of annealed glasses in the system. Their index values are higher, in general, by a small but irregular amount from those of the present study, in which no attempt was made to relieve the internal stresses and strains caused by quenching.

5. Summary

The equilibrium diagram for the system $BaO-B_2O_3-SiO_2$ was constructed from data, obtained essentially by the quenching method, on 178 ternary compositions. All the binary compounds showed primary fields in the ternary system. One new compound, $3BaO·3B_2O_3·2SiO_2$, melting at 1,009° C and possessing an extremely flat primary field was found, and its optical and X-ray properties described. Table 7 lists the compositions and liquidus temperatures of the ternary invariant points together with the crystalline phases in equilibrium with liquid.

The $BaO·4B_2O_3$ and SiO_2 primary phase areas include almost 70 percent of the diagram, and over these areas exists a large region of two-liquid immiscibility. On the basis of rotation of a tie line in the immiscibility region at two temperatures and of a change in index of refraction of the conjugate glasses at the two temperatures, it was concluded that the immiscibility gap decreases with increasing temperature.

Applying the method of eutectic matrix compound composition showed that $2BaO·3SiO_2$ is probably a compound and not merely a particular composition, even though the exact nature and extent of the $2BaO·3SiO_2$ solid-solution field could not be ascertained. The solid-solution region between $2BaO·3SiO_2$ and $BaO·2SiO_2$ extends into the interior of the diagram and was found to be complex.

An isofract diagram for the quenched glasses shows that barium oxide exerts the greatest influence on increase of refractive index. The isofracts lie nearly parallel to the borosilicate binary.

A self-adjusting, bridge-type controller suitable for precise temperature control of a quenching furnace was described briefly.

TABLE 7. *Ternary invariant points in the system* $BaO-B_2O_3-SiO_2$

Point [a]	Phases in equilibrium with one liquid	Type	Composition [b]				Temperature
			BaO	B_2O_3	SiO_2	Approximate limits	
			wt %	wt %	wt %	wt %	°C
A	$BaO·2B_2O_3$, $BaO·4B_2O_3$, SiO_2	Eutectic	38.7	53.8	7.5	±0.3	810 ±10
B	$BaO·B_2O_3$, $BaO·2B_2O_3$, $3BaO·3B_2O_3·2SiO_2$	do	54.2	44.0	1.8	±.3	875 ±5
C	$3BaO·B_2O_3$, $BaO·B_2O_3$, $BaO·SiO_2$	do	77.4	19.0	3.6	±.3	875 ±5
D	$BaO·B_2O_3$, $BaO·SiO_2$, $2BaO·3SiO_2$	do	68.0	18.6	13.4	±.3	920 ±10
E	$3BaO·3B_2O_3·2SiO_2$, $BaO·2SiO_2$, SiO_2	do	51.8	21.2	27.0	±1.0	950 ±20
F	$3BaO·3B_2O_3·2SiO_2$, $BaO·2B_2O_3$, SiO_2	Reaction	43.4	45.4	11.2	±1.0	825 ±10
G	$3BaO·3B_2O_3·2SiO_2$, $BaO·2SiO_2$, $2BaO·3SiO_2$	do	60.2	18.4	21.4	±.5	980 ±5
H	$BaO·B_2O_3$, $BaO·SiO_2$, $2BaO·3SiO_2$	do	67.5	18.5	14.0	±.3	925 ±10
I	$3BaO·B_2O_3$, $BaO·SiO_2$, $2BaO·SiO_2$	do	78.3	17.3	4.4	±.6	992 ±10
J	BaO, $3BaO·B_2O_3$, $2BaO·SiO_2$	do	87	12	1	[c] ?	<1,370
M [d]	$BaO·4B_2O_3$, B_2O_3, SiO_2	Eutectic	<2	>30	<30	[c] ?	<450
	Phases in equilibrium with two liquids (K, L)						
K	$BaO·4B_2O_3$, SiO_2	[e]	37.4	54.6	8.0	±1.0	815 ±10
L	$BaO·4B_2O_3$, SiO_2	[e]	1	40	59	[c] ?	

[a] Figures 6 and 7.
[b] Determined by extrapolation of established boundary curves to intersection; values given in weight percent.
[c] Because exact location of one or more boundaries not determined.
[d] Postulated [21].
[e] Quintuple line joins compositions of liquids K and L.

The authors take pleasure in expressing their appreciation to Floyd A. Mauer for the design and construction of the self-adjusting bridge-type furnace controller; to Edgar H. Hamilton, G. W. Cleek, and O. H. Grauer, of the Glass Section of the National Bureau of Standards, for preparation of the seven devitrified glass samples used in determining the nature of the $2BaO{\cdot}3SiO_2$ composition; and to Barbara M. Sullivan for obtaining the X-ray diffraction powder pattern data.

6. References

[1] Gordon F. Brewster, Norbert J. Kreidl, and Tyler G. Pett, Lanthanum and barium in glass-forming systems, J. Soc. Glass Tech. **31,** 153 (1947).

[2] Edgar H. Hamilton, G. W. Cleek, and O. H. Grauer, Some properties of BaO-B_2O_3-SiO_2 glasses and a theory of glass structure. (Publication pending.)

[3] E. P. Flint and Lansing S. Wells, The system lime-boric oxide-silica, J. Research NBS **17,** 727 (1936) RP941.

[4] Ernest M. Levin and Howard F. McMurdie, The system BaO-B_2O_3, J. Research NBS **42,** 131 (1949) RP1956.

[5] E. S. Shepherd, G. A. Rankin, and F. E. Wright, Binary systems of alumina with silica, lime, and magnesia, Am. J. Sci. [4] **28,** 293 (1909).

[6] W. L. Hill, G. T. Faust, and D. S. Reynolds, The binary system P_2O_5-$2CaO{\cdot}P_2O_5$, Am. J. Sci. **242,** 457 (1944).

[7] H. S. Roberts, The Geophysical Laboratory furnace thermostat, J. Opt. Soc. Am. **11,** 171 (1925).

[8] Henry Shenker, John L. Lauritzen, Jr., and Robert J. Corruccini, Reference tables for thermocouples, NBS Cir. 508 (1951).

[9] R. J. Corruccini, Differences between the international temperature scales of 1948 and 1927, J. Research NBS **43,** 133 (1949) RP2014.

[10] B. Hague, A. C. bridge methods, 5th ed. (Sir Isaac Pitman & Sons, Ltd, London, 1946).

[11] G. W. Morey, The ternary system Na_2O-B_2O_3-SiO_2, J. Soc. Glass Tech. **35,** 270 (1951).

[12] J. W. Greig, Immiscibility in silica melts, Am. J. Sci. [5], **13,** 1–44, 133–54 (1927).

[13] A. Cousen and W. E. S. Turner, Studies of the glasses boric oxide-silica, J. Soc. Glass Tech. **12,** 169–190 (1928).

[14] N. K. Dertev and T. H. Khudyakova, Solubility of silica in SiO_2-B_2O_3 glasses (Zhadnov Ind. Inst., Gorki) J. Applied Chem. USSR **23,** 839–45 (1950).

[15] P. Eskola, The silicates of strontium and barium, Am. J. Sci. [5], **4,** 345 (1922).

[16] R. H. Thomas, Phase equilibrium in a portion of the ternary system BaO-Al_2O_3-SiO_2, J. Am. Ceram. Soc. **33,** [2], 36 (1950).

[17] Ya. I. Ol'shanskiĭ, Equilibrium of two immiscible liquids in silicate systems of alkali-earth metals, Doklady Akad. Nauk., SSSR, **76** [1], 93 (1951); J. Am. Ceram. Soc. abstr., **34** [8], 145 (1951).

[18] W. Eitel, Silicate melt equilibria, Par. 67 (Rutgers University Press, New Brunswick, N. J. 1951).

[19] R. F. Geller, A resistor furnace with some preliminary results up to 2,000° C, J. Research NBS **27,** 555 (1941) RP1443; R. F. Geller, P. J. Yavorsky, B. L. Steierman, and A. S. Creamer, Studies of binary and ternary combinations of magnesia, calcia, baria, beryllia, alumina, thoria and zirconia in relation to their use as porcelains, J. Research NBS **36,** 277 (1946) RP1703.

[20] Alfred E. Austin, X-ray diffraction data for compounds in systems Li_2O-SiO_2 and BaO-SiO_2, J. Am. Ceram. Soc. **30** [7], 218 (1947).

[21] G. W. Morey and Earl Ingerson, System CaO-B_2O_3-SiO_2, Am. Mineralogist **22** [1], 38 (1937).

[22] Wilfrid R. Foster, Contribution to the interpretation of phase diagrams of ceramists, J. Am. Ceram. Soc. **34** [5], 151 (1951).

[23] Wilfrid R. Foster, A study of solid state reaction in the ternary system MgO-ZrO_2-SiO_2, J. Am. Ceram. Soc. **34** [10], 302 (1951).

[24] A. N. Winchell, The microscopic characters of artificial inorganic solid substances or artificial minerals, 2nd ed. (John Wiley & Sons, Inc., New York, N. Y., 1931.)

[25] Edwin Woods Roedder, The system K_2O-MgO-SiO_2, Am. J. Sci. **249,** 81–130 and 224–248 (1951).

[26] Alexander Findlay, The phase rule and its applications, p 113 (Dover Publications, New York, N. Y., 1945).

[27] Earl Ingerson, G. W. Morey and O. F. Tuttle, The systems K_2O-ZnO-SiO_2, ZnO-B_2O_3-SiO_2, Zn_2SiO_4-Zn_2GeO_4, Am. J. Sci. **246,** 31 (1948).

[28] R. F. Geller and E. N. Bunting, The system PbO-B_2O_3-SiO_2, J. Research NBS **23,** 275 (1939) RP1231.

[29] R. F. Geller and E. N. Bunting, The system PbO-B_2O_3, J. Research NBS **18,** 585 (1937) RP995.

[30] R. F. Geller, A. S. Creamer, and E. N. Bunting, The system: PbO-SiO_2, J. Research NBS **13,** 237 (1934) RP705.

[31] F. P. Hall and Herbert Insley, Phase diagrams for ceramists, J. Am. Ceram. Soc., Part II (Nov. 1947).

[32] G. Masing, Ternary systems, p. 103 (Reinhold Publishing Corp., New York, N. Y., 1944).

[33] T. F. Newkirk and Fred Ordway, The high-temperature centrifuge and its use in phase equilibrium studies, Bull. Am. Ceram. Soc. **31** [3] (abst., 54th Annual Meeting Program 1952).

Washington, May 12, 1953

...al of Research of the National Bureau of Standards Vol. 51, No. 1, July 1953 Research Paper 2431

Errors Introduced by Finite Space and Time Increments in Dynamic Response Computation

Samuel Levy and Wilhelmina D. Kroll

An investigation is made of the accuracy and stability of numerical integration methods when applied to the computation of the dynamic response of structures to impact loads. The effect of finite time increments is studied both by obtaining analytical solutions for a single-degree-of-freedom system and by carrying out numerical integrations for many-degree-of-freedom systems; the effect of finite space increments is studied by replacing a continuous beam by a discrete number of elastically connected point masses. It is found that: (1) Of the methods investigated, only Houbolt's is stable when the time increments are large compared with the natural periods of the system. Errors are introduced by Houbolt's method, in this case, which result in the damping out of the responses in the higher modes of vibration. All of the methods give good results when the time increment is less than about 1/30 of the period in the highest frequency mode. (2) The distributed mass of a beam can be considered to be concentrated at relatively few mass points for computational purposes; using a five mass idealization, the bending moment at the center of a uniform beam is determined with good accuracy.

1. Introduction

With larger aircraft, higher landing speeds, and the necessity of flying in bad weather, the transient vibrations caused by severe gusts, landing impacts, and similar shock loads are becoming increasingly important in the stress analysis of airplanes. The usual method of computing these transients is to superpose the response in a small number of the important modes [1, 2].[1] Such computations are lengthy and in some cases give results that are of questionable accuracy [3].

Houbolt [4] presents a numerical integration method in which the derivatives in the equations of motion are replaced by finite differences to permit a step-by-step calculation of the dynamic response of an elastic aircraft entering a gust. Houbolt's method is adaptable to the problem of the dynamic response of an airplane to landing impact and was used [5] to determine the deflections of the wing for an unsymmetrical two-point landing of a model airplane. From these deflections, the bending moments on each wing at stations 17.5 inches from the wing root were computed. The computed results were compared with experimental results. The agreement was good, indicating that the difference equation approach holds promise as a means of determining the dynamic response of airplanes to shock loads.

The purpose of the present paper is to determine the effect of the use of finite time increments and of the replacement of the continuous structure by a discrete number of elastically connected point masses on the accuracy and convergence of numerical integration methods. The errors due to using too coarse a time increment to adequately describe the fine detail in the force-time history and due to approximating the initial conditions by various finite difference approximations are not considered in this report. A general study of errors in numerical integration procedures, using techniques similar to those in this report, is given in references [6] and [7].

[1] Figures in brackets indicate the literature references at the end of this paper.

2. Error Due to Finite Time Increment

In order to determine the errors introduced by finite time increments in numerical integration methods, a study is made of a single-degree-of-freedom system having simple loading conditions. The motion of more complicated systems can be considered as being made up of the motion in several normal modes, each mode acting as a single-degree-of-freedom system. The results of this study can be used, therefore, in judging the adequacy of the various numerical integration methods for complicated systems as well as for simple systems. The results are determined in analytical form, using the calculus of finite differences, for convenience in judging the accuracy of the methods and the peculiar nature of the errors introduced by using them.

2.1. Basic Problem Considered

The basic problem considered in this section is shown in figure 1. The mass, if initially disturbed, should vibrate without damping or amplitude build-up at a natural frequency $\omega=\sqrt{k/m}$ (rad/sec). For such a system, the equation of motion is

$$m\frac{d^2x}{dt^2}+kx=0. \tag{1}$$

In applying numerical integration methods to the solution of this equation, the following notation is used:

Δt = time increment between successive steps in the numerical integration process.
n = number of steps taken from $t=0$ to $t=n\Delta t$; as subscript, indicates value when $t=n\Delta t$.
x_n = displacement when $t=n\Delta t$.

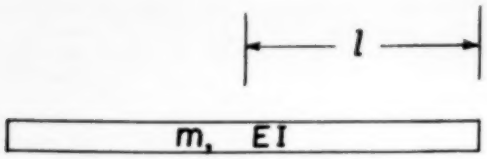

FIGURE 2. *Beam used in computations.*

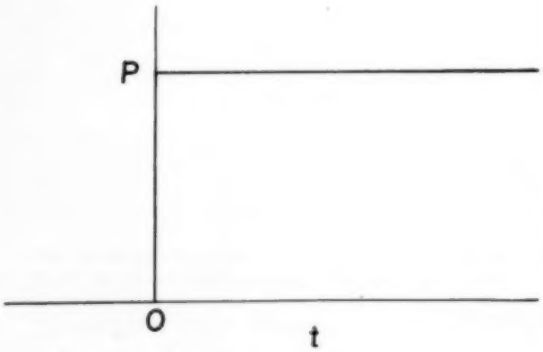

FIGURE 3. *Time history of force applied to beam.*

concerned, a study is made of the error resulting when this method of numerical integration is used and a finite number of lumped masses replace the distributed mass. This is done by comparing the computed responses with 3, 5, and 7 lumped masses for an undamped, uniform, free-free beam of mass m, length $2l$ and bending stiffness, EI, figure 2, using Houbolt's method as modified in reference [5]. It is assumed that the beam is subjected to suddenly applied transverse loads of the type shown in figure 3. As more complicated time histories of loading can be considered to be made up of stepwise changes of the type shown in figure 3, the results will be significant for any type of transverse loading. All displacements are taken in a vertical direction. Translation and rotation of the beam are considered in addition to bending.

3.1. Uniform Beam With Load Applied at Center

A uniform beam is considered to be suddenly subjected to a constant normal force P at its center. The beam is idealized by considering the mass of the actual beam, figure 4 (a), to be concentrated at 3-, 5-, and 7-mass points, figures 4 (b), 4 (c), and 4 (d), respectively.

To evaluate the combined errors due to the use of finite numbers of mass points and finite time increments, three time increments are used in the numerical analysis for each mass distribution. These time increments are

$$\Delta t = \sqrt{ml^3/12EI}, \quad \frac{1}{3}\sqrt{ml^3/12EI}, \quad \text{and} \quad \frac{1}{5}\sqrt{ml^3/12EI}.$$

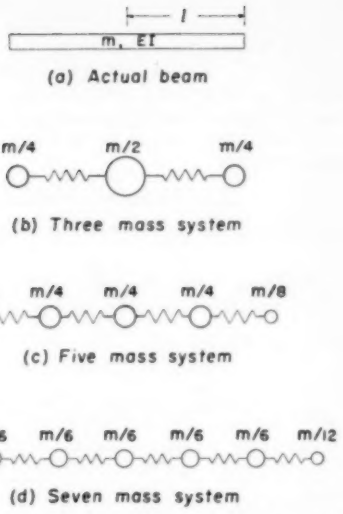

FIGURE 4. *Distributions of mass considered for beam subjected to impact at center.*

The computations are carried out as described in reference [5] and as shown for a typical case in the appendix. In this procedure, the initial conditions are taken into account by considering the displacements zero for three time increments prior to the initial instant of time. The flexibility is taken into account by the use of influence coefficients. Matrix algebra is used to simultaneously compute the displacements at all the mass points at a particular increment of time from the given forces acting at that time and from the known displacements at the preceding three increments in time. The bending moment at the center is then computed from the inverse of the influence coefficient matrix, the displacements at the various mass points, and the lever arms from these mass points to the center of the beam. The bending moment, M, at the center of the beam, positive when concave away from the side of the beam being struck, is plotted on a dimensionless basis in figures 5, 6, and 7 for the 3-, 5-, and 7-mass approximations, respectively. It is noted that, as the time interval used in the step-by-step numerical integration is shortened, the maximum absolute value of the bending moment is increased. As is to be expected from the analysis of a single degree-of-freedom system, the errors of the numerical method cause a damping out of the oscillatory response and, as the time increment is decreased, a decrease in the period of the oscillatory response.

For each of figures 5 to 7, the mass distribution is kept constant, and the increment of time used in the numerical integration is varied to show the effect of time increment. In each of figures 8 to 10, the time increment is kept constant, and the responses for the different mass distributions are plotted to bring out more clearly the effect of increasing the

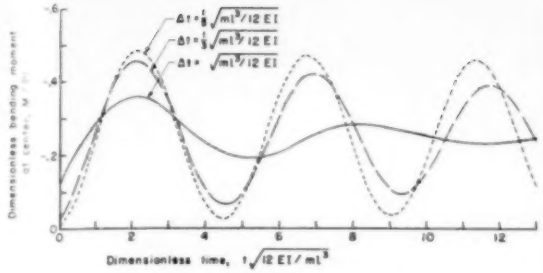

FIGURE 5. *Bending moment ratio at the center of the beam caused by impact at center, three-mass idealization.*

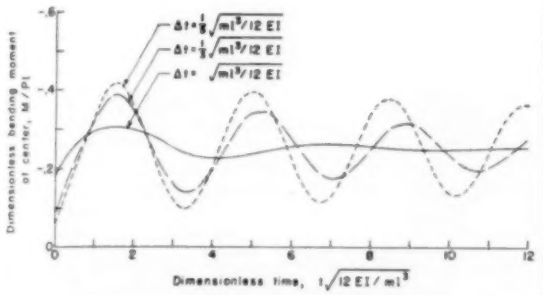

FIGURE 6. *Bending moment ratio at the center of the beam caused by impact at center, five-mass idealization.*

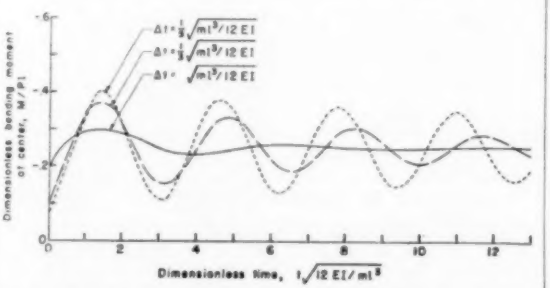

FIGURE 7. *Bending moment ratio at the center of the beam caused by impact at center, seven-mass idealization.*

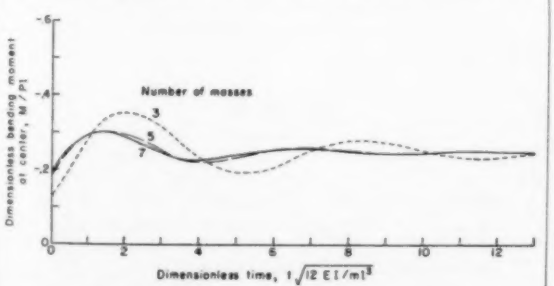

FIGURE 8. *Bending moment ratios for different mass idealizations with impact at center mass, time increment* $\Delta t = \sqrt{ml^3/12EI}$.

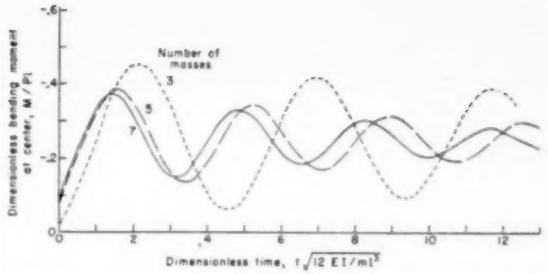

FIGURE 9. *Bending moment ratios for different mass idealizations with impact at center mass, time increment* $\Delta t = 1/3\sqrt{ml^3/12EI}$.

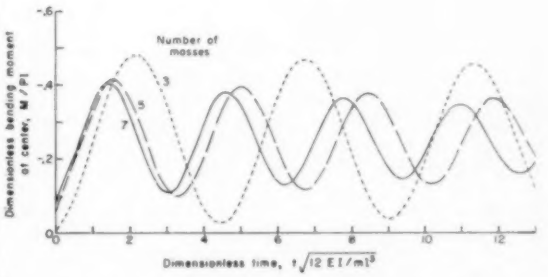

FIGURE 10. *Bending moment ratios for different mass idealizations with impact at center mass, time increment* $\Delta t = 1/5\sqrt{ml^3/12EI}$.

number of masses. The maximum absolute value of the bending moment at the center differs by not more than 4 percent for the 5- and 7-mass systems, regardless of time increment. There is some difference in the period of the response for the shorter time increments for the 5- and 7-mass systems.

3.2. Beam With Impact at One Tip

Because it was believed that an impact at a tip mass might result in a more severe loading condition, an investigation is made for the case of a load P applied at the tip of the beam shown in figure 4 (a), using the idealizations shown in figures 4 (b) and 4 (c). The bending moments at the center for the 3- and 5-mass idealizations are shown in figures 11 and 12, respectively. It is noted again, as in case 3.1, that as the time interval used in the step-by-step numerical integration is shortened, the maximum absolute value of the bending moment at the center is increased. As is to be expected from the analysis of a single-degree-of-freedom system, the errors of the numerical method cause a damping out of the oscillations, which is particularly evident for the longest time increment, and a decrease in the period of the oscillatory response as the time increment is decreased.

In figures 13 to 15, the time increment is kept constant, and the responses for idealization of the beam by 3 and 5 masses are plotted to bring out

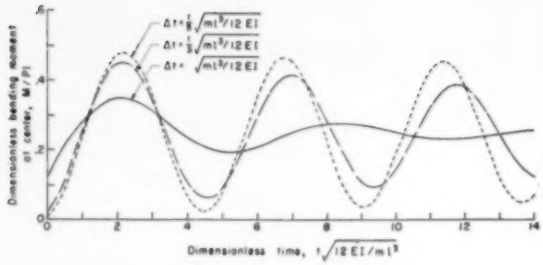

FIGURE 11. *Bending moment ratio at the center of the beam caused by impact at a tip, three-mass idealization.*

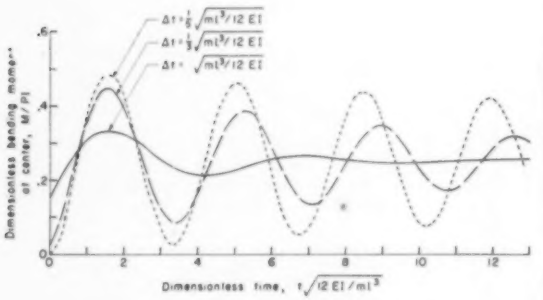

FIGURE 12. *Bending moment ratio at the center of the beam caused by impact at a tip, five-mass idealization.*

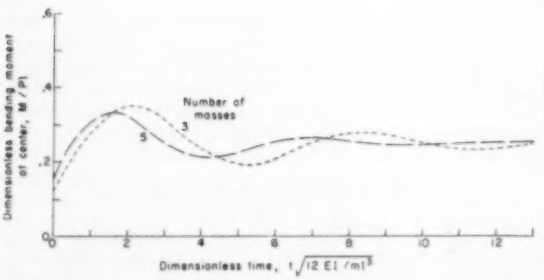

FIGURE 13. *Bending moment ratios for different mass idealizations with impact at tip, time increment* $\Delta t = \sqrt{ml^3/12EI}$.

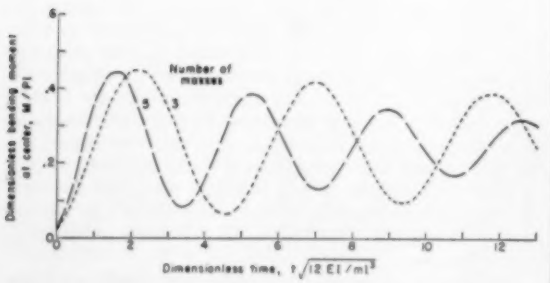

FIGURE 14. *Bending moment ratios for different mass idealizations with impact at tip, time increment* $\Delta t = 1/3\sqrt{ml^3/12EI}$.

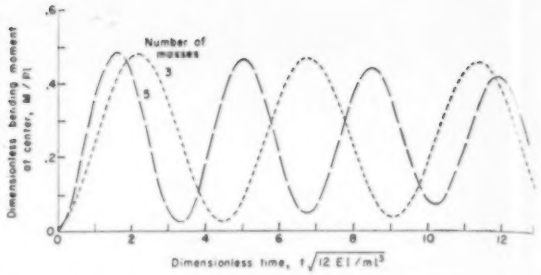

FIGURE 15. *Bending moment ratios for different mass idealizations with impact at tip, time increment* $\Delta t = 1/5\sqrt{ml^3/12EI}$.

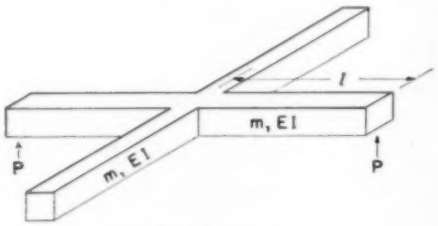

(a) Actual beams

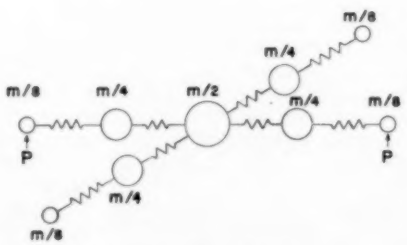

(b) Idealized beams

FIGURE 16. *Mass distribution considered for two beams normal to each other subjected to tip impact.*

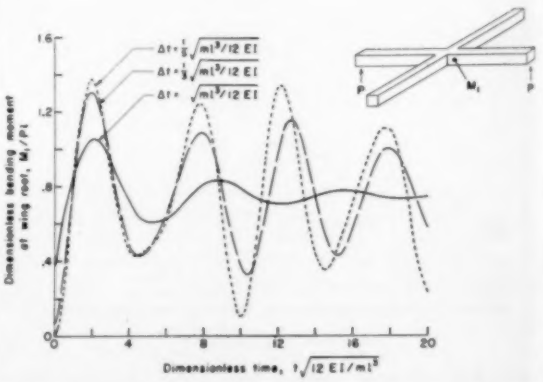

FIGURE 17. *Bending moment at wing root for pair of beams representing airplane, each beam idealized by five masses.*

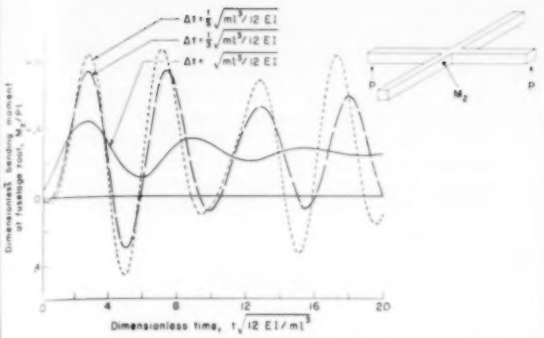

FIGURE 18. *Bending moment at fuselage root for pair of beams representing airplane, each beam idealized by five masses.*

the effect of increasing the number of masses. It can be seen that the period of the initial vibratory response decreases with an increase in the number of masses and that the damping increases. The maximum bending moment at the center is relatively unaffected.

3.3. Pair of Beams Representing a Fuselage and Wing With Impact at Both Wing Tips

An airplane can be approximated by two uniform beams at right angles to each other, one beam representing the wing, the other the fuselage. Such a system, figure 16 (a), is investigated. Each beam is idealized as 5 masses, as shown in figure 16 (b). The suddenly applied constant loads, P, are considered to act at each wing tip. The bending moments at the center of both the "fuselage" and "wing" beams are computed by using the same three time increments in the numerical integration as were previously used. The bending moment at the center of the struck beam (wing) is shown in figure 17 and that for the other beam (fuselage) is shown in figure 18. The agreement between the bending moment ratios for the three values of time increment is only fair even for the two shortest time increments. As might have been expected from the analysis given of the single-degree-of-freedom system, the error due to using the longest time increment is evident in the marked damping of the oscillatory response.

3.4. Discussion

It is estimated that a time increment of about 1/30 of the period in the fundamental mode is necessary for good accuracy in numerical-integration methods. This value is based on several factors.

(1) The solution given in eq (26) corresponds to about 20 time increments per fundamental period. In this case the frequency coefficient, 0.961, is in error by about 4 percent.

(2) The convergence indicated in the figures is not quite complete for the shortest time increment, which corresponds to 1/13.74 of the fundamental symmetrical mode period and only 1/5.00 of the lowest antisymmetrical mode period. A shorter time increment than this is certainly needed to give the response of the higher modes.

(3) The recommended time increment is likely to be used for computing responses with slower convergence than the bending moment at the center of the beam and for structures with slower convergence than that of a uniform beam.

(4) It is likely that computations by numerical methods will be carried out by automatic computing machines where the advantage of additional accuracy from a smaller time increment can be had with less penalty than when hand computing is used.

It is noted from figures 8, 9, and 10 that, for each time increment considered, the response to an impact at the center is essentially the same for the 5- and 7-mass idealizations of the beam but considerably higher for the 3-mass system. For impacts at one end of the beam, figures 13, 14, and 15, the response shows less change in going from the 3- to the 5-mass idealizations than is the case for impact at the center. It would appear that a uniform beam should be approximated by a 5-mass idealization if errors in the bending moment at the center are to be small.

In table 1, the maximum absolute values of bending moment ratios are given. For the beam with the impact at the center, the absolute value of the bending moment increased as the time interval for integration was decreased, but decreased as the number of masses used for the idealization of the distributed mass of the beam was increased. From this, it may well be that the errors caused by using a reasonable value of time interval for the numerical integration will be offset to some extent by the errors caused by using a finite number of masses. For the impact at a tip mass, the increase in bending moment with decrease in time interval is appreciable, but the decrease in bending moment with increase in number of masses is much less than for the case of impact at the center.

TABLE 1. *Maximum absolute value of bending moment at center of uniform beam struck with force P*

Time interval	$\lvert M/Pl \rvert$		
	3-mass	5-mass	7-mass
Impact at center			
$\sqrt{ml^3/12EI}$	0.355	0.305	0.295
$1/3\sqrt{ml^3/12EI}$	.450	.383	.368
$1/5\sqrt{ml^3/12EI}$	.480	.416	.400
Impact at tip			
$\sqrt{ml^3/12EI}$	0.355	0.333	.....
$1/3\sqrt{ml^3/12EI}$	.450	.448	.....
$1/5\sqrt{ml^3/12EI}$	.480	.485	.....

It is evident from figure 5 that the period of the response approaches the value for the exact solution for a beam idealized by 3 masses as the time interval in the integration is shortened. This same decrease in period with time increment is noted in figures 6 and 7 for the 5- and 7- mass idealization of the beam. The period of the response also decreases as the number of masses is increased, figures 7, 8, and 9. This latter result, at least qualitatively, verifies that obtained by Duncan [9]. He has obtained an exact solution showing that the periods of the computed modes of vibration of a uniform beam decrease as the number of masses chosen to represent the beam is increased, and that the magnitudes of the errors in the computed periods vary inversely as the square of the number of masses.

4. Conclusions

From the analyses of the responses of single-degree-of-freedom and many-degree-of-freedom systems to a suddenly applied force, it may be concluded that:

a) Numerical integration methods give results that closely approximate the exact solution only if the increment of time between successive steps in the integration is small compared to all the natural periods of vibration of the system. In cases similar to those investigated where bending moment near the center is desired, a time increment of about $\frac{1}{20}$ of the fundamental period of the system will give good results.

b) Of the methods investigated, the Houbolt method is the only one that gives convergent results for large time increments. In this method, errors introduced by large time increments result in the damping out of oscillatory response.

c) The distributed mass of the beam can be considered to be concentrated at relatively few mass points for computational purposes. In cases similar to those investigated, approximating a uniform beam by a 5-mass idealization gives good results.

5. Appendix

The detailed method of determining the response of a uniform beam to an impact load by numerical integration is given in this appendix for the case of a beam subjected to an impact at its tip. The case considered is that where the time increment is $\Delta t=\sqrt{ml^3/12EI}$. The responses for all the other cases presented in this report are obtained in a similar manner.

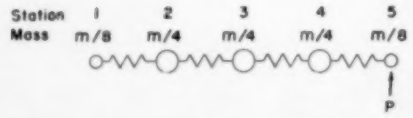

FIGURE 19. *Mass distribution for example considered in appendix.*

The mass of the uniform beam is considered to be distributed at five stations along its length, figure 19. The force, P, is applied at the tip, station 5. As used in this report, an influence coefficient, $\delta_{r,s}$ is the displacement at station r due to a unit load at station s with the center of the beam, station 3, fixed. The influence coefficients are given in table 2. Denoting the displacement positive upward at station r by d_r, the force at station r by F_r, and the rotation at station 3 by α, the displacements of the beam at stations 1, 2, 4, and 5 are

$$\left.\begin{aligned} d_1&=d_3+\delta_{11}F_1+\delta_{12}F_2-\alpha l,\\ d_2&=d_3+\delta_{12}F_1+\delta_{22}F_2-\alpha\frac{l}{2},\\ d_4&=d_3+\delta_{44}F_4+\delta_{45}F_5+\alpha\frac{l}{2},\\ d_5&=d_3+\delta_{45}F_4+\delta_{55}F_5+\alpha l \end{aligned}\right\}. \tag{A1}$$

Substituting the values of the influence coefficients from table 2 into eq (A1), and solving for the forces

TABLE 2. *Influence coefficients $\delta_{r,s}$ for 5-mass idealized beam shown in figure 19*

s \ r	1	2	3	4	5
1	$P/3EI$	$5P/48EI$	0	0	0
2	$5P/48EI$	$P/24EI$	0	0	0
3	0	0	0	0	0
4	0	0	0	$P/24EI$	$5P/48EI$
5	0	0	0	$5P/48EI$	$P/3EI$

in terms of the displacements at each station and of the rotation at station 3.

$$\left.\begin{aligned} F_1&=\frac{48EI}{7l^3}\left(2d_1-5d_2+3d_3-\frac{\alpha l}{2}\right),\\ F_2&=\frac{48EI}{7l^3}\left(-5d_1+16d_2-11d_4+3\alpha l\right),\\ F_4&=\frac{48EI}{7l^3}\left(-11d_3+16d_4-5d_5-3\alpha l\right),\\ F_5&=\frac{48EI}{7l^3}\left(3d_3-5d_4+2d_5+\frac{\alpha l}{2}\right) \end{aligned}\right\}. \tag{A2}$$

From the condition that the sum of the forces equal zero,

$$F_1+F_2+F_3+F_4+F_5=0, \tag{A3}$$

and substituting from eq (A2), the value of F_3 is

$$F_3=\frac{48EI}{7l^3}\left[3d_1-11d_2+16d_3-11d_4+3d_5\right] \tag{A4}$$

From the requirement that the net moment equal zero

$$F_1(0)+F_2\left(\frac{l}{2}\right)+F_3(l)+F_4\left(\frac{3l}{2}\right)+F_5(2l)=0, \quad \text{(A5)}$$

and using eq (A2) and (A4),

$$\alpha=0.25\,\frac{d_1}{l}-1.5\,\frac{d_2}{l}+1.5\,\frac{d_4}{l}-0.25\,\frac{d_5}{l}. \quad \text{(A6)}$$

Substituting the value of α from eq (A6) into eq (A2), and rewriting eq (A4):

$$\left.\begin{aligned}
F_1&=\frac{48EI}{7l^3}\,(1.875d_1-4.25d_2+3.00d_3-0.75d_4+0.125d_5),\\
F_2&=\frac{48EI}{7l^3}\,(-4.25d_1+11.50d_2-11.00d_3+4.50d_4-0.75d_5),\\
F_3&=\frac{48EI}{7l^3}\,(3.00d_1-11.00d_2+16.00d_3-11.00d_4+3.00d_5),\\
F_4&=\frac{48EI}{7l^3}\,(-0.75d_1+4.50d_2-11.00d_3+11.50d_4-4.25d_5),\\
F_5&=\frac{48EI}{7l^3}\,(0.125d_1-0.75d_2+3.00d_3-4.25d_4+1.875d_5)
\end{aligned}\right\}. \quad \text{(A7)}$$

The forces are the sum of the inertia loads due to the acceleration of the mass of the beam and the applied forces,

$$\left.\begin{aligned}
F_1&=-\frac{m}{8}\,\ddot{d}_1,\\
F_2&=-\frac{m}{4}\,\ddot{d}_2,\\
F_3&=-\frac{m}{4}\,\ddot{d}_3,\\
F_4&=-\frac{m}{4}\,\ddot{d}_4,\\
F_5&=-\frac{m}{8}\,\ddot{d}_5+P
\end{aligned}\right\}, \quad \text{(A8)}$$

where m is mass of uniform beam; $\ddot{d}_r$, acceleration of beam at station $r(r=1,2,\ldots 5)$; and P, applied constant force at station 5.

Using the difference eq (17), acceleration at station r can be expressed as

$$(\ddot{d}_r)_t=\frac{2}{\Delta t^2}\,(d_r)_t-\frac{5}{\Delta t^2}\,(d_r)_{t-\Delta t}+\frac{4}{\Delta t^2}\,(d_r)_{t-2\Delta t}+\frac{1}{\Delta t^2}\,(d_r)_{t-3\Delta t}. \quad \text{(A9)}$$

Equating the first of eq (A7) and (A8) and substituting for $(\ddot{d}_r)_t$ from eq (A9), we obtain

$$-\frac{m}{8\Delta t^2}\,[2(d_1)_t-5(d_1)_{t-\Delta t}+4(d_1)_{t-2\Delta t}-(d_1)_{t-3\Delta t}]=\frac{48EI}{7l^3}\,[1.875d_1-4.25d_2+3.00d_3-0.75d_4+0.125d_5]_t. \quad \text{(A10)}$$

Similar relations are obtained by using the remaining eq (A7) and (A8).

Multiplying eq (A10) and the corresponding equations for the other stations through by $3EI/Pl^3$ to express the deflections as a dimensionless ratio, and transposing terms, the equations can be written in a form which, for station 1, reads

$$\left(1.875+\frac{7ml^3}{192\Delta t^2}\right)\left(\frac{3d_1EI}{Pl^3}\right)_t-4.25\left(\frac{3d_2EI}{Pl^3}\right)_t+3.00\left(\frac{3d_3EI}{Pl^3}\right)_t-0.75\left(\frac{3d_4EI}{Pl^3}\right)_t+0.125\left(\frac{3d_5EI}{Pl^3}\right)_t=(J_1)_t, \quad \text{(A11)}$$

where

$$(J_1)_t=\frac{7ml^3}{384EI\Delta t^2}\left[5\left(\frac{3d_1EI}{Pl^3}\right)_{t-\Delta t}-4\left(\frac{3d_1EI}{Pl^3}\right)_{t-2\Delta t}+\left(\frac{3d_1EI}{Pl^3}\right)_{t-3\Delta t}\right]. \quad \text{(A12)}$$

Equation (A11) and the equations similar to it can be expressed in matrix form as

$$[A]\left\{\frac{3d_rEI}{Pl^3}\right\}_t=\{J_r\}, \quad \text{(A13)}$$

where the matrix $[A]$ is given in table 3. Solving eq (A13) for the deflections gives,

$$\left\{\frac{3d_rEI}{Pl^3}\right\}_t=[A]^{-1}\{J_r\}_t, \quad \text{(A14)}$$

TABLE 3. *Matrix [A] of deflection coefficients for use in equation (A13')*

$1.875+\frac{7ml^3}{192EI\Delta t^2}$	−4.25	3.00	−0.75	0.125
−4.25	$11.50+\frac{7ml^3}{96EI\Delta t^2}$	−11.00	4.50	−.75
3.00	−11.00	$16+\frac{7ml^3}{96EI\Delta t^2}$	−11.00	3.00
−0.75	4.50	−11.00	$11.5+\frac{7ml^3}{96EI\Delta t^2}$	−4.25
.125	−0.75	3.00	−4.25	$1.875+\frac{7ml^3}{192EI\Delta t^2}$

where $[A]^{-1}$ is obtained as the inverse of $[A]$ with $\Delta t=\sqrt{ml^3/12EI}$. The matrix $[A]^{-1}$ is given in table 4. The first of this set of equations in conventional form is

$$\left(\frac{3d_1EI}{Pl^3}\right)_t=1.344937(J_1)_t+0.589567(J_2)_t+$$
$$0.113294(J_3)_t-0.113732(J_4)_t-0.237485(J_5)_t. \quad \text{(A15)}$$

where, from eq (A12),

$$(J_1)_t=1.09375\left(\frac{3d_1EI}{Pl^3}\right)_{t-\Delta t}-0.87500\left(\frac{3d_1EI}{Pl^3}\right)_{t-2\Delta t}$$
$$+0.21875\left(\frac{3d_1EI}{Pl^3}\right)_{t-3\Delta t}. \quad \text{(A16)}$$

Similar equations can be obtained for J at the other stations.

TABLE 4. *Inverted matrix $[A]^{-1}$ of table 3 with $\Delta t=\sqrt{ml^3/12EI}$*

1.344937	0.589567	0.113294	−0.113732	−0.237485
0.589567	.519302	.305894	.079741	−.113732
.113294	.305894	.417773	.305894	.113294
−.113732	.079741	.305894	.519302	.589567
−.237485	−.113732	.113294	.589567	1.344937

It is assumed that, prior to the application of the force, P, the displacements at all stations are zero. The computations are tabulated as shown in tables 5 and 6. The J's are computed for time t, table 6, using eq (A16) for $(J_1)_t$ and similar equations for the other J's. The d's are computed for time t, table 5, using eq (A15) for $(3d_1EI/Pl^3)_t$ and similar equations for the other d's. From the d's at time t, the J's at time $t+\Delta t$ are computed and, from these, the d's at time $t+\Delta t$. Thus a time history of the displacement ratios of the uniform beam due to the suddenly applied constant force is obtained.

Since the step-by-step numerical procedure is dependent on previously computed values, it is desirable to have a check column which will indicate errors made in the computation. The deflections at each station were checked by computing the displacement, D, of the center of gravity of the beam from two different formulas. If these two values of D agreed, the computation of the deflections was assumed correct. The first equation for D_t is:

$$\frac{3EI}{Pl^3}D_t=\frac{1}{m}\sum_{r=1}^{5}\left(m_r\frac{3d_rEI}{Pl^3}\right)_t, \quad \text{(A17)}$$

where

$$m=\sum_{r=1}^{5}m_r \quad \text{(A18)}$$

$$\frac{3EI}{Pl^3}D_t=0.125\left(\frac{3d_1EI}{Pl^3}\right)_t+0.250\left(\frac{3d_2EI}{Pl^3}\right)_t+$$
$$0.250\left(\frac{3d_3EI}{Pl^3}\right)_t+0.250\left(\frac{3d_4EI}{Pl^3}\right)_t+$$
$$0.125\left(\frac{3d_5EI}{Pl^3}\right)_t. \quad \text{(A19)}$$

The other equation is obtained by substituting for $[(3d_1EI)/Pl^3]_t$, $[(3d_2EI)/Pl^3]_t$, . . . $[(3d_5EI)/Pl^3]_t$ in eq (A19), their equivalents in terms of the J's of eq (A14). This gave

$$\frac{3EI}{Pl^3}D_t=0.28571375(J_1)_t+0.28571362(J_2)_t+$$
$$0.28571375(J_3)_t+0.28571362(J_4)_t+$$
$$0.28571375(J_5)_t. \quad \text{(A20)}$$

The small differences in the coefficients in eq (A20) result from rounding-off error. For a good error indication, the coefficients, as given, are needed. The values of D from eq (A19) and (A20) are given in columns (7) and (8) of table 5.

The J's are checked by comparing their sums as determined from two different formulas. The first formula is

$$\left(\sum_{r=1}^{5}J_r\right)_t=(J_1)_t+(J_2)_t+(J_3)_t+(J_4)_t+(J_5)_t. \quad \text{(A21)}$$

The second formula is obtained by substituting in eq (A21) the value of $(J_1)_t$ in eq (A16) and corresponding values for the other J's. Then, making use of eq (A19),

$$\left(\sum_{r=1}^{5}J_r\right)_t=8.75(D)_{t-\Delta t}-7.00(D)_{t-2\Delta t}+$$
$$1.75(D)_{t-3\Delta t}+0.4375. \quad \text{(A22)}$$

The values computed from eq (A21) and (A22) are given in columns (7) and (8), respectively, of table 6. The good agreement between the check columns in tables 5 and 6 indicate that the computation is free of numerical error.

TABLE 5. *Displacement ratios at stations along a uniform beam subjected to an impact at its tip*

1	2	3	4	5	6	7	8	9
Time ratio $t\sqrt{\frac{12EI}{ml^3}}$	Displacement ratio $3d_nEI/Pl^3$ at stations—					$3EI\delta/Pl^3$		Bending moment ratio at center, M/Pl
	1	2	3	4	5	Eq (A19)	Eq (A20)	
−3	0	0	0	0	0	0	0	0
−2	0	0	0	0	0	0	0	0
−1	0	0	0	0	0	0	0	0
0	−0. 103900	−0. 049758	0. 049506	0. 257936	0. 588410	0. 125000	0. 125000	. 153654
1	−. 525637	−. 168315	. 294203	. 967785	1. 83828	. 437499	. 437499	. 309800
2	−1. 40216	−. 348058	. 820339	2. 20772	3. 79212	. 968745	. 968745	. 322636
3	−2. 72217	−. 596199	1. 61553	4. 00162	6. 55516	1. 73436	1. 73436	. 253868
4	−4. 42824	−. 927607	2. 64076	6. 35719	10. 2248	2. 74216	2. 74216	. 213325
5	−6. 50884	−1. 34718	3. 88834	9. 28142	14. 8320	3. 99603	3. 99603	. 227965
6	−8. 99357	−1. 85109	5. 37772	12. 7830	20. 3579	5. 49794	5. 49794	. 257022
7	−11. 9070	−2. 43581	7. 12514	16. 8678	26. 7835	7. 24885	7. 24885	. 265110
8	−15. 2485	−3. 10178	9. 13013	21. 5368	34. 1121	9. 24923	9. 24923	. 254424
9	−19. 0059	−3. 85121	11. 3845	26. 7865	42. 3569	11. 4993	11. 4993	. 244509
10	−23. 1735	−4. 68514	13. 8843	32. 6223	51. 5247	13. 9993	13. 9993	. 244722
11	−27. 7347	−5. 60308	16. 6319	39. 0387	61. 5123	16. 7491	16. 7491	. 249866
12	−32. 7545	−6. 60427	19. 6304	46. 0398	72. 6149	19. 7488	19. 7488	. 252659
13	−38. 1739	−7. 68860	22. 8806	53. 6226	84. 5319	22. 9884	22. 9884	. 251377
14	−44. 0108	−8. 85645	26. 3810	61. 7899	97. 3652	26. 4979	26. 4979	. 249285
15	−50. 2639	−10. 1081	30. 1306	70. 5494	111. 117	30. 2473	30. 2473	. 248816
16	−56. 9335	−11. 4436	34. 1295	79. 8742	125. 786	34. 2465	34. 2465	. 249836
17	−64. 0204	−12. 8628	38. 3783	89. 7915	141. 372	38. 4957	38. 4957	. 250307
18	−71. 5252	−14. 3657	42. 8773	100. 292	157. 874	42. 9946	42. 9946	. 250228
19	−79. 4478	−15. 9524	47. 6262	111. 377	175. 294	47. 7434	47. 7434	. 249824
20	−87. 7877	−17. 6230	52. 6249	123. 044	193. 631	52. 7420	52. 7420	. 249634

TABLE 6. *Values of J at stations on beam*

1	2	3	4	5	6	7	8
Time ratio, $t\sqrt{\frac{12EI}{ml^3}}$	Values of J at stations—					$\sum_1^5 J$	ΣJ eq (A22)
	1	2	3	4	5		
−3	0	0	0	0	0	0	0
−2	0	0	0	0	0	0	0
−1	0	0	0	0	0	0	0
0	0	0	0	0	0. 437500	0. 437500	0. 437500
1	−0. 113640	−0. 108845	0. 108426	0. 564234	1. 08107	1. 53125	1. 53125
2	−. 484093	−. 281114	. 556827	1. 66564	1. 93326	3. 39061	3. 39061
3	−1. 08641	−. 488595	1. 30132	3. 24861	3. 10535	6. 07028	6. 07028
4	−1. 86547	−. 708722	2. 22709	5. 31345	4. 69122	9. 59757	9. 59757
5	−2. 76821	−1. 13807	3. 30839	7. 86939	6. 71464	13. 9861	13. 9861
6	−3. 83981	−1. 58449	4. 59119	10. 9287	9. 14720	19. 2428	19. 2428
7	−5. 11017	−2. 09753	6. 11451	14. 5016	11. 9626	25. 3710	25. 3710
8	−6. 57770	−2. 67831	7. 87698	18. 5887	15. 1633	32. 3724	32. 3724
9	−8. 22675	−3. 33234	9. 85591	23. 1857	18. 7653	40. 2478	40. 2478
10	−10. 0499	−4. 06206	12. 0431	28. 2902	22. 7763	48. 9975	48. 9975
11	−12. 0515	−4. 86616	14. 4435	33. 9036	27. 1923	58. 6219	58. 6219
12	−14. 2374	−5. 74265	17. 0654	40. 0282	32. 0074	69. 1209	69. 1209
13	−16. 6091	−6. 69120	19. 9102	46. 6643	37. 2204	80. 4946	80. 4946
14	−19. 1638	−7. 71269	22. 9745	53. 8110	42. 8339	92. 7428	92. 7428
15	−21. 8998	−8. 80780	26. 2557	61. 4678	48. 8498	105. 866	105. 866
16	−24. 8172	−9. 97647	29. 7542	69. 6347	55. 2680	119. 863	119. 863
17	−27. 9174	−11. 2184	33. 4714	78. 3122	62. 0872	134. 735	134. 735
18	−31. 2008	−12. 5334	37. 4081	87. 5005	69. 3071	150. 481	150. 481
19	−34. 6671	−13. 9217	41. 5637	97. 1993	76. 9279	167. 102	167. 102
20	−38. 3159	−15. 3834	45. 9376	107. 409	84. 9502	184. 597	184. 597

The forces are determined from the displacements of the masses at the five stations on the beam by use of eq (A7). The forces, multiplied by thier distances from the center of the beam determine the bending moment at the center of the beam. Designating the bending moment at the center by M,

$$M=F_1 l+F_2 \frac{l}{2} \tag{A23}$$

$$M=\frac{48EI}{7l^2}(-0.25d_1+1.50d_2-2.50d_3+1.50d_4-0.25d_5) \tag{A24}$$

$$\frac{M}{Pl}=-0.5714286\,\frac{3d_1EI}{Pl^3}+3.4285714\,\frac{3d_2EI}{Pl^3}-5.7142857\,\frac{3d_3EI}{Pl^3}+3.4285714\,\frac{3d_4EI}{Pl^3}-0.5714286\,\frac{3d_5EI}{Pl^3}. \tag{A25}$$

Values of the bending moment ratio computed from eq (A25) are given in column 9, table 5. They are plotted in figure 12 for $\Delta t=\sqrt{ml^3/12EI}$.

The authors thank Mrs. L. W. Roberson for computing the responses of the uniform beams to impact loads.

6. References

[1] M. A. Biot and R. L. Bisplinghoff, Dynamic loads on airplane structures during landing, NACA ARR 4H10 and Wartime Report W–92 (October 1944).

[2] Walter Ramberg and Albert E. McPherson, Experimental verification of theory of landing impact, NBS J. Research **41,** (1948) RP1936.

[3] Walter Ramberg, Transient vibration in an airplane wing obtained by several methods, NBS J. Research **42,** 437 (1949) RP1984.

[4] John C. Houbolt, A recurrence matrix solution for the dynamic response of aircraft in gusts, NACA TN 2060 (March 1950).

[5] Wilhelmina D. Kroll and Samuel Levy, A step-by-step method of determining the dynamic response of aircraft in landing, NBS Lab. No. 6.4/1–181, PR6, BuAer TED NBS 2410 (September 21, 1949).

[6] George G. O'Brien, Morton A. Hyman, and Sidney Kaplan, A study of the numerical solution of partial differential equations, Naval Ord. Lab. Memo 10433 (January 4, 1949).

[7] R. Courant, K. Friedricks, and H. Lewy, Über die partiellen Differenzengleichungen der Mathematishen Physik, Math. Annalen, p. 32–74 (1928).

[8] Samuel Levy, Computation of influence coefficients for aircraft structures with discontinuities and sweepback, J. Aeronaut. Sci. [10] **14,** 547–560 (October 1947).

[9] W. J. Duncan, Preliminary note on the dependence of the errors in the natural frequencies on the number of elements in the segmental representation of a uniform shaft (April 1950).

Washington, May 3, 1951.

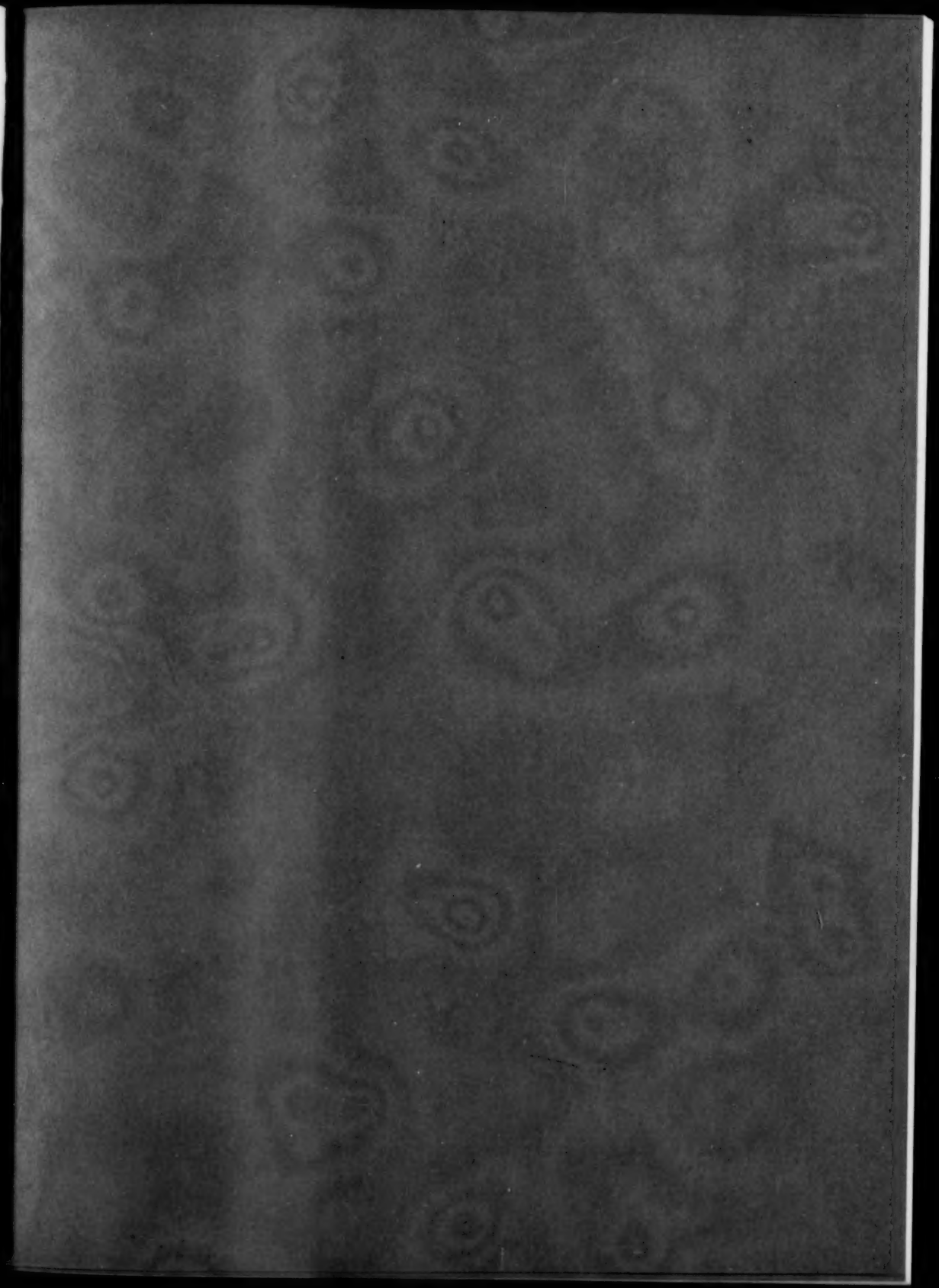

UNITED STATES
GOVERNMENT PRINTING OFFICE
BUREAU OF PUBLIC DOCUMENTS
WASHINGTON 25, D. C.

OFFICIAL BUSINESS

PENALTY FOR PRIVATE USE TO AVOID PAYMENT OF POSTAGE, $300

Journal of Research of the National Bureau of Standards Vol. 51, No. 1 July 1953

Contents

		Page
Fabrication of radio-frequency micropotentiometer resistance elements, Lewis F. Behrent.	RP2426	1
Properties of some masonry cement, D. N. Evans, A. Litvin, A. C. Figlia, and R. L. Blaine.	RP2427	11
Subsieve particle-size measurement of metal powders by air elutriation, Rolla E. Pollard.	RP2428	17
Eigenvectors of matric polynomials, Murray Mannos.	RP2429	33
The system barium oxide-boric oxide-silica, Ernest M. Levin and George M. Ugrinic.	RP2430	37
Errors introduced by finite space and time increments in dynamic response computation, Samuel Levy and Wilhelmina D. Kroll.	RP2431	57

Single copies of the above Research Papers are not available for sale. Superintendent of Documents, U. S. Government Printing Office, Washington 25, D. C., will supply 100 or more copies, and request for the purchase price should be mailed promptly to that Office.

For sale by the Superintendent of Documents, U. S. Government Printing Office, Washington 25, D. C. • Price 60 cents
$5.50 per year; six subscriptions, $3.75 foreign.

UNITED STATES GOVERNMENT PRINTING OFFICE, WASHINGTON : 1953